ATMOSPHERIC DRIVERS OF ICE DRIFT IN THE ANTARCTIC MARGINAL ICE ZONE

Ashleigh Catherine Stevenson Womack

Supervised by Associate Professor Marcello Vichi

Physical Oceanography

This dissertation is presented for the degree of

Master of Science

In the Department of Oceanography

University of Cape Town

October 2020

National
Research
Foundation

DECLARATION

I know and understand the meaning of plagiarism and declare that all the work in this document, save for that which is properly acknowledged, is my own. I have used the Harvard convention for my citations and referencing. This dissertation has been submitted to the Turnitin module and I confirm that my supervisor has seen my report and any concerns revealed by such have been resolved with my supervisor.

Signed: Signed by candidate

Date: 7th October 2020

Ashleigh Catherine Stevenson Womack

Cape Town

ABSTRACT

Sea-ice drift in the Antarctic marginal ice zone (MIZ) was investigated using an array of five drifting ice buoys, deployed during the winter sea-ice expansion, in July 2017. An initial 15-day analysis of pancake ice drift is presented, using the cluster of buoys, which shows: (1) exceptionally fast ice drift speeds and increased meandering of the buoys during cyclone activity; (2) high correlation of drift velocities with the surface wind velocities, even at 100% remotely sensed ice concentration, indicating free drift conditions where ice drift is primarily governed by wind; and (3) the presence of a clear energy peak (≈13.5 hour period), which is suggested to be excited by the passage of cyclones through the transfer of momentum from wind. Additionally, one of the buoys (buoy U1) drifted for approximately four months from the South Atlantic sector to the Indian Ocean sector of the Southern Ocean. The analysis of this buoy revealed that it remained within the MIZ even during the winter ice expansion, as the mixed pancake-frazil field was maintained. This allowed for a continued assumption of free drift conditions for buoy U1's full drift, where it continued to respond linearly to the momentum transfer from surface winds. The analysis of buoy U1 also indicated a strong inertial signature at a period of 13.47 hours however, the wavelet analysis indicated majority of the power remained within the lower frequencies. This strong influence at the lower (multi-day) frequencies has therefore been identified as the primary effect of atmospheric forcing. When these lower frequencies were filtered out using the Butterworth high-pass filter it allowed the inertial oscillations to become more significant within the wavelet power spectrum, where it can be seen that these inertial oscillations were often triggered by the passage of cyclones. The initiation of inertial oscillations of sea ice has therefore been identified as the secondary effect of atmospheric forcing, which dominates ice drift at sub-daily timescales and results in the deviation of ice drift from a straight-line path. This comprehensive analysis suggests that the general concentration-based definition of the MIZ is not enough to describe the sea-ice cover, and that the MIZ, where ice is in free drift and under the influence of cyclone induced inertial motion, and presumably waves, can extend up to ≈200 km.

ACKNOWLEDGEMENTS

This dissertation would not have been able to progress to the position it did without the kindness and support of these individuals and therefore I would like to extend my sincere thanks to all of them.

A/ Prof. Marcello Vichi for your supervision and for the incredible opportunities you have given to me to travel and constantly learn. Your support and valuable advice throughout has played a key role in the materialisation of this dissertation. You have allowed me to grow academically - more than I could have imagined. From being my supervisor in my honour's year to now, you have played a momentous role in my life.

My mother and father, for your constant encouragement and always believing in me. I am incredibly grateful for your love and support.

The National Research Foundation (NRF) and the University of Cape Town (UCT) financial need programme for funding my master's degree. I would not have been able to do my thesis without your aid.

The Department of Science and Innovation (DSI) for funding the Antarctic expeditions aboard the S.A. Agulhas II, and for the Department of Environment, Forestry and Fisheries (DEFF) for facilitating them.

The South African National Antarctic Programme (SANAP) and the Captains and crew aboard the S.A. Agulhas II for making the Antarctic expeditions possible.

A/ Prof. Gabriele Messori and A/ Prof. Inga Koszalka at Stockholm University. Thank you for allowing me to partake in the Geophysical Fluid Dynamics master's course at your university. It was such an amazing experience in which I learnt so much.

Jonathan Rogerson for your constant help and guidance with any coding problem I had, big or small, you were always there to help. I honestly would not have been able to finish without you and your snacks.

Dr. Catharina Womack for taking the time to proofread my dissertation, and together with Martin Womack for both being such a wonderful support over the past two years.

My amazing group of friends for their constant support and good humor. You all have kept me going.

And I will not forget Sina Wallschuss and Trisha Parbhoo for 'running' alongside me since our first year together. You two have been my rock for the past six years, and have shown incredible support. I have been very fortunate to be studying together with both of you.

CONTENTS

LIST OF TABLES

LIST OF FIGURES

LIST OF EQUATIONS

GLOSSARY AND ACRONYMS

ACC	Antarctic Circumpolar Current
ACT	Antarctic Circumpolar Trough
AMSR2	Advance Microwave Scanning Radiometer 2
ARTIST	Arctic Radiation and Turbulence Interaction STudy
ASI	ARTIST Sea Ice
Austral Autumn	March, April, May
Austral Winter	June, July, August
Austral Spring	September, October, November
Austral Summer	December, January, February
COI	Cone of Influence
GCOM-W1	Global Change Observation Mission for Water
IMS	Ice Mapping System
JAXA	Japan Aerospace Exploration Agency
MIZ	Marginal Ice Zone
PSD	Power Spectral Density
S.A.	South Africa
SIC	Sea Ice Concentration
SIE	Sea Ice Extent
SO	Southern Ocean
SSMIS	Special Sensor Microwave Imager/Sounder
T_b	Brightness Temperature

WIIOS	Waves In Ice Observation Systems
WOCE	World Ocean Circulation Experiment

1. INTRODUCTION

1.1. Sea ice in the Southern Ocean

The Southern Ocean (SO) is a major buffer for anthropogenic heat and carbon (Frölicher, 2015), and its large seasonality is modulated by the existence of sea ice. During winter when the Antarctic sea ice is at its largest extent, it forms a natural barrier between the ocean and the atmosphere, modifying the exchange of heat, gases and momentum. Sea ice is often thought of as a single compact component of the cryosphere, characterized by its edge, extent and thickness. At a first look, it behaves as a lid shielding the surface ocean from the atmosphere's influence; it forms and melts according to the heat balance; and its presence prevents the transfer of wind and wave energy as well as constituents such as atmospheric gases, dust and aerosols. However, sea ice is a complex material with regards to both its spatial morphology and to its material constituents (Bartels-Rausch et al., 2012). It is made of a pure solid matrix, liquid saline brines, gas bubbles and impurities, and biota and inorganic particulates may also be present (Perovich, 2017).

The winter growth of Antarctic sea ice is dominated by the presence of frazil and pancake ice at the outer region of the ice cover (Doble and Wadhams, 2006). Winter observations in the eastern Weddell Sea have exhibited an ice-covered surface comprised of small to medium pancake ice with an estimated 30%-40% frazil ice (Alberello et al., 2020; Vichi et al., 2019). Pancake ice remains unconsolidated while there is adequate wave energy preventing the pancakes from freezing together (Alberello et al., 2019). However, they generally form a consolidated ice pack as the freezing-front moves northwards, leaving them further from the effects of ocean waves (Doble and Wadhams, 2006). The unconsolidated zone, known as the marginal ice zone, is approximately between 5 km to 100 km wide (Feltham, 2005; Heorton et al., 2014), and will be discussed further in Section 1.3.

1.2. The formation and lifecycle of sea ice

The lifecycle of sea ice starts with the supercooling of the ocean, to approximately -1.8°C in the polar oceans (Lemieux et al., 2017) and the formation of the first ice crystals, called 'frazil ice'. The Antarctic is a highly dynamic environment with high wind speeds and the effects of ocean swell can penetrate deep within the higher latitudes, which greatly favours the formation of frazil ice (Petrich and Eicken, 2017). Frazil ice, seen in Figure 1.1(a), forms from very fine filaments of ice at the surface of the ocean, or ice crystals may mix within the surface layers due to turbulent fluid motion, providing that the buoyancy force is not big enough to bring them up to the ocean surface (Bartels-Rausch et al, 2012). This accumulation of frazil ice prompts the formation of grease ice, a 0.1-1 cm thick 'mushy' layer at the surface (Bauer and Martin, 1983; Lemieux et al., 2017). These two types of sea ice form the sea-ice development stage known as new ice, which does not yet make up solid ice. During calm conditions, grease ice grows thicker and more solid due to downward crystal growth at the bottom of the ice (Bauer and Martin, 1983). Then, under the influence of winds and waves, this 'mushy' layer can become consolidated to form plates with diameters of a few tens of centimetres to a few metres, known as pancake ice (Figure 1(b)) (Lemieux et al., 2017). Pancake ice consists of roughly circular ice floes with raised edges which accumulate mass and grow in diameter until the interstitial space is covered, and creates a dynamic environment (Alberello et al., 2020). Eventually these pancakes consolidate into a coherent ice sheet as the freezing front moves further north, leaving the ice floes far from the effects of ocean waves (Doble and Wadhams, 2006).

The evolution of the Antarctic marginal ice zone (MIZ) is governed by the dynamics and thermodynamics of pancake ice (Doble and Wadhams, 2006; Alberello et al., 2020). While, sea ice can extend over an area approximately the size of Antarctica itself during its winter maximum, it develops as a thin layer over the ocean's surface, on average less than 1 m thick (Eayrs et al., 2019). The majority of the Antarctic sea ice is young ice (10-30 cm thick) and first-year ice (thicker than 30 cm to 2 m) made up of solidified pancake ice, which does not survive the summer melt season. Only a few coastal regions around Antarctica have multiyear ice cover (Eayrs et al., 2019).

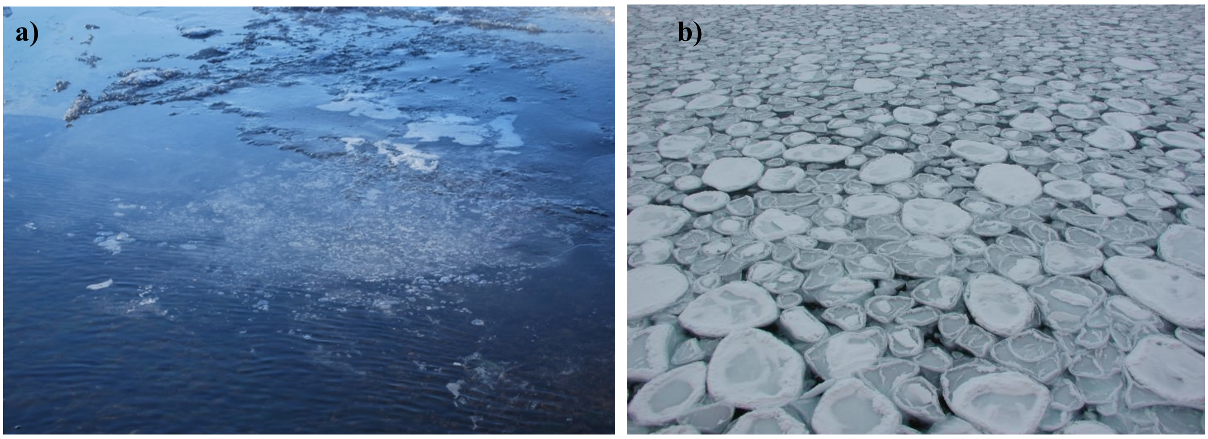

Figure 1.1: Photograph of frazil ice (a) and of pancake ice (b) in the Southern Ocean. It can be difficult to see frazil ice in the ocean as it has not yet formed a larger scale structure, but it can make the sea surface appear "oily". Pancake ice is very distinctive with its rounded and raised edges and flat interior. Photographs obtained from the iSTAR- NERC Ice Sheet Stability Programme (2014).

Fracturing, which is a consequence of divergent processes, can be considered as the next stage of the ice lifecycle. A single pancake floe may contain thousands of tiny fractures – thermal cracks – produced by the contraction of sea ice in addition to the small flexures and cracks caused by wave activity within the MIZ. In the consolidated zone, where waves are dampened out, compression and/or temperature changes can cause the flexure and cracking on the sea ice. Subsequent opening and shearing can the create cracks or working leads and ridging. These leads can extend for several hundreds of kilometres (Figure 1.2) and can be detected by satellites (Bartels-Rausch et al, 2012). Sea-ice fractures, driven by wave dynamics, ocean currents and atmospheric winds, play an important part in the formation, break-up and retreat of sea ice during a seasonal cycle (Weiss and Dansereau, 2017), and synoptic events like storms may further affect the sea-ice state in unpredictable ways (Vichi et al., 2019). Wave conditions and wave-ice interactions play a vital role in controlling the magnitude of ice breakups and the mechanical floe size redistribution in the marginal ice zone (Zhang et al., 2015). These waves tend to bend ice resulting in its break-up, when the bending-induced stresses are greater than its flexural strength or if the continual bending leads to fatigue failure (Zhang et al., 2015). Brash ice can then occur as a result of the wreckages of pack ice or ice floes, and is made up of a mixture of frazil ice from the formation stages and the fragments of fractured floes.

The third stage is the deformation of sea ice. During this stage, some regions of sea ice are compressed, while open water is created in other regions. The total ice mass does not change however, the shape of the sea-ice thickness distribution changes (Bartels-Rausch et al., 2012). Rafting and ridging are important processes of ice deformation, occurring when the ice floes converge and collide due to the differential drift of the individual floes (Hopkins et al., 1999). Rafted ice occurs when floes (partially) override each other, and is responsible for the rapid thickening of floes. In Antarctic pack ice, increases in ice thickness beyond 0.4 m is mostly attributed to rafting and ridging (Allison and Worby, 1994). Pressure ridges are created by the flexural failure of different ice sheets and the subsequent piling of ice blocks created by the failure on top and beneath the two ice sheets (Hopkins et al., 1999). While, the growth of pancake ice from frazil ice forms the distribution of small floes (where the diameter < 2.3 m), rafting and ridging of pancakes can form the distribution of large floes (diameter > 4 m) (Alberello et al., 2019). Deformation of sea-ice cover via methods of rafting and ridging accounts for the thickest ice observed and yields a mechanism for thickening, even when thermodynamic growth is delayed (Petrich and Eicken, 2017). Therefore, deformation is especially important in a warming climate as it may compensate for some of the thinning due to the reduction of ice growth and an increase in sea-ice melt (Petrich and Eicken, 2017).

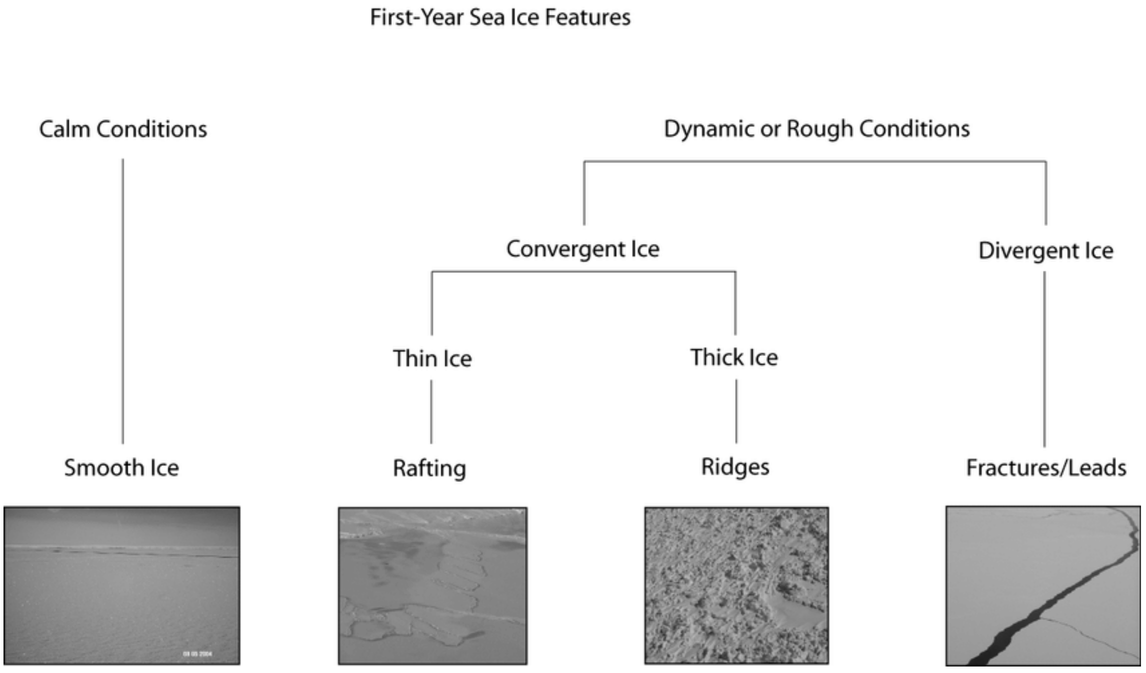

Figure 1.2: A diagram showing sea-ice features of first-year ice formed in dynamic/rough or calm conditions. The Southern Ocean is a very dynamic ocean and therefore dynamic/rough conditions dominate. The diagram was obtained from Iacozza (2011).

The last stage is the aging and melting of sea ice; yet, all these stages can occur simultaneously (Bartels-Rausch et al., 2012). Unlike the Arctic, the Antarctic sea ice shows little surface ablation and rarely has melt ponds during the summer melt season (Andreas and Ackley, 1982). The dynamic ice cover in the Southern Ocean is rather more susceptible to lateral and bottom ice melt when temperatures increase (Itkin et al., 2017). Melting of the ice cover in the Antarctic begins when the surface-layer air temperatures reach significantly above $0^{o}C$ (Andreas and Ackley, 1982), and the features formed in stages two and three become the weak points along which the sea-ice cover disintegrates (Itkin et al., 2017). The summer-time ice extent can be also effected by the storms and wave activity, however the majority of it is preconditioned by the sea-ice dynamics occurring during the winter months (Itkin et al., 2017). Higher fractured sea ice provides more surface for lateral melting and allows for stronger wave penetration, which can then increase ice melting and hence decrease the ice volume (Itkin et al., 2017).

Although the advancement and retreat of the Antarctic sea ice is the largest annually recurring event on Earth (Massom and Stammerjohn, 2010), most of our scientific knowledge on the physical and biogeochemical dynamics of sea ice in the SO has been derived from pack-ice conditions (McPhee et al., 2008; Ackley et al., 2015), and less attention has been given to the dynamics of the ice edge region (Doble et al., 2013; Doble et al., 2003). The processes by which sea ice grows and melts are not fully understood, as the nature of the ice makes it hard to study, particularly in the marginal ice zone- the boundary where air-sea interactions are at their maximum (detailed in Section 1.3). The small size of the pancake floes and their continuously varying aggregations often prevent or hinder the practice of satellite feature-tracking methods as well as it makes the deployment of conventional in situ instruments difficult (Doble and Wadhams, 2006). Deployments of buoys in the northern Weddell Sea have been largely unsuccessful because of instrumental failure as the environment is harsh, with large energy waves, strong winds (Doble and Wadhams, 2006), and below-freezing temperatures.

1.3. The Antarctic marginal ice zone

The marginal ice zone is a greatly dynamic outer region of the (partially) ice-covered ocean made up of unconsolidated or broken floes due to the propagation of waves into MIZ (Vichi et al., 2019; see also Section 1.5). It is where the interaction between the ocean and atmosphere are stronger and more variable, and where extreme weather conditions such as cyclones produce the most rapid and dramatic changes of these interactions (Andreas et al., 2010; Zhang et al., 2015; Vichi et al., 2019, Alberello et al., 2019). For operational use with satellite data, the MIZ can be classified as the distance on the sphere between two concentration contours: 15%, corresponding to the ice edge; and 80%, corresponding to sea ice classified as a very close pack (Strong et al., 2017). Below 15% the region is considered to be open ocean. This however, is a broad classification of the MIZ, and its application to the SO is subject to the validation of the remote sensing products by in situ observations.

Dynamic and thermodynamic processes vary significantly between the inner pack ice and the MIZ, involving frazil and pancake ice. This includes changes in ice-albedo feedbacks, changes in surface exchanges of heat, gases and momentum, changes in sea-ice mechanics, and variations in oceanic heat fluxes (Zhang et al., 2015). However, very little field data of metocean (meteorological and oceanographic) conditions in the SO are available, and even less in the MIZ, where wave properties such as the dispersion relation can change owing to the presence of sea ice (see Section 1.5). This is because the harsh environment of the Antarctic especially in the winter months restricts our accessibility to the sea-ice cover, and the number of in-situ platforms are limited due to high deployment and maintenance costs. The majority of the available metocean conditions have been collected during summer, when the sea-ice conditions were relatively mild. These gentle sea states reduce the intensity of many important mechanics dominating the interactions between waves and sea ice and do not involve the interactions between large ocean waves (> 3 m) and sea ice (see Section 1.5), which decay differently to smaller waves (< 3 m) (Kohout et al., 2014). This limits our knowledge of the metocean properties and our capabilities to accurately model them, and how they influence sea-ice properties and growth. Contemporary numerical models struggle to predict the advance and/or retreat of sea ice in the SO (Kwok et al., 2017; Alberello et al., 2019), leading to strong biases in ocean-atmosphere heat fluxes and salt input into the ocean (Alberello et al., 2019).

1.4. Synoptic cyclonic events and their impact on the MIZ

The Southern Ocean contains some of the most extreme and intense storms on Earth, with radii extending from 500 km to 2000 km (Hoskins and Hodges, 2005; Uotila et al., 2011). The majority of these storms are mid- and high-latitude synoptic cyclones. Cyclones primarily develop in the Atlantic and Pacific sectors of the SO (Hoskins and Hodges, 2005; Uotila et al., 2011), and generally follow a south-eastwards path, experiencing net cyclogenesis in the mid-latitudes and net cyclolysis closer to the Antarctic continent (Hoskins and Hodges, 2005). A major region for cyclogenesis is on the leeside of the Andes at around 30^{o}S (Papritz et al., 2014), while the South Atlantic, and particularly the eastern Weddell Sea, is a region of net cyclolysis for cyclones developing near South America and other regions of open ocean genesis (Hoskins and Hodges, 2005; Yuan et al., 2009; Vichi et al., 2019). The majority of severe storms occur in winter in the Atlantic at around 0^o, 30^o, and 90^{o}E, with good agreement among several storm tracking methods (Grieger et al., 2018).

These synoptic systems contribute to the general atmospheric circulation in the southern polar latitudes by maintaining the Antarctic Circumpolar Trough (ACT), a region of low-pressure over the Southern Ocean (Irving et al., 2010), between 60^{o}S and 70^{o}S, that is characterised by strong westerly winds and divergence of sea ice (Simmonds, 2003; Maksym, 2019). Papritz et al. (2014) estimated that 60%-90% of all strong precipitation events in this region are due to the synoptic cyclones. In addition, modelling results indicate that storms modify the ocean, sea ice, and surface heat fluxes (Uotila et al., 2011), as cyclonic systems transport mid-latitude moisture and heat to the polar latitudes (Messori et al., 2017; Woods and Caballero, 2016) as well as they greatly influence sea-ice drift in terms of deformation, rotation and drift velocity.

Synoptic events and storms contribute to the variability and trends of the Antarctic sea-ice extent (Holland and Kwok, 2012; Maksym, 2019; Schemm, 2018; Turner et al., 2017, Alberello et al., 2020), particularly in the Atlantic-Indian ocean region of the SO (Matear et al., 2015) rather than large atmospheric modes such as the Southern Annular Mode (SAM). These local atmospheric events act to modify sea ice, both dynamically and thermodynamically, on short timescales, with an instantaneous response of sea ice (Schlosser et al., 2016). Ice-landing synoptic storms can cause rapid variations in sea ice when warm oceanic air from the mid-latitudes is advected onto sea ice, and when storm-induced waves are generated near the ice edge (Vichi et al., 2019). This contributes to the continuation of an unconsolidated ice cover where these waves propagate far into.

1.5. Effects of wind and wave forcing on sea ice

Waves in the SO are the biggest on Earth and are attracting a significant amount of research to understand the complex physics that drives them (Montiel et al., 2018), and their interactions with sea ice, as very little is known about the impact that these ocean waves have on ice breakup in the MIZ (Montiel and Squire, 2017). Intense and frequent storm activity generate these large ocean waves in the SO (Massaom and Stammerjohn, 2010; Kohout et al., 2014), which have enough energy to propagate hundreds of kilometres into the sea-ice cover (Vichi et al., 2019; Kohout et al., 2014). This is because the wave height is estimated to decay almost linearly for larger waves (> 3 m), while the wave height for smaller waves (< 3 m) decays exponentially (Kohout et al., 2014). These waves cause the sea ice to fracture into smaller floes and accelerates its melt season, which additionally increases the extent of open water regions (Montiel and Squire, 2017; Montiel et al., 2018). Vichi et al. (2019) suggests that these propagating waves delay the consolidation and maintains the mixed frazil-pancake field. This leads to lower sea-ice concentrations. Concurrently, sea-ice cover reduces the wave energy, through dissipative processes such as turbulence, and wave-induced collisions or the breakup of ice floes (Montiel et al., 2018), causing the wave energy to eventually die out (Lemieux et al., 2017; Dolatshah et al., 2018; Vichi et al., 2019) as the waves propagate into the sea-ice pack.

Dynamic processes include the motion and deformation of sea ice by winds and ocean currents (Thorndike and Colony, 1982), with the principal factor being the wind (Vihma et al., 1996), and other forces which come into play when the ice is drifting i.e. Coriolis force and inertial oscillations (see Section 1.7), internal ice stresses and sea-surface tilt (Thorndike and Colony, 1982). Sea-ice drift is a consequence of the wind forcing and ice-ocean interactions. Waves propagating through the ice leave behind a wake of broken ice floes, which subsequently become more susceptible to deformation by winds and currents (Kohout et al., 2014). Winds transfer momentum to sea ice, and under free drift conditions, i.e. the absence of internal stresses, sea ice changes from moving to the right of isobars to moving almost parallel to the isobars with a linear relationship to surface wind velocities, and therefore varies quickly with the changing wind fields (Wassermann et al., 2006). This simple linear ratio between the wind speed and the ice-drift speed is known as the wind factor, with the angle between the drift vectors being the turning angle. The well-known rule-of-thumb states that the wind factor is 2% (Leppäranta, 2011; Alberello et al., 2019). However, in pancake ice conditions, larger velocity ratios have been observed. Doble and Wadhams (2006) reported a wind factor of 3%-3.5% in the Antarctic, while more recently in the Arctic, Lund et al. (2018) reported wind factor values of up to 5% for pancake ice, but stated this was for the 17 m height winds as opposed to the regular 10-m winds.

The highest wind factor and turning angle values and correlation coefficients, between winds and ice drift, occur during low sea-ice concentration conditions (Thorndike and Colony, 1982;

Uotila, 2001; Alberello et al., 2019). In the Arctic MIZ, Wilkinson and Wadhams (2003) determined a mean wind factor of 2.7% for pancake ice, with a higher wind factor of 3.9% close to the ice edge, for ice concentration < 25%. Past observations have shown that the turning angle between the wind direction and the ice drift is on average between 0^o and 30^o, being positive in the northern hemisphere and negative in the southern hemisphere (Alberello et al., 2019).

Surface winds strongly depend on the cyclonic activity within the Antarctic Circumpolar Trough (Schlosser et al., 2016), and are the key thermodynamic and dynamic agents underlying sea-ice variability and trends in the SO (Vihma et al., 1996; Hobbs et al., 2016; Schemm, 2018). Cyclonic winds can lead to cyclonic trajectories in the sea-ice drift vector field within the Antarctic and the Arctic, however; ocean currents and internal stresses may produce deviations from the linear relationship between winds and ice drift (Wassermann et al., 2006). It has been predicted that there will be a continuation in the poleward shift of storm tracks over the SO (Massom and Stammerjohn, 2010; Kohout et al., 2014), resulting in increased winds over this region especially in austral summer and autumn (Massom and Stammerjohn, 2010), which will greatly affect sea-ice drift in the Antarctic, particularly in the MIZ due to its dynamical nature and the high frequency of storms across it.

On synoptic scales, winds that are associated with cyclones can be very intense, especially in the east Antarctic regions as cyclones are enhanced by strong katabatic winds (Wang et al., 2014). The low-pressure cells initially produce strong northerly flow at areas to the east of the cyclone centre, suppressing the katabatic winds. However, after the cyclone has moved east of that area, the strong southerly flow on the western side of the cyclone centre enhances the katabatic flow (Wang et al., 2014). These strong winds can enforce large atmospheric, and consequently, oceanic forcing on sea ice, with a large potential to cause rapid changes in extreme sea-ice conditions and drive sea-ice drift (Wang et al., 2014).

1.6. Sea-ice drift in the Southern Ocean

Sea-ice drift is a consequence of external forces – atmospheric and oceanic forcing – and internal ice stresses. The drift is altered by the impacts of the ice material properties, explicitly the thickness, strength and local ice concentrations (Heil et al., 2009). The net drift of sea ice is divergent as sea ice is advected north towards wider latitudinal zones (Vihma et al., 1996). Deviations from this are caused by transient cyclones passing over the sea ice in the MIZ, which may lead to areas of convergence and increases in ice thickness. Ice drift influences the sea-ice extent (SIE) and concentration (SIC) (detailed in Section 2.2) in many different ways (Schlosser et al., 2018). Divergence is associated with southerly winds blowing off the Antarctic coast, resulting in the offshore ice transport and an increase in the SIE, as well as the formation of leads and coastal polynyas near the coast. On the other hand, northerly winds lead to ice convergence, increasing the ice concentration and thickening by rafting and ridging (Schlosser et al., 2018). In this case, the northerly winds result in a decrease of the ice extent and an increase in ice thickness in the interior. The passage of polar cyclones cause the sea ice to undergo cyclical periods of convergence and divergence due to the fluctuating wind directions. In addition, strong westerly winds may also lead to the eastward redistribution of ice with a northerly component due to Ekman Transport (Schlosser et al., 2018).

Sea-ice drift and deformation are strongly dependent on the local ice and weather conditions (Itkin et al., 2017). The drifting speed of ice can be highly variable and ice can accelerate rapidly due to sporadic changes of wind speed and direction (Ackley et al., 2015). Therefore, synoptic events and strong winds have a great influence on the evolution of sea ice. However, our current understanding of the interactions between cyclones and sea ice is still limited (Vichi et al., 2019), as most of the existing literature on polar cyclones does not consider what happens when cyclones cross the MIZ.

1.7. Inertial oscillations of sea ice

Drift trajectories of sea ice often include circular or elliptical loops, inertial oscillations, superimposed on an approximately steady translation (McPhee, 1988). This is because sea ice is embedded within the surface of the ocean, experiencing the transfer of momentum from winds above and oceanic forcing from below. Simultaneous with the ocean, sea ice responds to atmospheric forcing at both the synoptic and sub-daily frequencies (the inertial response) (Heil et al., 2009). The inertial response of sea ice has been seen in both the Arctic (Gimbert et al., 2012; Lammert et al., 2009; Leppäranata et al., 2011) and the Antarctic (Doble and Wadhmans, 2006; Heil et al., 2009; Alberello et al., 2020), and have usually been observed in thicker sea ice (>1 m). Gimbert et al. (2012) however, found greater magnitudes of inertial oscillations for reduced sea-ice thickness, concentration and extent in the Arctic, during both summer and winter.

Inertial motion is associated within a rotating system. If a moving object or body, situated on a horizontal surface within a rotating system, is free of external forces, then within a rotating framework the body will follow a circular motion, known as inertial oscillations (Heil, 1999). Due to external forces, the body does not rotate in a circle indefinitely, but rather the inertial motion is superimposed onto other forms of motion (Heil, 1999). Inertial oscillations occur on spatial scales which are smaller than the Rossby radius of deformation, causing them to be a local phenomenon.

In the case of the ocean, inertial oscillations are caused by the rotations due to Coriolis acceleration. The first studies of inertial oscillations in the ocean were introduced by Nansen's observations made during the Fram's voyage along the Transpolar drift. Nansen (1902) determined that sea ice was drifting at a 30^{o} angle to the right of the wind direction. This is due to Coriolis force which acts perpendicularly to the moving particle, resulting in a deviation of the trajectory to the left (right) in the Southern Hemisphere (Northern Hemisphere). This deviation initiates the inertial oscillations that are characterised by a frequency of:

$$f_0 = 2\Omega sin\phi \qquad [1.1]$$

where ϕ is the latitude and Ω is the angular velocity of Earth. These inertial oscillations are close to a semi-diurnal frequency (2 cycles day^{-1}) in the Arctic (Gimbert et al., 2012), and in the Antarctic region (Alberello et al., 2019) due to high latitudes.

In the ice-covered ocean, inertial oscillations are caused by wind forcing events such as the passage of polar cyclones, which decrease within a few days (Gimbert et al., 2012). This dampening is due to internal stresses caused from mechanical interactions within the ice cover. These interactions involve the fracturing of ice, friction between floes and the shearing of leads, or ridge formation (Gimbert et al., 2012). Therefore, in reality, the amplitude of the inertial drift may vary from the theoretical value determined by Earth's rotation, since it depends on the magnitude of the forcing mechanism, in addition with decay caused from friction (Heil, 1999).

1.8. Aim and objectives

The aim of this study is to contribute to the understanding of the interactions between atmospheric forcing and sea-ice drift in the Antarctic MIZ, and to provide a better description of sea-ice dynamics in the MIZ by integrating existing data on the MIZ configuration with the atmospheric data and ice drift velocity. The ice drift data were collected from the S.A. Aguhlas II during the 2017 winter expedition, and were complemented by ERA5 atmospheric reanalysis data and AMSR2 ice concentration data with a spatial resolution of 3.125 km. The key objectives of this study are: (1) to investigate how storm conditions reshape the edge of the MIZ at synoptic scales (Vichi et al., 2019), (2) to investigate the relationship and correlation between surface winds and ice drift during pancake ice conditions, and (3) to investigate how wind forcing events generate inertial oscillations in sea ice, which dominate at the sub-daily frequencies.

As introduced in the previous sections, there have been many studies that have focused on understanding the role of atmospheric forcing on sea-ice drift and deformation in the Antarctic (Thorndike et al., 1986; Vihma et al., 1996; Uotila et al., 2000; Lindsay, 2002; Doble and Wadhams, 2006; Hutchings et al., 2012; Itkin et al., 2017) however, most of these studies have based their research on pack ice conditions. The lack of in situ data on winter ice drift and concentration in the SO marginal ice zone often makes satellite imagery products the only source of information (Vichi et al., 2019). However, these datasets are more suitable for understanding large-scale and long-term drift patterns (Kwok et al., 2017) rather than the features of the daily and sub-daily sea-ice drift, which is more likely to be affected by the passage of polar cyclones (Vichi et al., 2019). Therefore, this study provides a comprehensive analysis, by correlating in situ ice drift data and ERA5 atmospheric reanalysis data, to better understand and highlight the effects of ice-crossing polar cyclones on sea-ice drift in the Antarctic MIZ.

2. DATA AND METHODS

In this study, several types of data sources are used and combined to complete an extensive and precise analysis. Data measurements are assembled from drifting ice buoys, high-resolution sea-ice concentration satellite estimates and atmospheric reanalysis data. The data are then co-located to the temporal and spatial locations of the buoy measurements and combined to create the comprehensive analysis. The methods used to perform the analyses are presented later in this chapter.

2.1. In-situ measurements

In-situ sea ice data were gathered from the S.A. Agulhas II research ship which departed from Cape Town, South Africa, along the World Ocean Circulation Experiment (WOCE) I06 transect between the 1st July and the 20th July 2017. The vessel reached the marginal ice zone on the 4th July 2017 at 62.5^{o}S and 29.8^{o}E, at which point a polar cyclone was crossing the ice edge. Two autonomous devices, Waves In Ice Observation Systems (WIIOS) further known as buoys NYU1-2, were deployed on individual ice floes at 62.8^{o}S and 29.8^{o}E at midday on the 4th July, approximately 100 km from the ice edge (Figure 2.1(b)). These buoys recorded their location, temperature and wave spectral characteristics every 15 minutes (Vichi et al., 2019). From midnight on the 5th July three Trident Sensors Helix beacons (see Figure 2.1(a)), simply referred to as buoys U1-3, were deployed approximately 18 km east of NYU1-2 (U1-2) at 62.8^{o}S and 30.2^{o}E, and 24 km north of NYU1-2 (U3) at 62.6^{o}S and 29.9^{o}E, where they transmitted their location every 4 hours. These two sets of buoys were non-floating devices i.e. they sink when the ice melts, and their locations were used to deduce their ice drift speed (Vichi et al., 2019). To attain comparable results, buoys NYU1-2 have been resampled to a 4-hourly time interval.

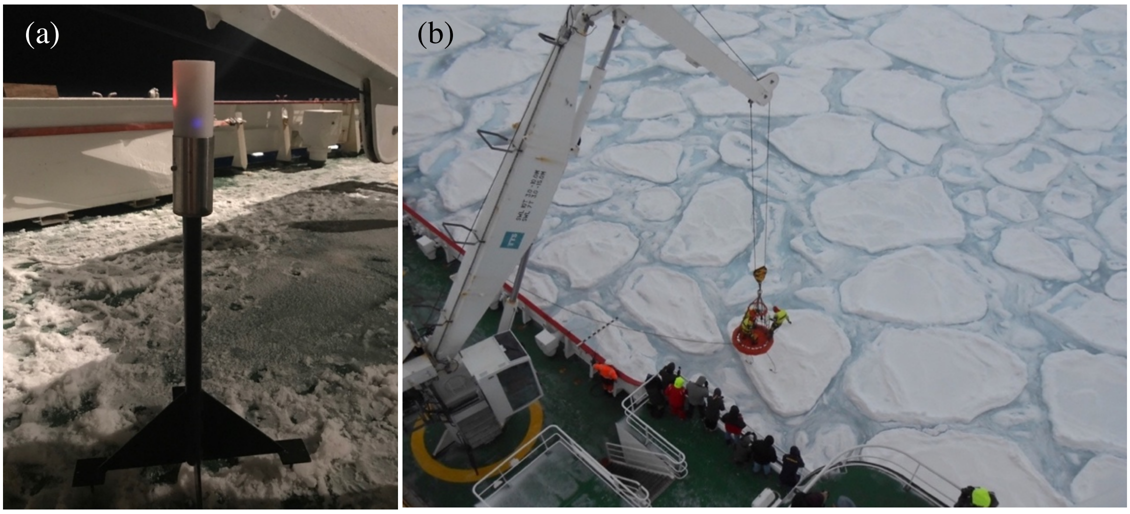

Figure 2.1: (a) A photograph of one of the Trident Sensors Helix beacons just before it was deployed. These buoys weigh approximately 25 kg each and sink when the ice melts. (b) The deployment of buoys on the 4th July 2017 on pancake floes using the ship crane. Photograph obtained from Skatulla (2017).

Buoy NYU1 only transmitted data for 8 days and 18 hours while buoy NYU2 ceased to transmit on the 20th July 2017, therefore the group analysis period is from the 4th to 20th July 2017, with NYU1 being shorter. The signal of the first Trident unit (U1) was only lost on the 1st December 2017 at 61.5°S and 55.0°E, presumably due to ice melting. The full duration of this buoy is additionally analysed in Chapter 4.

2.2. Satellite data

Sea-ice concentration (SIC) is defined as the percentage of the area of the ocean that is covered by sea ice, while the sea-ice extent (SIE) is the total area of sea-ice cover with an ice concentration greater than some threshold value (generally 15%) (Eayrs et al., 2019). This study uses SIC data from remote sensing, acquired from the passive microwave AMSR2 sensor at a 3.125 km horizontal spatial resolution and a daily frequency. Advance Microwave Scanning Radiometer-2 (AMSR2) is operating on the Japan Aerospace Exploration Agency's (JAXA) Global Change Observation Mission for Water GCOM-W1 spacecraft which was launched on the 18th May 2012 (JAXA, 2015), and is processed by Hamburg University using the ASI algorithm (Spreen et al., 2008). The ARTIST (Arctic Radiation and Turbulence Interaction STudy) sea ice (ASI) algorithm uses radiances with frequencies of 89 GHz (Spreen et al., 2008), producing a high spatial resolution of 3.125 km. The AMSR2 sensor has been retrieving sea-ice data since August 2012 using brightness temperatures (T_b); the temperature of a blackbody that would emit the same amount of radiation as the targeted body. Passive microwave radiometers are suitable, especially for monitoring polar regions, as they provide a good spatial and temporal coverage as well as they are almost independent of cloud coverage and daylight conditions (University of Hamburg, 2014). The ASI-AMSR2 sea-ice concentration data was obtained from ftp://ftp-projects.cen.uni-hamburg.de/seaice/AMS2/.

2.2.1. Comparison with different SIC data

In order to determine whether passive microwaves have a limited capability in detecting thin ice near the Antarctic ice edge, the SIC from two additional datasets, were obtained for the 1st December (see Section 4.1.1.), as the ice concentration appeared to be underestimated by the AMSR2 sensor at a 3.125 km horizontal spatial resolution.

The sea-ice concentration data from the AMSR2 sensor at a 6.25 km horizontal spatial resolution and a daily frequency was obtained from the University of Bremen (https://seaice.uni-bremen.de/data/amsr2/asi_daygrid_swath/s6250/). It uses the same ASI algorithm applied to the 3.125 km spatial resolution product however, a lower spatial resolution is produced and processed by the University of Bremen.

SIC data were additionally obtained from the Special Sensor Microwave Imager/Sounder (SSMIS), which is a 24-channel (19 GHz to 183 GHz), linearly polarized passive microwave radiometer system designed to attain a range of polarised atmospheric temperatures, moisture, and land variables under most weather conditions (NSIDC, 2018). The SSMIS satellite is operated by the Defense Meteorological Satellite Program (DMSP) and is part of the National Aeronautics and Space Administration's (NASA) Pathfinder Program (National Center for Atmospheric Research Staff, 2016). The SIC data are generated using the Advanced Microwave Scanning Radiometer – Earth Observing System (AMSR-E) Bootstrap algorithm, therefore producing a lower horizontal resolution (Cosimo, 1995). The daily SIC data were obtained from the Global Ocean 1/4^{o} Physics Analysis and Forecast Updated Daily product obtained from the Copernicus Marine Service (https://marine.copernicus.eu).

2.3. Atmospheric reanalysis data

ERA5 reanalysis, downloaded from https://cds.climate.copernicus.eu/, was used to obtain synoptic scale meteorological conditions given at an hourly frequency and with a 0.25x0.25 degrees horizontal spatial resolution. ERA5 is the fifth-generation European Centre for Medium-Range Weather Forecasts (ECMWF) atmospheric reanalysis of the global climate, containing a detailed record of the evolution of the global atmosphere from 1979 to the present. It provides a dynamically consistent estimation of the land, ocean and atmosphere state at every time step. A reanalysis product combines both model data and observations from around the world to create a globally complete and consistent dataset by using the laws of physics (Copernicus Climate Change Service., 2020). This key principle is known as data assimilation and is based on the method where every 12 hours (for the ECMWF) a previous forecast is combined with newly accessible observations, optimally, to produce an estimate of the atmosphere, known as analysis. Reanalysis is similar, but with a reduced resolution to allow for the establishment of a dataset which can go back several decades. ERA5 uses the 4D-Var data assimilation method, which includes the precise time of the observations and model evolution within the assimilation period (Copernicus Climate Change Service., 2020). This allows ERA5 to offer estimates hourly, which provides a detailed evolution of weather events, and is an improvement from ERA-Interim. The 10-metre u- and v-components of wind, the mean sea level pressure and the 2-metre temperature were downloaded at an hourly time step for the period of each set of buoys. Observations collected from shipborne data along the Good Hope Line in 2019 compared well with the corresponding data from ERA5 (Figure 2.2), which was also reported by Vichi et al. (2019) for the WOCE I06 transect however, both displayed an underestimation of the wind intensity. This is a known issue of reanalyses, which has been found in other Antarctic regions (Vichi et al. 2019).

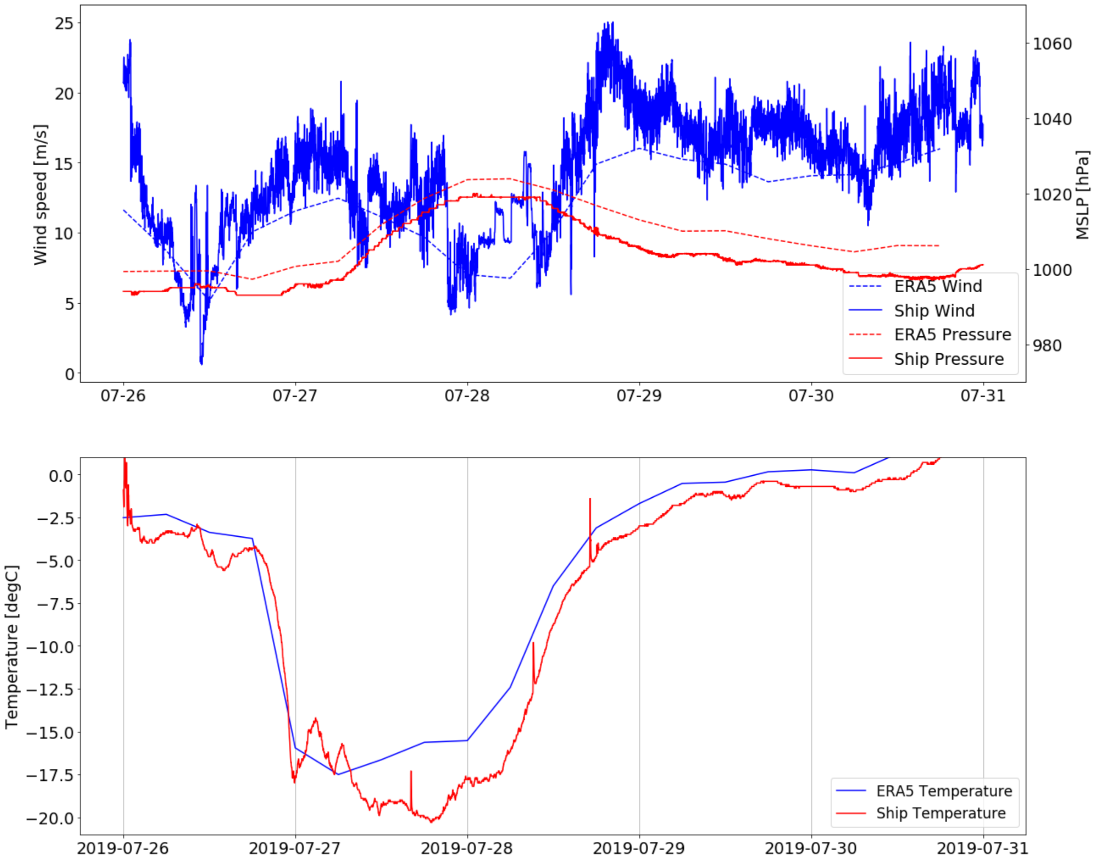

Figure 2.2: Shipborne atmospheric measurements of a). sustained wind and barometric pressure and b) temperature for the time period that the ship was located within the MIZ compared with the mean sea level pressure, 10-metre winds and 2-metre temperature derived from ERA5.

2.4. Methods

The 5 buoys are used to derive information on sea-ice drift in the MIZ. Details on ice drift kinematics are presented first, then the correlation between wind and ice drift is discussed, with a focus on the passage of polar cyclones, and lastly a power spectral analysis and a wavelet analysis are presented.

2.4.1. General Drift and Meandering

For each of the buoys, their latitude and longitude positions have been used to calculate their zonal u and meridional v components using the standard equations:

$$u = \frac{\Delta x}{\Delta t} \qquad [2.1]$$

$$v = \frac{\Delta y}{\Delta t} \qquad [2.2]$$

where Δx and Δy are the zonal and meridional distances travelled between successive points, and Δt is the time interval, in this case 4 hours or 14400 seconds. The modulus U (the scalar velocity) is calculated as:

$$U = \frac{\sqrt{\Delta x^2 + \Delta y^2}}{\Delta t} \qquad [2.3]$$

The direction of the buoys is calculated as the arctan of the meridional component divided by the zonal component for each successive position.

In addition to the drift velocity, the meander coefficient of each buoy acts as a primary quantitative measure for the kinematics of sea-ice drift (Vihma et al., 1996). As sea ice acts under the influence of changing winds, ice floes spend a substantial amount of their time turning and deflecting away from the general drift direction. Therefore, majority of ice drift trajectories greatly exceed the resultant distance, and the ratio between these two is given by the meander coefficient. It is calculated as:

$$\mathrm{M} = \frac{\mathrm{I}}{\Delta \mathrm{X}} \qquad [2.4]$$

where ΔX is the net transition of the buoy and I is the total trajectory length for the time period 4th July to 20th July 2017 for the group analysis (Chapter 3), and additionally for the 4-month drift of buoy U1 (Chapter 4). A higher meander coefficient indicates a more erratic trajectory, when winds are more intense and variable, whereas a value of 1 implies that the buoy moved in a straight line. Although the meander coefficient is a ratio between two distances, it is a function of the time period for which it is being computed and additionally is dependent on the sampling intervals of the position data (Heil et al., 2009).

2.4.2. Distance from the ice edge

The distance between the buoys and the ice edge, defined as the daily position of the AMSR2 0% ice concentration, is calculated as the geodesic distance of the nearest ice edge position to buoys' position for each day of the study period. This is illustrated in Figure 2.3 where the position of buoy U1 and the 0% SIC is shown for the 5th July. The arrow denotes the shortest distance between the ice edge and buoy U1.

The open ocean is defined as having an ice concentration of 0%, and to find the boundary between the sea ice and the open ocean, the most southerly 0% ice concentrations were determined for each longitude in the defined sample region, as seen in Figure 2.3. The geodesic distance is then computed by (1) using the Haversine function, which determines the great-circle distance between two points on a sphere given their longitudes and latitudes, and (2) by finding the minimum distance within the entire sample region for each day of the buoy's drift. This minimum distance is independent of where the buoy is located as it the nearest distance for the total 360° ice edge contour around Antarctica. Within the last 15 days of the full drift period, buoy U1 was active but outside the AMSR2 satellite-derived ice edge while the SSMIS data showed the buoy to remain within the sea-ice zone (further detailed in Section 4.2). Therefore, this calculation was additionally repeated using the coarser SSMIS ice concentration data for the last month of buoy U1's full drift.

The marginal ice zone is typically indicated as the region in which remotely-sensed SIC lies between 15% and 80%, however for the purpose of this calculation it has been classified as the 0% ice concentration contour, being the definite ice edge. The distance, however, must be interpreted with care as satellite products may be limited in reporting sea-ice concentrations at the ice edge as thin ice such as frazil and brash may also be interpreted as open water.

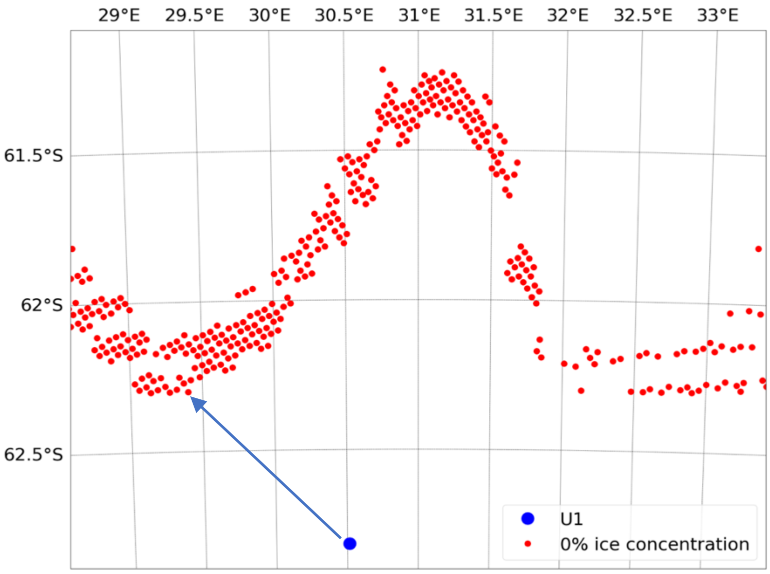

Figure 2.3: Finding the minimum distance between the buoy U1 and the ice edge for the 5th July. The red dots denote the AMSR2 0% SIC. The blue dots denote the position of buoy U1.

2.4.3. Co-location of ERA5 reanalysis data

In order to relate the atmospheric products to ice motion, the 10-m wind components, the 2-m temperature and the mean sea level pressure data from the ERA5 reanalysis product have been co-located to the buoys' time and location, using a tri-linear interpolation method (2D in space and 1D in time). These products have been downloaded with an hourly time interval, however after co-location, the atmospheric products have a time interval of 4 hours, at the buoys' location. The wind velocity and direction have been calculated using the same methods as the buoys' velocities, detailed in Section 2.4.1.

2.4.4. Identifying synoptic storm activity

Ice drift trajectories show many loops and meanders caused by varying winds during storm activity, highlighted in Section 2.4.1. To investigate the impact of these storms with varying durations and intensities, several case studies have therefore been identified. During the initial sample period, 4th July to 20th July 2017, Vichi et al. (2019) identified an intense polar cyclone which developed at the ice edge impacting the sample region, and was followed by 4 additional cyclones of various intensities. These 5 storms are further analysed in Chapter 3. Additionally, several other case studies have been identified for buoy U1 during its 4-month drift, using a visual analysis method. This was achieved by visually examining the ERA5 mean sea level pressure and 2-m temperature fields at 4 hourly intervals for the full period of buoy U1 (see Figure 2.4).

Mid-latitude cyclones are synoptic scale low-pressure systems with cyclonic (clockwise in the southern hemisphere) flow and are driven by temperature gradients between the warm subtropics and the colder polar latitudes. One of their defining features is their asymmetric thermal structure which manifests clearly in the fronts which define the cyclone (Martin, 2013). Therefore, the cyclones were identified by low-pressure troughs located near buoy U1 (see Figure 2.4), with a minimum low pressure of < 970 hPa, and an increase in air temperature to near melting point on the eastern flank of the cyclone. Vichi et al. (2019) found that air temperatures increased rapidly to values near melting during the onset of a polar cyclone and returned to -15^{o}C around 2 days later.

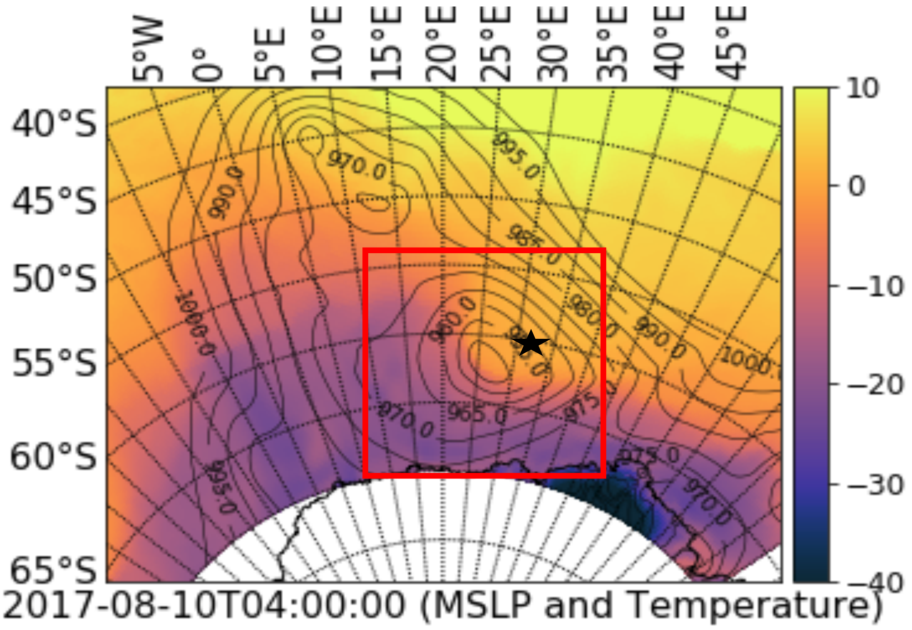

Figure 2.4: Air temperature (°C) and pressure fields (hPa) are plotted and the used to manually identify storms affecting ice drift of buoy U1. The red square highlights the storm event. The black star indicates the location of buoy U1 for 10th August 2017.

Once these storms have been identified, the dates when these storms were nearest to buoy U1 were calculated by using Python's geodesic distance function and Python's indexing method. The geodesic function finds the shortest distance between the centre of the low-pressure cell and the buoy. Low pressure systems that are identified are correlated to the loops and meanders of buoy U1's trajectory and studied according to the ice drift characteristics; the trajectory, the meander coefficient, the wind factor, the turning angle and the correlation coefficients.

2.4.5. Correlation between buoy drift and wind

Momentum transfers from surface winds to the sea ice can be defined using a simple linear ratio, the wind factor (detailed in Section 1.5.), with a turning angle between the wind and the ice (Doble and Wadhams, 2006). The wind factor α and turning angle θ were estimated using a least squares regression method adopted from Kimura and Wakatsuchi (2000), and assuming the sea ice was in free drift. Here, the variables U_a, V_a, and u_i, v_i denote the zonal and meridional components of wind and ice respectively. The index of the discretised series of wind and ice drift is denoted by k, with n being the upper bound of the summation. These equations can be written as:

$$\theta = \arctan\left[\frac{\sum_{k=1}^{n}\{U_a(k)v_i(k)\}-\sum_{k=1}^{n}\{V_a(k)u_i(k)\}}{\sum_{k=1}^{n}\{U_a(k)u_i(k)\}+\sum_{k=1}^{n}\{V_a(k)v_i(k)\}}\right] \qquad [2.5]$$

$$\alpha = \frac{c_1+c_2-c_3+c_4}{\sum_{k=1}^{n}\{U_a^2(k)\}+\sum_{k=1}^{n}\{V_a^2(k)\}} \qquad [2.6]$$

where

$$c_1 = \cos\theta \sum_{k=1}^{n}\{U_a(k)u_i(k)\} \qquad [2.7]$$

$$c_2 = \sin\theta \sum_{k=1}^{n}\{V_a(k)u_i(k)\} \qquad [2.8]$$

$$c_3 = \sin\theta \sum_{k=1}^{n}\{U_a(k)v_i(k)\} \qquad [2.9]$$

$$c_4 = \cos\theta \sum_{k=1}^{n}\{V_a(k)v_i(k)\} \qquad [2.10]$$

From here, the vector correlation coefficient r_v can be calculated using the following equation by Kimura and Wakatsuchi (2000):

$$r_v = \frac{c_1+c_2-c_3+c_4}{\sqrt{\sum_{k=1}^{n}U_a^2(k)+\sum_{k=1}^{n}V_a^2(k)}\sqrt{\sum_{k=1}^{n}u_i^2(k)+\sum_{k=1}^{n}v_i^2(k)}} \qquad [2.11]$$

The vector correlation defines the goodness of fit between the two sets of vectors, which includes scaling, translation and rotation. In addition, the Pearson correlation coefficient $r_{X,Y}$ was also calculated to determine the linear relationship between the modulus of ice drift and wind:

$$r_{X,Y} = \frac{\mathrm{cov}(X,Y)}{\sigma_X\sigma_Y} \qquad [2.12]$$

where cov is the covariance, σ_X is the standard deviation of X and σ_Y is the standard deviation of Y, with X and Y being the modulus of wind and ice drift respectively.

2.4.6. Power Spectral Analysis

Alberello et al. (2019), using the same group of ice buoys, studied the correlation between ice drift and winds using buoy NYU1 for the 8 days and 18 hours. They reported that the ice drift was characterized by inertial oscillations of period 13.1±0.85 hours, which is close to the theoretical range of 13.5±0.05 hours at 62^o-63^oS.

Using the same dataset but this time with all 5 of the ice buoys, and the additional analysis of buoy U1 for its full duration, a power spectral analysis is computed for each buoy to further examine whether their velocity time series indicates a peak within the inertial frequency range for each buoy's given latitude range. The theoretical oscillation periods are given as:

$$T = 2\pi/f_0 \qquad [2.13]$$

yielding values associated with the latitude range of each buoy's drift, where f_0 is the inertial frequency (Equation 1.1).

The power spectrum of a time series describes the distribution of power (the measure of variance) with respect to the frequency contained in the analysed signal (Glover et al., 2011). It is a technique allowing the same information contained within the time domain to be displayed in the frequency domain, while still conserving the total power held within the signal.

To display the distribution of power in the frequency domain, a fast Fourier transform (FFT) is applied to the velocity time series of the buoys. The FFT is a mathematical procedure that changes the domain of a signal from the original (usually time or space) to a representation in the frequency domain or vice versa. Applying the FFT to the velocity time series allows for the analysis of how much variance is contained in frequency bands that can be associated with external forcing mechanisms. The FFT is performed for the time series with length n (length of times series) which creates a transform X that ranges from -fc to +fc with a value length corresponding to the length of the FFT. The critical frequency fc is the maximum observational frequency for a series (Glover et al., 2011), and is defined as $fc = 1/2\Delta t$.

The power spectrum can then be computed by multiplying the FFT elements by their complex conjugates because the Fourier transform values are generally complex quantities (Glover et al., 2011), meaning that they have both real and imaginary parts. The squared amplitude of a complex number is achieved by multiplying itself by its complex conjugate and is always real ($\in\mathbb{R}$). The power spectrum is normalized by dividing it by the length of the time series to make the total power the sum squared amplitude, given by:

$$\sum_{j=0}^{N-1} \left|x_j\right|^2 \qquad [2.14]$$

which is the most straight forward form. The ‘j’ denotes the use of complex numbers (where $i = \sqrt{-1}$). By using Parseval’s Theorem (Equation 2.15), which states that the total power in the time domain must be equal to the total power calculated in the frequency domain, the computations can then be checked to see if they conserve the power. If the time domain and frequency domain are equal to each other, then the power spectrum is correct.

$$\int_{-\infty}^{+\infty} |x(t)|^2 \, dt = \int_{-\infty}^{+\infty} |X(f)|^2 \, df \qquad [2.15]$$

From here the periodograms can be created, where the power in each frequency bin is the total power in that bin. To make a better estimate of the power spectra with a confidence limit of 95%, a PSD object is created. Welch’s method is one of the approaches used for spectral density estimations. It is an improvement on the periodogram spectrum method, detailed above, as it reduces noise in the estimated power spectra in exchange for reducing the frequency resolution.

A Hann window is used in this Welch spectral object as the data were in the form of a discretised time series. This window dampens the beginning and end of the time series to 0, and better defines the spectral peaks (Figure 2.5). The Welch object divides the time-based sample array into segments 256 samples long while setting the overlap between windows to 0 (Glover et al., 2011). This controls the amount of discrete frequency estimates, and computing the spectrum in this manner breaks the original series into 256 sample segments, wherein the remaining data are truncated. A PSD object is then created using the Welch spectrum object, the time series, the sample frequency and a confidence level of 95%. In order to create the plots, the PSD, frequencies and confidence intervals are then extracted from the PSD object. Even though the sample frequency f_s is specified, the ultimate limit to the frequency resolution is the Nyquist frequency, which is half the sample frequency. The power is further normalized from the peridogram on a per frequency basis and defined over the frequencies 0 to +fc (Glover et al., 2011).

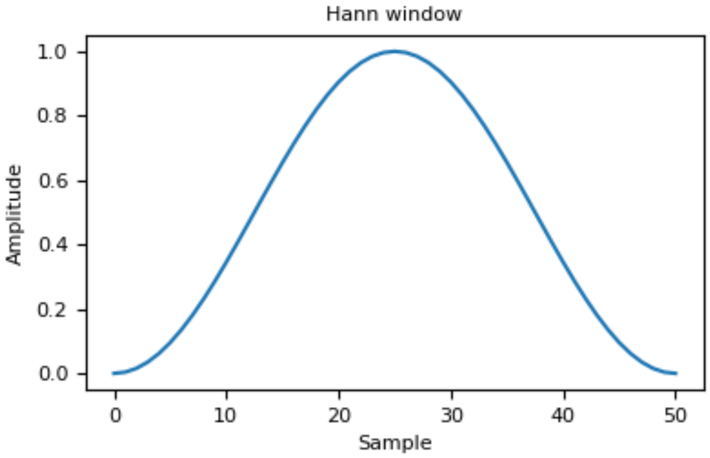

Figure 2.5: Hann window function which dampens the beginning and end of the sample.

2.4.7. Wavelet Analysis

The power spectral analysis is valuable in showing the periodicities within the velocity time series of ice drift. These periodicities can be connected to possible drivers i.e. winds and ocean surface currents, however this information is either presented in the time domain or the frequency domain, but not both. Therefore, to overcome this, a wavelet analysis is created, which yields information about the time series and frequencies together. By decomposing a time series into a time-frequency space, it allows for the determination of the dominant modes of variability, and how these modes vary in time (Torrence and Compo, 1998).

A wavelet is a wave packet of finite duration, with a mean value of zero ($\int_{-\infty}^{+\infty} \Psi(t)dt = 0$). The implementation of wavelets amounts to the translation of the wave packet along a time series, and at each step along the way it correlates the wavelet to just that section of the time series, where there is a wavelet signal (Glover et al., 2011). This produces a time series of how well a wavelet of that period correlates at each step. The Morlet wavelet, which is a common type of wavelet, has been used to do the analysis.

It is important to note the cone of influence (COI) which is the area of the wavelet spectrum in which the edge/boundary effect become important. These effects result from areas where the stretched wavelets extend further than the edge of the observation interval. Inside the COI, the information shown is accurate, while the outside the COI, the information of the wavelet spectrum should be treated with caution due to the potential edge effects.

2.4.7.1. Relationship between cyclones and inertial oscillations of sea ice

Inertial oscillations of sea ice are known to be caused by wind forcing events such as the passage of polar cyclones (detailed in Section 1.7). Therefore, the dates when the power within the wavelet spectrum, at different periods (frequencies), increases and dissipates are compared with the occurrences of ice-landing cyclones. Bursts of cyclic loops in the drift trajectories are connected to dates when cyclones, found in Section 2.4.4, passed near the buoys. These storm events are then compared to the periods at which the power increases, and when these increases occurred during the drift of the buoys. From here, the relationship between the low frequency forcing of cyclones and the occurrence of inertial oscillations of sea ice can be interpreted.

2.4.7.2. High-pass filtering of buoy U1

To further understand the mechanisms that excite inertial oscillations of sea ice, a high-pass Butterworth filter is applied to buoy U1, for the full duration of its time series, in order to filter out lower frequencies which dominate over a longer period. This further shows the periodicity of inertial motion and highlights the significance of the peaks at the inertial frequency range. The Butterworth filter is a type of signal processing filter which has a frequency response that is maximally flat in the passband and slopes towards zero in the stopband, in this case, the lower frequencies (Figure 2.6). A 12th order filter was used to remove frequencies below the cutoff frequency of 0.04 Hz, which corresponds to roughly a daily frequency, and passes the sub-daily frequencies where the inertial range is situated. From here a new wavelet analysis is created for the filtered time series using the same methods as before.

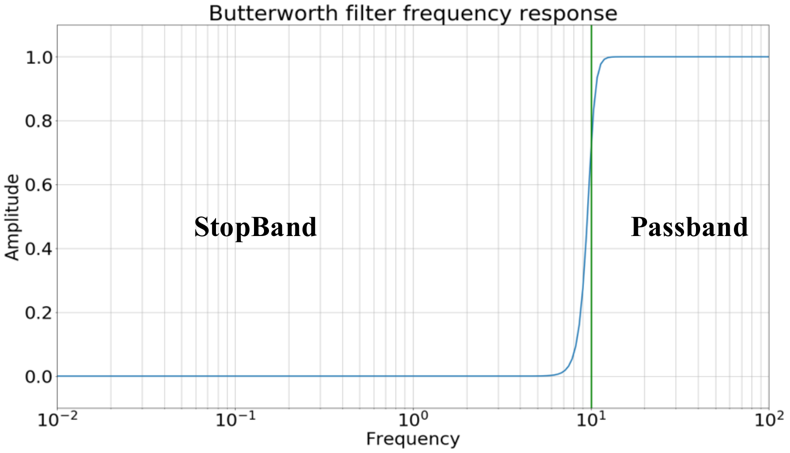

Figure 2.6: High-pass Butterworth Filter with the blue line being the filter response of nth order and the vertical green line indicating the cutoff frequency.

3. RESULTS: DRIFT MEASUREMENTS AND GROUP ANALYSIS

The results are presented as follows: first, a comprehensive analysis is presented describing the ice drift dynamics of the five buoys, and then the role of atmospheric forcing on ice drift during pancake ice conditions, from 4th July to 20th July 2017. These results will be discussed concurrently.

3.1. Environmental conditions

A polar cyclone developed along the ice edge on the 2nd July, where it progressed south-eastwards with a deepening core until complete cyclolysis on the 5th July. The minimum pressure was found to be 927 hPa with a maximum wind speed of approximately 15 m s^{-1}. Over an approximately 15-day period, four more cyclones of various durations and intensities impacted the MIZ during the time of the buoys' deployments (Figure 3.1). During the passage of each storm, wind speeds over the sea ice increased accompanied by increased air temperatures, which rose to near melting point before decreasing once again to around -10^{o}C to -20^{o}C after cyclolysis. The first storm is characterised by a longer period of increased temperatures until the second storm arrived. The second storm (6th July-8th July) bordered the ice edge, travelling over the open ocean just north of the buoys. The third and fourth storms (9th July-11th July and 11th July-14th July) had cyclogenesis over the marginal ice zone where the third storm had lysis south of the buoys and the fourth, north-west of the buoys. The final storm (19th July-20th July) had cyclogenesis north of the buoys, travelling along the ice edge where it disappeared north-east of the buoys. Vichi et al., (2019) classified three out of the five cyclones as being explosive events, which was shown by the normalised deepening rates (change in the core pressure over 24 hours weighted by latitude) being greater than 1. However, all five of the cyclone were strong storms, impacting the sea ice differently.

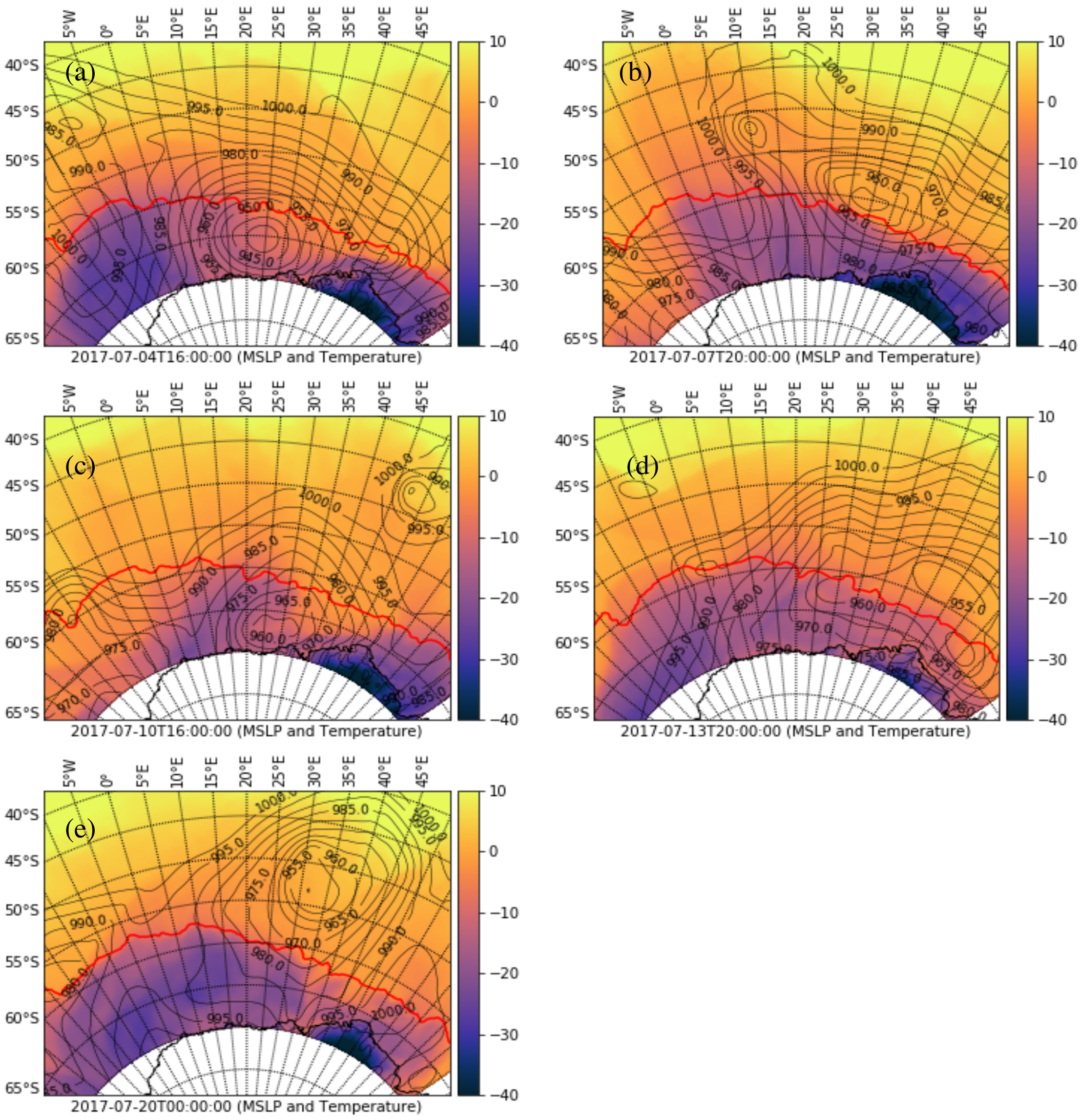

Figure 3.1: Environmental conditions of the 5 storms when they were the close to the buoys: (a) at 16:00 on 4th of July; (b) at 20:00 on 7th of July; (c) at 16:00 on 10th of July; (d) at 20:00 on 13th of July; (e) at 00:00 on 20th of July. The black contour lies indicates the ERA5 isobars in hPa. The purple-orange shading indicates the ERA5 2-metre air temperature in ^{o}C. The red contour denotes the 15% AMRS2 sea-ice concentration.

The area affected by the cyclones extends deep into the ice cover. This can be seen by the air temperature and pressure fields showed in Figure 3.1. Warm air was advected southwards on the eastern flank of the cyclones, while cold air was advected northwards towards the equator on the western flank of each cyclone (Schlosser et al., 2018). As the cyclone travels eastwards across the ice edge, it warms the overlying air temperatures, generates large waves and forces the ice edge southwards, while also enhancing the northwards katabatic flow of cold air from the pole on the western flank (Vichi et al., 2019), which drives ice formation and the forces the ice edge northwards. This causes the MIZ concentration to be rearranged in a clockwise rotation. Although the four additional storms were less intense than the extreme event, they carried substantial energy in their winds and still contributed in the reshaping of the ice edge at the synoptic scale (Vichi et al., 2019).

3.2. Buoy drift

Figure 3.2 shows the trajectories of the five buoys from deployment until 20th July 2017 superimposed on the AMSR2 sea-ice concentration. After deployment on 4th July, buoys NYU1-2 initially travelled in a southeast direction, forced by the first cyclone when wind speeds reached ≈15 m s^{-1} (eastwards). After the deployment of the trident buoys (U1-3), on the 5th July, all five of the buoys travelled in a northeasterly direction before switching northwesterly under the direction of the second cyclone, with maximum wind speeds also reaching ≈15 m s^{-1}. Impacted by the third and fourth storms which generated wind speeds of ≈10 m s^{-1}, the buoys all drifted east; first drifting slightly southwards and then northwards. During the last storm, also with a wind speed maximum of ≈10 m s^{-1}, the buoys switched to drift northwesterly.

Even with buoy U3 which was deployed away from the main group, the buoys remained close together and followed in a similar drift track over the ≈15 days, containing four distinct east-west alternating phases. These phases are divided by sharp turns and loops, showing a great amount of meandering as a result of varying winds. Although similar, these buoys present their own individual trajectory, independent of each other due to minimal/absence of internal stresses in pancake ice (Leppäranata et al., 2011). U1 began to diverge from the main group of buoys on the 14th July and travelled more south during the last clockwise loop, and while U3 displays a similar trajectory pattern to the rest buoys, it contains a more prominent northward component during its drift period.

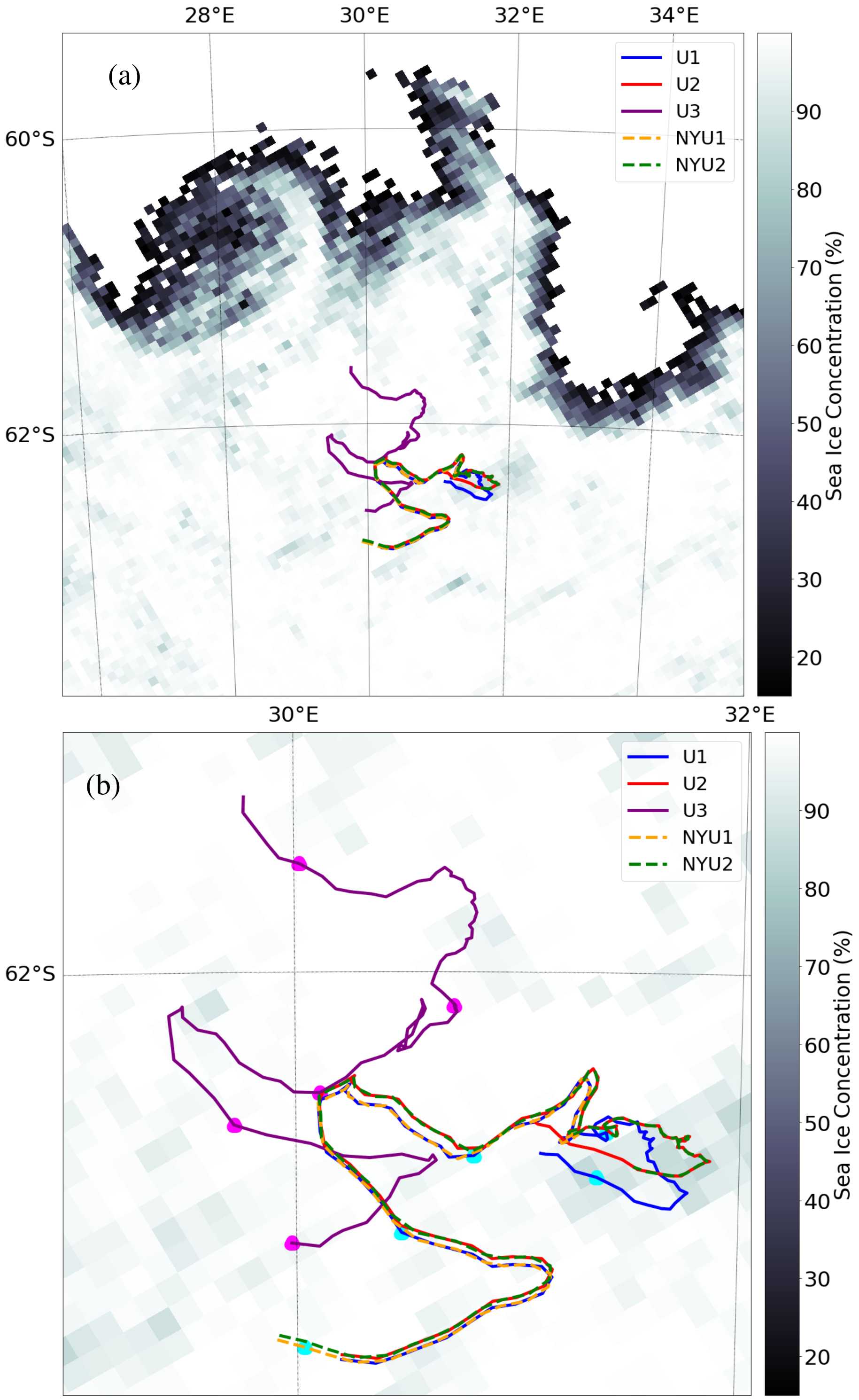

Figure 3.2: (a) The trajectories of the five buoys from deployment until the 20th July (13th July for NYU1), and (b) the trajectories highlighting when each storm was closest to the buoys. The purple circles indicate when each storm was closest to buoy U3, and the light blue circles indicate when the storms were nearest to the rest of the buoys. The shadings show the AMSR2 sea-ice concentration with values between 15%-100% on the 20th July.

The buoys had a mean scalar drift speed of 0.23 m s^{-1} for buoys U1, U2 and NYU2, 0.25 m s^{-1} for buoy U3, and 0.32 m s^{-1} for buoy NYU1. Buoy NYU1's speed is over 50% higher than the previously reported daily averages for this region of the SO (Alberello et al., 2020). However, all buoys have values which are similar to that of Doble and Wadhams (2006) who reported scalar drift speeds between 0.22 and 0.35 m s^{-1} for the central Weddell Sea. The mean scalar wind speed was 7.81 m s^{-1} for buoy U1, 7.91 m s^{-1} for U2, 8.27 m s^{-1} for U3, 10.17 m s^{-1} for NYU1 and 8.08 m s^{-1} for NYU2. Buoy NYU1 spent a larger proportion of its time, relative to the other buoys, under the influence of storms causing it to have the greatest mean scalar speed. The scalar speed of each buoy was largely determined by its u-component (east-west, approximately parallel to the ice edge), with buoy U3 having the largest v-component.

3.2.1. Ice edge effects on ice drift

According to observations aboard the ship (Figure 2.1), the five buoys were deployed in unconsolidated pancake ice conditions making up approximately 60% of the ice surface, with floes of 3.2 m in diameter (Alberello et al., 2020). The rest of the ice surface was made up of frazil ice in between the floes. The in-situ ice observations in the MIZ only lasted for around 24 hours, when the ship travelled back to Cape Town. The buoys were deployed ≈100 km directly south of the ice edge. This entry into the MIZ was characterised by a localised protrusion, complicating the interpretation of the distance from the ice edge calculation shown in Figure 3.3. Here, the ice edge was calculated as the distance between the nearest point along the ice edge to each buoy, detailed in Section 2.4.2. It is noted that the buoys remained within 100 km from the ice edge, even during the ice expansion. Alberello et al. (2020), using the same dataset, reported that the buoys were always in 100% ice concentration, according to the remotely sensed AMSR2 SIC.

Figure 3.3 shows that there was a consistent decrease in the distance of the main cluster of buoys from the ice edge, until the 11th July, followed by a gradual increase until just before the last storm on the 19th July. On the other hand, buoy U3 indicates a decrease in distance during each storm followed by a lesser increase before the passage of the next storm. This downward, yet varying, trend of buoy U3 continued until the 14th July, where the distance from the ice edge is affected by the passage of the fourth storm, unlike the rest of the buoys. This would be due to its more north-western position; undergoing slightly different wind and ocean forcing. From the 14th July, buoy U3 follows the same trend as the other buoys.

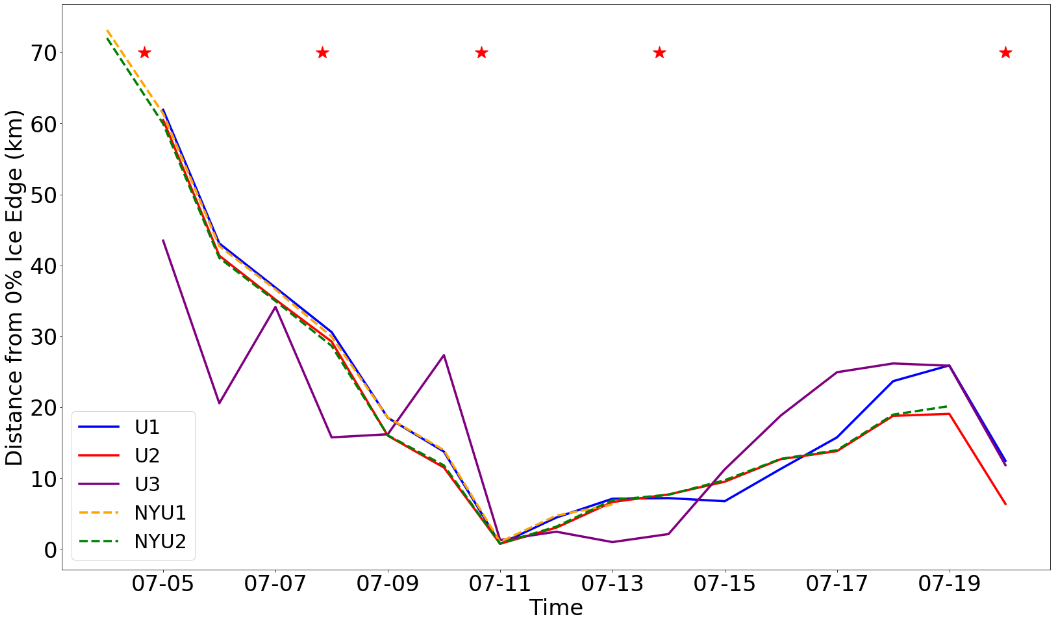

Figure 3.3: Distance between the buoys and the ice edge defined by 0% sea-ice concentration. The red star symbols indicate the time when the storm cores were closest to the buoys' location.

Near the ice edge, wind stress can be affected by several factors such as the surface roughness and compactness of the sea ice (Doble and Wadhams, 2006). These spatial variations of wind stress may give rise to the divergence and convergence of sea-ice drift. Therefore, buoy U3 being located closer to the ice edge would have experienced an altered wind and ocean forcing compared to the rest of the buoys, and this is seen by its slightly different trajectory pattern in Figure 3.2.

During the passage of the storms, warm air was advected poleward onto the sea ice, pushing the ice edge downwind as the sea ice was compressed. Winds and ocean currents can compact the sea ice to produce a relatively narrow ice edge region (Heorton et al., 2014). The buoys also have a constant northwards velocity component which may additionally reduce the distance of the buoys from the ice edge. However, after the 11th July for the main cluster of buoys and the 14th July for buoy U3, the buoys' distance from the ice edge increases as the MIZ relaxes from a more compact state, and the ice extent grows as it would during the austral winter expansion.

As the buoys were located close to the sea-ice edge, they remained within the MIZ which is approximately 5-100 km in width (Heorton et al., 2014), and is charcterised by ice floes which have been broken by wave energy due to their close proximity to the open ocean. Vichi et al.

(2019) reported waves present in the sea-ice field even during the period of storm quiescence after the 14th July, which coincided with a decrease in air temperatures and an increase in distance of the buoys from the ice edge. The intense waves-in-ice activity suggests that the sea ice never reached pack ice conditions but rather maintained the frazil-pancake ice conditions (Alberello et al., 2020), even with 100% SIC. This allows for the assumption of free-drift, where ice drift is under the influence of winds and ocean surface currents only (Gimbert et al. 2012; Heorton, 2019).

3.2.2. Quantitative measures of ice drift

In addition to the qualitative analysis describing the buoy array, the overall drift pattern of the individual buoys is described by their meander coefficients. The meander coefficients have been calculated for the ≈15-day period, except for buoy NYU1 which only drifted for 8 days and 18 hours, resulting in the lowest meander coefficient (Table 3.1). This is supported by an additional calculation of buoy U1 for the ≈9-day period, giving a coefficient of 2.94, which can be seen in Figure 3.4. Figure 3.4 shows the time series of the meander coefficient for all five buoys, indicating how each buoy deviated from a straight path over time. It highlights how the meander coefficient is a function of time (as detailed in Section 2.4.1), and also how storm conditions occurring at specific times affect the trajectory of each buoy. It is noted that although the meander coefficient of buoy NYU1 cannot be compared to the rest of the group, due to a shorter duration, it is an informative measure of ice drift suggesting that the ice drift deviated from a straight-line path, under the influence of erratic winds.

Table 3.1: Total distance travelled from deployment to 20th July 2017

Buoy	Total trajectory length (km)	Net Distance (km)	Meandering Coefficient (M)
U1	309.50	65.65	4.86
U2	315.16	69.62	4.67
U3	329.60	108.98	3.22
NYU1 (only until 13th July 2017)	239.49	85.18	2.88
NYU2	305.89	90.12	3.46

In Figure 3.4, it can be seen that the meander coefficient follows a general increase over the ≈15-day period. The meander coefficient largely increased with the onset of each cyclone, with buoy U3 typically having the largest meander coefficient. After the fourth cyclone, all five of the buoys displayed similar meander coefficients which remained constant until the arrival of the final storm. However, at the end of the drift period, while the other buoys' meander coefficient increased, buoy U3's meander coefficient dropped during the last storm. Referring back to Figure 3.2, it can be seen that during the last cyclone, buoy U3 travelled north-westerly with little deviation or meandering, whereas the other buoys travelled in a cyclonic loop. This difference in the buoys drift pattern therefore affected the outcome of their meander coefficients.

Although meander coefficients from other studies cannot be directly related, due to different deployment durations and sampling frequencies, it is informative to analyse these meander coefficients in light of the other studies. Heil et al. (2009) derived low meander coefficients for the East Antarctic which indicated that the ice drift was rather part of a large-scale forcing system – the Antarctic coastal current. However, this buoy array displays sufficiently high coefficients, inferring to the erratic nature of ice drift during the analysed period. This suggests that the drift patterns are significantly related to atmospheric forcing, where varying winds have a great effect on ice drift.

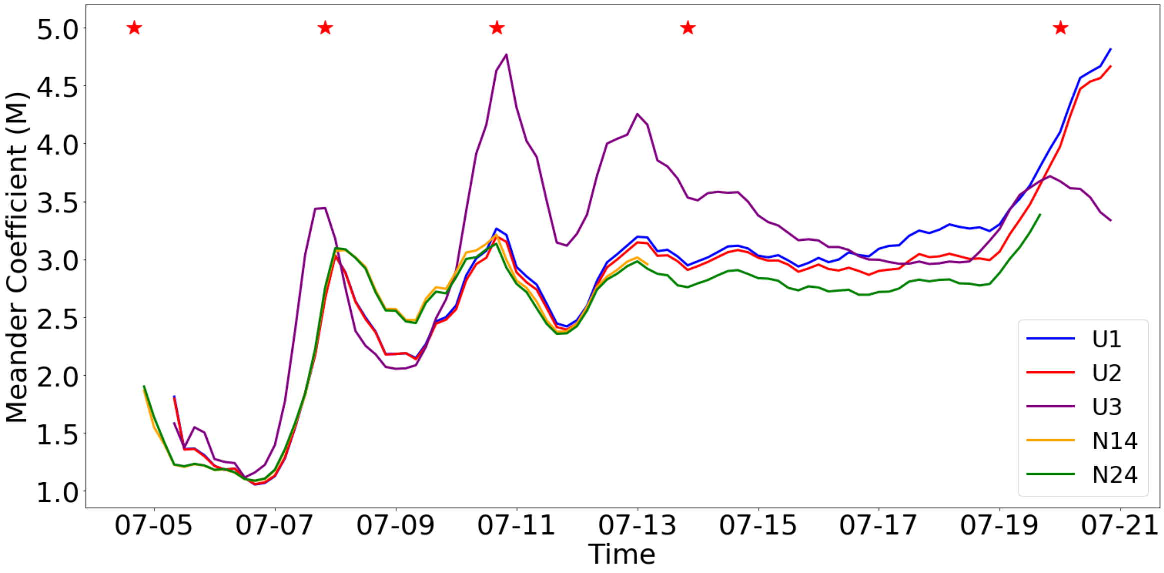

Figure 3.4: Time series of the meander coefficient for each buoy. The red star symbols indicate the time when the storm cores were closest to the buoys' location.

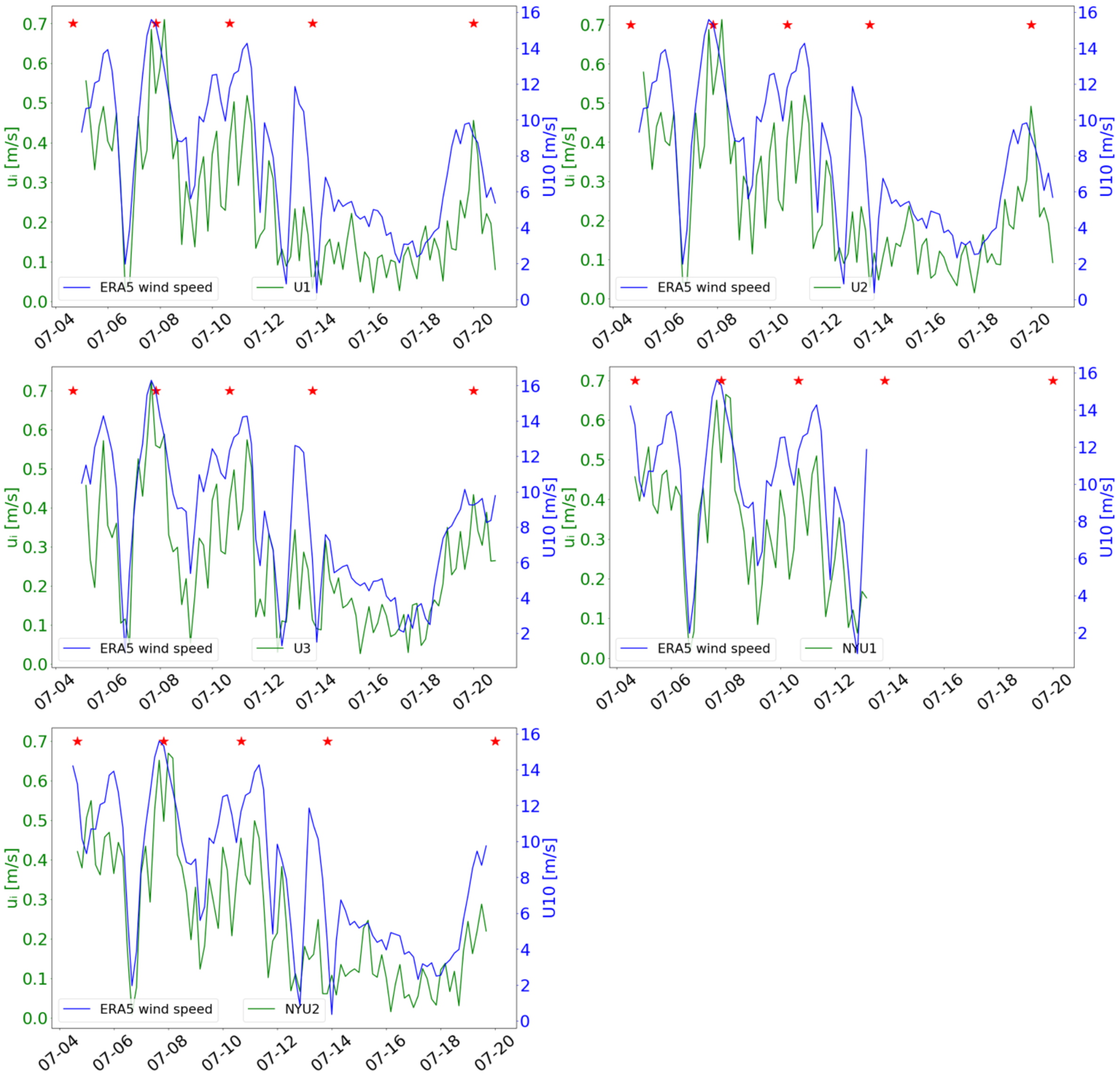

Figure 3.5: Sea-ice drift speed and wind speed measured at the locations of the 5 buoys. The left axis (green) denotes the buoy speed and the right axis (blue) denotes the wind speed. The red star symbols indicate the time when the storm cores were closest to the buoys' location.

During all cyclones, except for the fourth cyclone, the ice drift speed for each buoy notably increased (Figure 3.5). The increase in ice drift speed was observed around one day after the increase in wind speed, and is almost identical for all five of the buoys in the cluster. The qualitative response of the ice to wind forcing is due to free-drift conditions of the ice floes. The floes, on which the buoys were deployed, were not drifting relative to one another at scales between 5-100 km (Vichi et al., 2019), however they show very similar velocity time series.

The largest drift speed for all of the buoys was not observed during the first cyclone but rather the second. The waves generated by the first cyclone were the most intense (Vichi et al., 2019), causing the sea ice to fracture into smaller floes, predisposing them to deformation and high drift speeds by the strong winds of the second cyclone. The maximum instantaneous ice drift speed of buoy NYU1 was 0.75 m s^{-1} during the second storm, which is the fastest recorded for Antarctic pancake ice drift (Alberello et al., 2020). Large ice drift speeds have previously been reported in the Central and Western Weddell Sea (Vihma et al., 1996; Doble and Wadhams, 2006), but these studies did not relate the large drift speeds to the occurrence of cyclones.

3.3. Correlation between buoy drift and wind

To investigate the physical control of winds on sea-ice drift in the MIZ, the observed sea-ice speed and direction for each buoy were compared with the ERA5 wind vectors. All buoys displayed a mean wind factor value of ≈3% (Table 3.2). This is higher than the typical rule-of-thumb of 2%, detailed in Section 1.5., however the Antarctic MIZ is known for its high velocity ratios. Pancake ice conditions allow the floes to readily follow changes in atmospheric forcing, particularly during storm events, when wind speeds are high. In support of these findings, Doble and Wadhams (2006) reported a wind factor of 3-3.5% for Antarctic pancake ice conditions. Additionally, Alberello et al. (2020), using the same dataset, reported a wind factor value of 3.3% for buoy NYU1, but with a 15-minute sampling interval.

Table 3.2: Principal Characteristics of the Drift Dynamics

Buoy	Wind Factor (%)	Turning Angle θ (°)	Linear Coefficient of Determination (R^2)		Vector Coefficient of Determination (R_v^2)
			DIR	SPEED	
U1	2.86	-24.02	0.39	0.67	0.74
U2	2.92	-24.32	0.40	0.68	0.76
U3	2.82	-27.09	0.18	0.72	0.74
NYU1 (only until 13th July 2017)	3.09	-23.54	0.41	0.65	0.84
NYU2	2.88	-22.18	0.34	0.72	0.79

The time series of the wind factor and turning angle of buoy U1, detailed in Figure 3.6, shows that the highest speed ratios reached 5-6%, while during the periods between cyclones, the wind factor was generally 2-4%. Only buoy U1 is displayed as all buoys have similar mean wind factor and turning angle values. The large speed ratios of buoy U1 coincided with periods of maximum ice drift speeds during storm activity, and during periods when the wind speed approached 0 m s^{-1}, causing the ice drift to almost stop (see Figure 3.5). The peak wind factor occurred on the 18th July during the period of low winds, shown in Figure 3.7. Figure 3.7 shows the stick plots of buoy U1 for both the wind and ice drift using the wind convention, where wind and ice drift are reported by the direction from which they originate. It demonstrates the rotation and sharp changes in the wind, which caused buoy U1 (and the other buoys) to drift and meander. The wind factor relies on the qualitative response of ice drift to wind forcing. As the wind speed increases, the ice drift speed follows, with the same occurring when wind speed decreases. It is a mathematical ratio between the wind and ice drift speeds, therefore a high wind factor value does not necessarily indicate storm conditions or high winds, and should not be used below some threshold value.

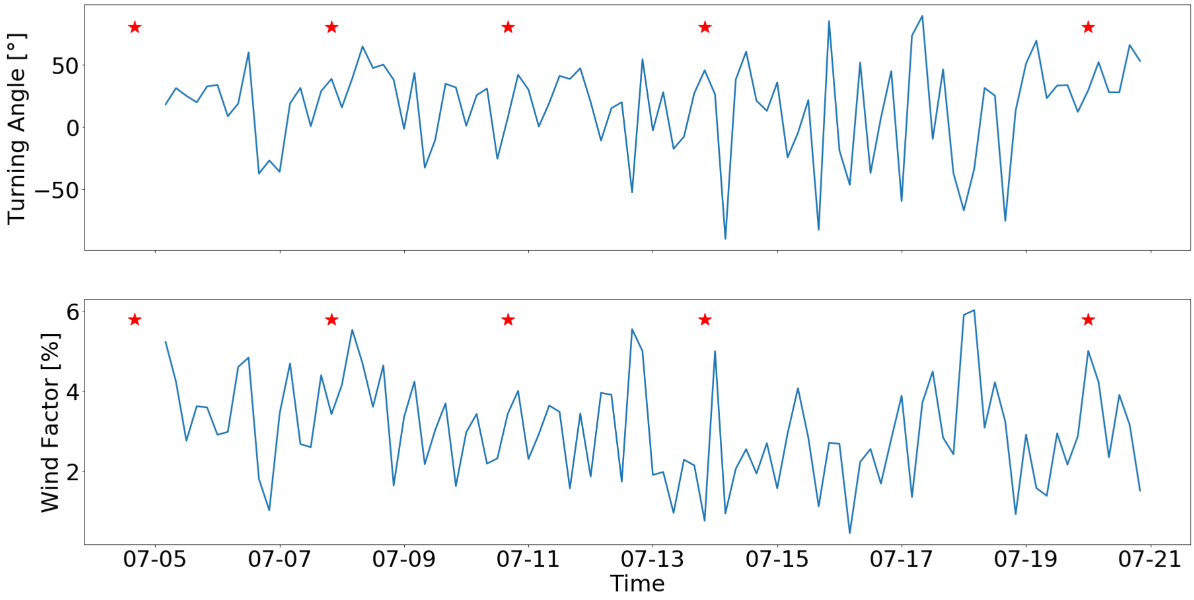

Figure 3.6: Time series of the turning angle and wind factor of buoy U1. The red star symbols indicate the time when the storm cores were closest to the buoy's location.

Vihma and Launianen (1993) observed that the wind factor is greatly dependent on the location of the buoys with respect to the ice edge, and since the buoys remained within 100 km from the ice edge (Figure 3.3), the lower ice compactness increased the buoys' wind response, resulting in high wind factor values.

Table 3.2 displays the mean turning angle of each buoy which lies between ≈-22° and ≈-27°, falling within the typical range of 0° to -30° for the Southern Hemisphere (Leppäranta, 2011). Alberello et al. (2020) reported a mean turning angle of ≈-25° for buoy NYU1, using the methods detailed in Leppäranta (2011), and is very similar to that found in this study (-23.54°) using the least squares method (detailed in Section 2.4.5.). This dataset shows generally large variations between -50° to +50° (see Figure 3.6), with the largest variations ($|\theta| > 90^\circ$) occurring during the period of quiescence. During each cyclone, the turning angle is always positive between 0°-50°, and unlike the wind factor, the turning angle follows the pattern of cyclone activity. Stronger winds, during the passage of cyclones, decrease the turning angle, while the largest turning angles occurred during periods of reduced wind speeds ($|U| < 6$ m s^{-1}), when wind stresses were small (see Figure 3.7). Large ranges are consistent with Uotila et al. (2000) who reported value from -20° to +60° in the Weddell Sea, and Lund et al. (2018) who reported values from -23° to +83° during storm conditions in the Arctic.

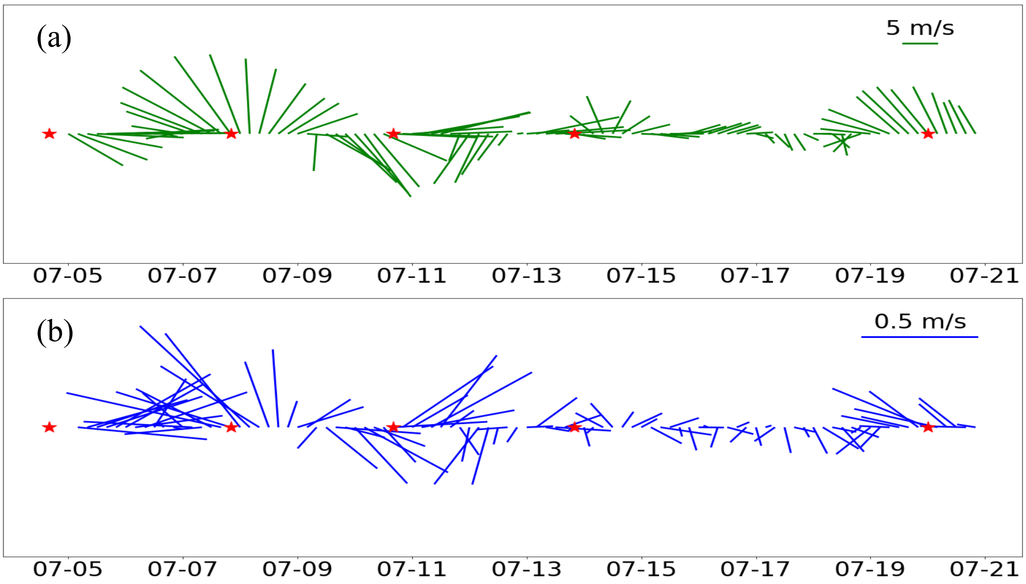

Figure 3.7: Stick plots showing the time series of (a) the interpolated ERA5 wind vectors at buoy U1's position and (b) the ice drift vectors of buoy U1. The red star symbols indicate the time when the storm cores were closest to the buoy's location.

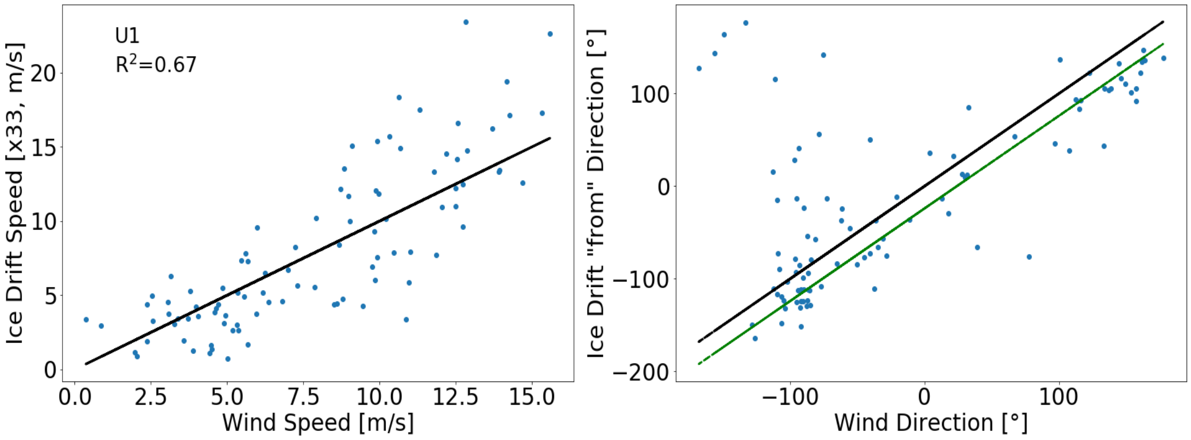

Figure 3.8: Scatterplots (left) of ice drift speed as a function of wind speed and (right) of ice drift direction as a function of wind direction of buoy U1. The black line is the 1:1 line. The green line is the turning angle at -24.02°.

The relationship between buoy U1 and the wind vectors is shown in Figure 3.8; the rest of the buoys are equivalent and are detailed in Appendix A (Figures A and B). The ice drift speeds have been multiplied by 33, so that the 1:1 line represents an ice drift of 3% of the wind speed, being the approximate wind factor for this buoy array. Many of the ice drift speeds are above and below this line, with a good correlation of $R^2 = 0.67$ (Table 3.2). This is the linear coefficient of determination, which is the proportion of the variance in the ice drift speed that is predictable from the wind speed. Alberello et al. (2020) reported a slightly lower value of $R^2 = 0.56$ for buoy NYU1, but with a higher frequency sampling interval, and Doble and Wadhams (2006) reported a value of $R^2 = 0.5$ for Antarctic pancake ice conditions. They however, did not consider the relationship between ice drift and wind direction. Figure 3.8 shows that in terms of ice drift and wind direction, the points are generally closer to the 1:1 line except for the top-left corner, leading to a lower linear coefficient of determination of $R^2 = 0.39$, which is similar for the rest of the buoys except for buoy U3, which can be attributed to its more northerly position (see Table 3.2). These outlying points mostly occurred during the period of quiescence (14th-19th July) when the wind stresses were small (see Figure 3.7), and when the turning angle range was the largest (see Figure 3.6).

The vector R_v^2, which defines the relationship between ice drift and winds by considering both speed and direction, is calculated for all buoys (detailed in Section 2.4.5). The vector R_v^2 values are higher than the linear R^2, for each buoy (Table 3.2), and although the vector R_v^2 cannot be fully compared to the linear R^2, it indicates that the relationship between ice drift and wind direction is significant. This demonstrates that the wind not only governs sea-ice drift speed, through the transfer of momentum, but also governs the trajectory path of each ice floe. Both methods however, show a good correlation between ice drift and winds due to the high wind response of pancake ice floes, and suggests that the winds contribute heavily towards the observed ice drift, with ocean currents have a small contribution.

3.4. Spectral Analysis of ice drift

Figure 3.9 shows the spectra of both the wind (blue) and ice drift velocities (orange) of buoy U1. The other buoys reflect very similar results and are found in Appendix A (Figures C-F). The wind velocity spectrum of buoy U1 forms an energy cascade for the 15-day period, while the ice drift velocity forms an energy peak at a frequency just below two cycles day^{-1} (13.57 hours), indicated by the red vertical line. The period at which the energy peaks is close to the inertial range of 13.47-13.59 hours, at 63^{o}-62^{o}S respectively, defined by the Earth's rotation. Buoy NYU1 has the lowest estimated energy peak at a period of 13.00 hours (Table 3.3), which is due to its shorter drift period of only ≈9 days. However, all buoys have indicated a similar inertial response to their theoretical range. The peaks therefore denote inertial oscillations within the ice, and is seen in all five of the buoys. Vihma et al. (1996) and Geiger et al. (1998) both reported an inertial response of sea ice at a period of ≈12 hours, for the west Weddell Sea, while Heil et al. (2009) found an inertial response occurring at 1.82 cycles per day (13.19 hours) for East Antarctica.

Table 3.3: Inertial Response of Ice Drift

Buoy	Inertial Oscillation (estimated)	Inertial Oscillation (Theoretical)
U1	13.57 hours	13.59-13.47 hours (Lat: 62◦-63◦)
U2	13.57 hours	13.59-13.47 hours (Lat: 62◦-63◦)
U3	13.57 hours	13.72-13.47 hours (Lat: 61◦-63◦)
NYU1 (only until 13th July 2017)	13.00 hours	13.59-13.47 hours (Lat: 62◦-63◦)
NYU2	13.48 hours	13.59-13.47 hours (Lat: 62◦-63◦)

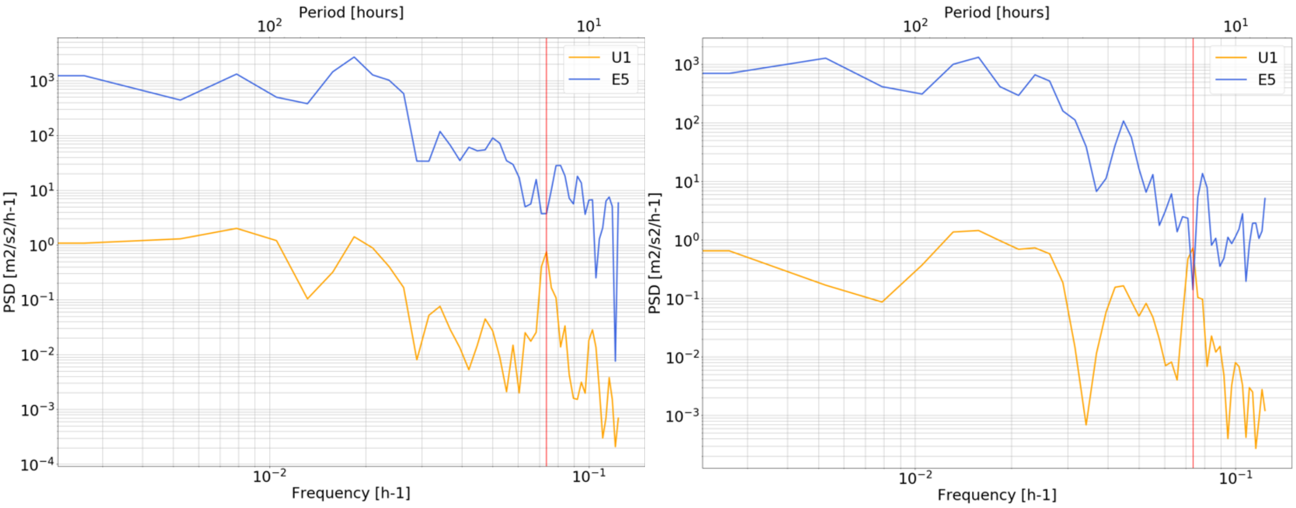

Figure 3.9: Power Spectral Density corresponding to the (left) zonal component of ice drift velocity and the (right) meridional component of ice drift velocity for buoy U1. The orange line indicates buoy U1 and the blue line indicates the ERA5 winds. The vertical red line indicates the peak associated with inertial oscillations (13.57 hours).

Inertial oscillations are generally associated with rapid changes in wind stress, i.e. the passage of storm fronts, which occur on time scales of about five days (Thorndike, 1986), in the SO. As stated in Section 3.1., the first four cyclones were the found to be closest to the buoys every three days, while the fifth cyclone followed seven days later. This cyclone frequency is seen in the PSD of the u and v components of wind (Figure 3.9). The majority of the power within the wind velocity time series is found within the lower (multiday) frequencies, with slight peaks at periods of ≈64 and ≈128 hours (≈3 and ≈5 days respectively) for both the zonal and meridional components. This low-frequency forcing of winds excites inertial oscillations of sea ice, indicated by buoy U1's peak within the inertial frequency range (see Figure 3.9).

In order to examine the periodicities of the ice drift velocity, in both the time and frequency domain, a wavelet analysis was done (see Section 2.4.7). Figure 3.10 shows the wavelet power spectrum (left) and the wavelet spectrum (right) of both the zonal and meridional drift components of buoy U1 until the 20th July. The other buoys display similar results and are found in Appendix A (Figures G-J). The wavelet power spectrum indicates the presence of two main cycles (energy components) within sea-ice drift. During the passage of the first cyclone, momentum is transferred from the strong winds to the sea ice, where the drift of the ice floes respond at both the synoptic and inertial frequencies. Sea ice captures the increase in power within the inertial frequency range which is not found within the wind spectrum. The wavelet power spectrum highlights this feature of sea ice.

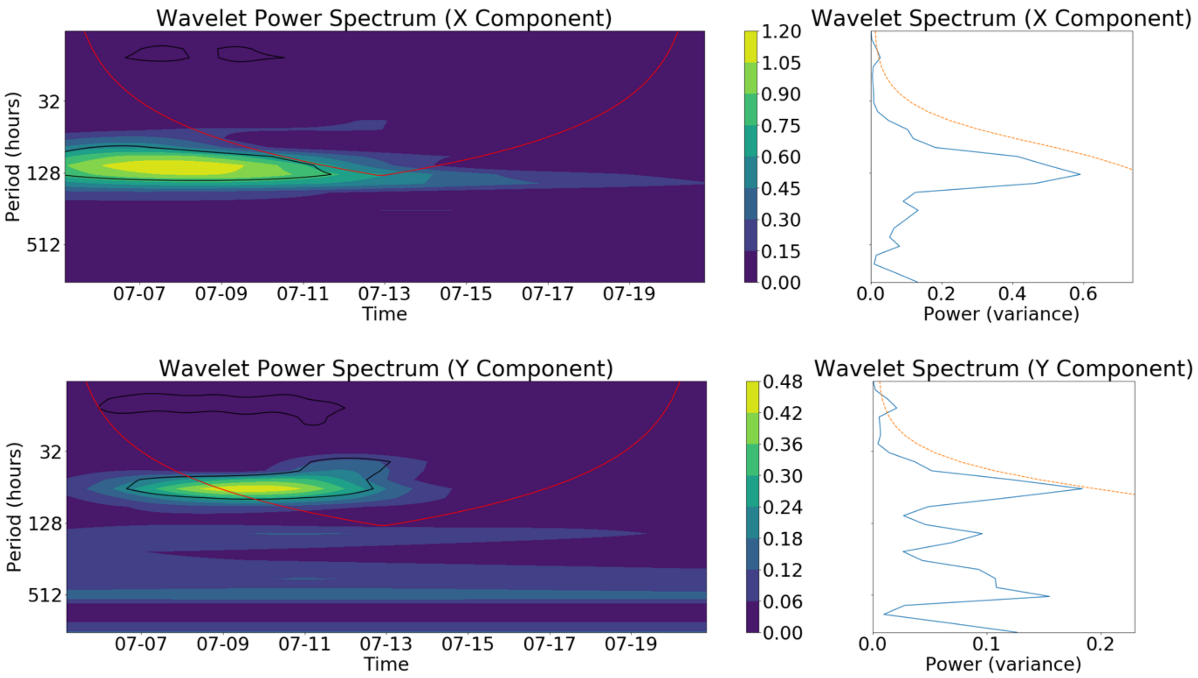

Figure 3.10: The Wavelet Power Spectrum (left) and the Wavelet Spectrum (right) of buoy U1. The red line indicates the cone of influence, the black contours (left two figures) and orange dashed line (right two figures) indicate the 95% significance level.

The wavelet power spectrum (Figure 3.10) shows that both of the ice drift components display statistically significant power between the 5th and 11th July for the zonal component, at the 128-hour period, and between and the 7th and 13th July for the meridional component, at 64 hours. This two-day lag at the synoptic frequencies, between the zonal and meridional components, would be due to the cyclone initially pushing the buoys zonally before pushing the buoys meridionally. Majority of the power within sea-ice drift is found at the synoptic frequencies, showing the direct transfer of momentum from the low-frequency wind forcing to the sea ice. However, a longer time series is needed to fully show the synoptic energy component as most of the power, particularly for the zonal component, lies outside of the COI. A further analysis is conducted in Chapter 4, where buoy U1 drifted for four months, where the edge effects are reduced.

In addition to the synoptic response of sea ice, the momentum transfer from winds at the lower frequencies excites an inertial response which occupies a well-defined frequency band (see Figure 3.9), and is due to the embedding of the ice cover within the upper ocean layer (Heil et al., 2009). Both the *u* and *v* drift components display statistically significant power within the inertial response period of ≈13.5 hours, between the 6th and 12th July (Figure 3.10). This inertial response is found within the COI for both components, and is therefore void of any edge effects.

Synchronous with the ocean, sea ice (McPhee, 1978) provides a medium that successfully allows the transfer of energy from the lower frequencies (wind forcing) to semi-diurnal frequencies (Heil et al., 2009). However, as seen in Figure 3.10, these two frequencies are not directly connected to one another and do not show the transfer of power from the lower frequencies to the inertial frequencies. Unlike tidal forcing which is distinctly linked to high-frequency oceanic processes, inertial oscillations of sea ice have no direct high-frequency equivalent in the atmospheric and oceanic spectra (Heil et al., 2009). Here, a cascade of energy from multiday frequencies is needed to produce both the synoptic and inertial frequency responses in ice drift (Figure 3.9). This energy cascade develops from non-linear processes in ice motion, which is driven by synoptic-scale changes in atmospheric forcing (McPhee, 1978).

While the first cyclone was the most intense, the greatest amount of power at the synoptic frequencies only occurred after the passage of the second cyclone, which had winds reaching 15 m s^{-1}, the largest ice drift velocity for all buoys and a high wind factor. Additionally, the dates when the inertial response was significant were found to coincide with the passage of the second and third cyclones, and when the meander coefficient increased. The meander coefficient is associated with the inertial oscillations because if there are inertial oscillations, there will be a deviation from a straight trajectory path. However, as this is only for a 15-day analysis it will be further examined in Section 4.6, when buoy U1 drifted for four months.

During this 15-day analysis, the ice floes were closer to the ice edge, and predisposed to strong winds by wave activity. Therefore, they are expected to follow and oscillate in a similar way to an ocean fluid parcel with strong inertial oscillations (Gimbert et al., 2012). The last three cyclones had winds only reaching 10 m s^{-1} and therefore there was a reduced transfer of momentum for exciting inertial oscillations. Consequently, with the reduction of wind forcing, the power at the synoptic and sub-daily frequencies dissipated within a few days after the third cyclone. The inertial oscillations therefore decayed due to kinetic energy dissipation within the Ekman layer, internal ice stresses and/or friction between the ice bottom and ocean surface. The elliptical loops of the buoys therefore disappeared before the passage of the next cyclone over the ice edge, which would have excited new inertial oscillations.

4. RESULTS: SYNOPTIC INFLUENCES ON ICE DRIFT OVER THE SEASONAL SCALE

This chapter presents a comprehensive analysis of the four-month drift of buoy U1 from the South Atlantic sector to the Indian Ocean sector of the Southern Ocean. This period encompasses the advance and retreat phases of the seasonal sea ice in these regions. The results of the analyses will be discussed concurrently.

4.1. The influence of seasonality on sea-ice drift

Buoy U1 remarkably transmitted information on sea-ice drift for over four months until the signal was lost at 61.5°S and 55.0°E on the 1st December 2017, presumably due to ice melting. The other four buoys stopped transmitting information in July and August, presumably due to buoy malfunction as the SIE was still expanding. Over this approximately four-month drift of buoy U1, it travelled a net distance of ≈1336 km from the South Atlantic sector to the Indian Ocean sector of the Southern Ocean, with minimal variation in latitude ($<2^{o}$) (see Figure 4.1). Throughout this period from July to December, the SIE underwent a seasonal change from austral winter to spring. However, unlike the Arctic which has a symmetric seasonal cycle in the waxing and waning of sea ice, the Antarctic has an asymmetric seasonal cycle characterised by a slow sea-ice advance in the austral winter months (March to September), and a rapid retreat during the austral summer months (November to February) (Eayrs et al., 2019). This rapid retreat can be seen during the last period of buoy U1's trajectory in Figure 4.2, where the ice extent during November reduced by over 100 km in only fifteen days.

The tracks of the synoptic cyclones define the position of the ACT (Section 1.3), which varies between regions and seasons. It is strongest and usually situated farthest south during austral spring and autumn and shifts north during austral summer and winter (Irving et al., 2010; Schlosser et al., 2011). This means that the ACT may be situated south of the ice edge during some months (Schlosser et al., 2011), where the synoptic cyclones travelling within the trough have a higher influence on the formation and distribution of sea ice.

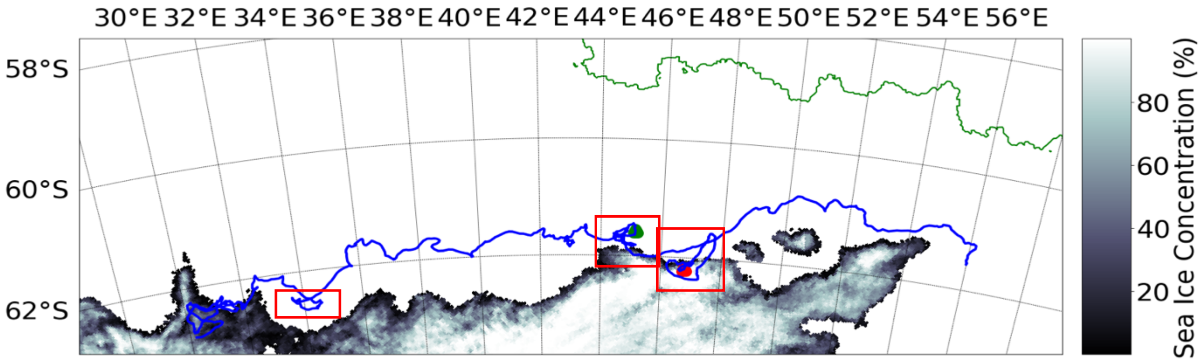

Figure 4.1: The full trajectory of buoy U1 (blue line) from the 5th July to the 1st December. The shadings show the AMSR2 SIC with values between 0%-100% on the 1st December. The green circle denotes the end of the advance season on the 30th September. The red circle denotes the beginning of the melt season on the 1st November. The green line indicates the ice edge at 0% ice concentration for the 30th September, the maximum northward extent of sea ice. The three red boxes indicate the three loops within buoy U1's trajectory, excluding the first loop analysed in Chapter 3.

Figures A-C in Appendix B show the air temperatures and pressure fields when ten ice-landing cyclones between August and October were closest to buoy U1's position, as it drifted eastwards within the MIZ. The Antarctic sea ice is not bounded by land, and is free to vary in response to these polar cyclones as well as oceanic influences (Eayrs et al., 2019). Twice a year, with the shifting of the ACT, the changes in the position and the intensity of these zonal winds work either with or against the continuously evolving ice edge to slow down the autumn advance and hasten the spring retreat (Eayrs et al., 2019), through increased wave activity and the advection of moisture from the lower latitudes (see Section 3.1). This is seen in Figure 4.1 where buoy U1 spent most of its time drifting during the sea-ice advance until the point of the green circle, which indicates the location buoy U1 on the last day of September, approximately the time of the Antarctic SIE maximum. On the other hand, buoy U1 drifted much less during the spring melt season, when the zonal winds along with the change in the surface radiative balance worked to hasten the spring retreat. This is indicated by the shorter trajectory from the red circle – denoting the location of buoy U1 on the 1st November, where the spring retreat begins in November (Eayrs et al., 2019) – to the end of buoy U1's trajectory at 56^{o}E (Figure 4.1). Therefore, the analysis of buoy U1 may help to investigate the role atmospheric forcing have on the melting.

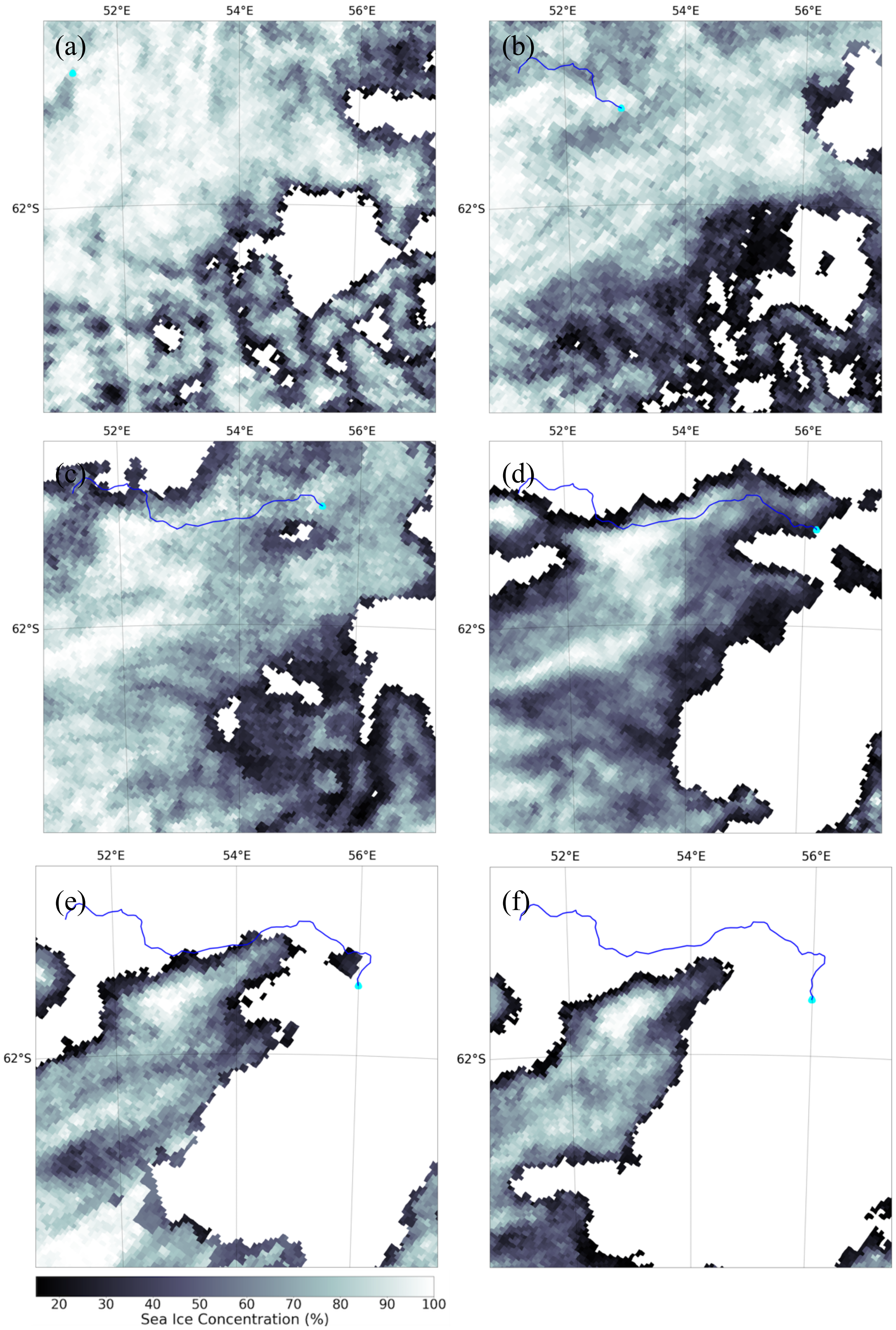

Figure 4.2: The drift trajectory of buoy U1 for the last fifteen days of its complete drift period: (a) at 12:00 on 16th of November; (b) at 12:00 on 21st of November; (c) at 12:00 on 26th of November; (d) at 12:00 on 29th of November; (e) at 12:00 on 30th of November (f) at 12:00 on 1st of December. The blue line indicates buoy U1, with the light-blue circle denoting the position of the buoy for the corresponding day. The shadings show the AMSR2 sea-ice concentration with values between 0%-100% on the corresponding day of each plot.

4.1.1. Mismatch in satellite-derived ice conditions during melting

As buoy U1 drifted until the 1st December, it experienced the beginning of the summer-time sea-ice melt, where ice floes would have become smaller, thinner and often covered by surface water. However, in Figure 4.2 it can be seen that according to the high-resolution AMSR2 sea-ice concentration, buoy U1 exited the MIZ prior to the last day of transmission (1st December), apparently on the 29th November. The two-day discrepancy between buoy U1 and the AMSR2 ice concentration is likely due to an underestimation of ice concentration by the satellite product. This is also found in the lower resolution AMSR2 product (Figure 4.3) however, the SIC from the coarser SSMIS sensor with a spatial resolution of 25 km shows that buoy U1 was in the ice until the 1st December.

The two-day inconsistency found in the AMSR2 estimates could be due to either (1) the small size of the floes, (2) the buoy being situated on brash ice and/or (3) surface melting or flooding by wave action. These may cause the sea ice to be interpreted by the high resolution ASI algorithms as less than 15% SIC, and there are inherent uncertainties with ice concentrations lower than 15%. Additionally, there are many corrections being made on the AMSR2 sensors, which may likely remove the presence of ice. Liu et al. (2020) reported that the AMSR2 sensor identified areas near the Arctic ice edge as water while NOAA's Interactive Multisensor Snow and Ice Mapping System (IMS), based on the human analysis of several near-real-time datasets, identified the areas as being covered by sea ice. This discrepancy of the AMSR2 (at both resolutions) can be attributed to their limited capability to detect thin ice near the ice edge, especially during the melt season (Liu et al., 2020).

Figure 4.2(e) however, shows an additional cluster of sea ice at ≈56^{o}E and therefore buoy U1 could have been carried away from the MIZ by underlying currents on a surrounding band of small ice floes or brash ice. Additionally, Trident buoys weigh ≈25 kg (see Section 2.1), and therefore sink when ice floes melt and can no longer support the weight of the buoys. Therefore, as buoy U1 transmitted information on sea-ice drift until the 1st December, it ensures that it was on the floes until that date.

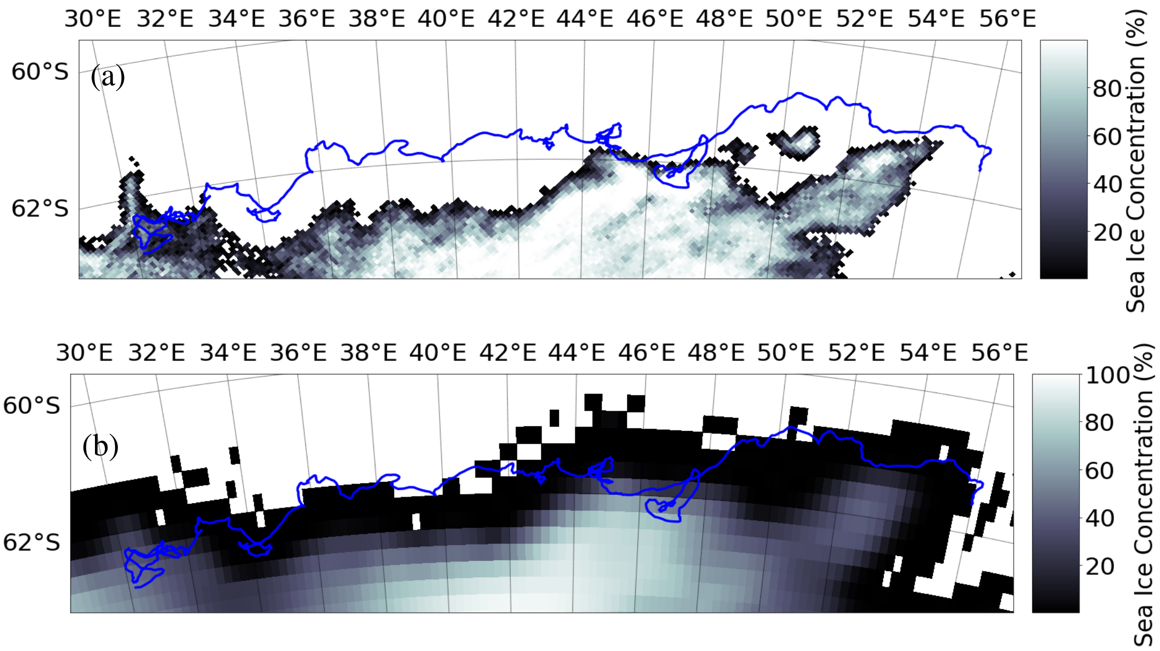

Figure 4.3: The full trajectory of buoy U1 (blue line) from the 5th July 2017 to the 1st December 2017 with (a) the shadings showing the AMSR2 6.25 km spatial resolution SIC and (b) the shadings showing the SSMIS 25 km spatial resolution SIC. The ice concentration values for both satellite products are between 0%-100% for the 1st December 2017.”

4.2. The role of the ice edge on buoy U1’s trajectory

Figure 4.4 shows that the distance of buoy U1 from the ice edge fluctuates as the ice edge is rearranged by the ice-landing cyclones, discussed in Section 4.1. The red rectangular boxes indicate the periods of frequent cyclone activity found using the methods detailed in Section 2.4.4, which correlate with the three large loops that were identified as being the most prominent in the buoy’s trajectory and will be further discussed in Section 4.3. The green rectangular box denotes the five cyclones previously discussed in Chapter 3. It can be seen that the minimum distances of buoy U1 from the ice edge correlates with these periods of frequent cyclone activity. This could be because of the propagation of waves deep into the MIZ, which breaks up and allows the sea ice to become more susceptible to the regular passage of cyclones, which then leads to the ice floes being pushed downwind to produce a relatively narrow ice edge region (Heorton et al., 2014). This results in the compression of the unconsolidated pancake ice field, and the southwards movement of the ice edge, which is then followed by the relaxation and the northwards movement of the ice edge during periods between storms, when southerly winds are prevalent.

The varying distance from the satellite-estimated ice edge alternates between larger during reduced storm activity and smaller during high storm activity. However, as discussed in Section 4.1.1, the AMSR2 passive microwaves sensors are limited in capability to detect thin and small ice floes within the ice edge region and therefore from November on (during summertime sea-ice melt), it is uncertain whether the estimate of the distance from the ice edge is accurate. Therefore, the same calculation was computed using the SSMIS ice concentrations from the 1st November until the last day of buoy U1's transmission (see Figure 4.5(b)), as it captured buoy U1 within the MIZ until the 1st December. The grey shaded areas in both Figure 4.4. and Figure 4.5. indicate the period (16th November to the 1st December) when the buoy was still active but outside the AMSR2 satellite-derived ice edge, as detailed in Figure 4.2.

Figure 4.5 shows a comparison between the AMSR2 and SSMIS ice edge calculations, from the 1st November to the 1st December. The SSMIS distance displayed a vastly different and often opposite outcome to the AMSR2 distance from the ice edge calculation. The biases between the AMSR2 sensors and the SSMIS sensor can be due to the differences in algorithm sensitivity to ice edge conditions and due to the spatial resolution of the sensors (Meier and Steward, 2019). Therefore, the SSMIS may have a better capability in detecting the ice edge region as it cannot resolve small ice clusters, but rather it smooths over large areas of ice cover.

The distance of the SSMIS distance initially decreased from ≈120 km on the 1st November to ≈5 km on the 11th November, while the AMSR2 distance shows the opposite. The distance between the buoy and the AMSR2 ice edge rather increased from ≈10 km on the 1st November to over 100 km on the 7th November. The SSMIS distance then displayed a general increase until the 20th November, whereas the AMSR2 distance showed a general decrease until the 20th November. The SSMIS distance then displayed one more peak on the 27th November, before decreasing as the buoy began to drift closer to the ice edge, ending at ≈10 km from the ice edge. The AMSR2 distance on the other hand displayed one much larger peak (at ≈80 km) on the 25th November, during which the SSMIS showed a distance minimum. The AMSR2 distance then decreased to ≈20 km on the 29th November. This decrease correlates with Figure 4.2(d), where it looks as though buoy U1 was leaving the MIZ. The distance then began to increase once again as buoy U1 presumably drifted on a band of brash ice or a cluster of small ice floes (see Figure 4.2(e)). On the 1st December, the AMSR2 sensor did not capture the likely presence of smaller ice floes, mentioned above in Section 4.1.1, and therefore the distance increased to ≈40 km in the open ocean.

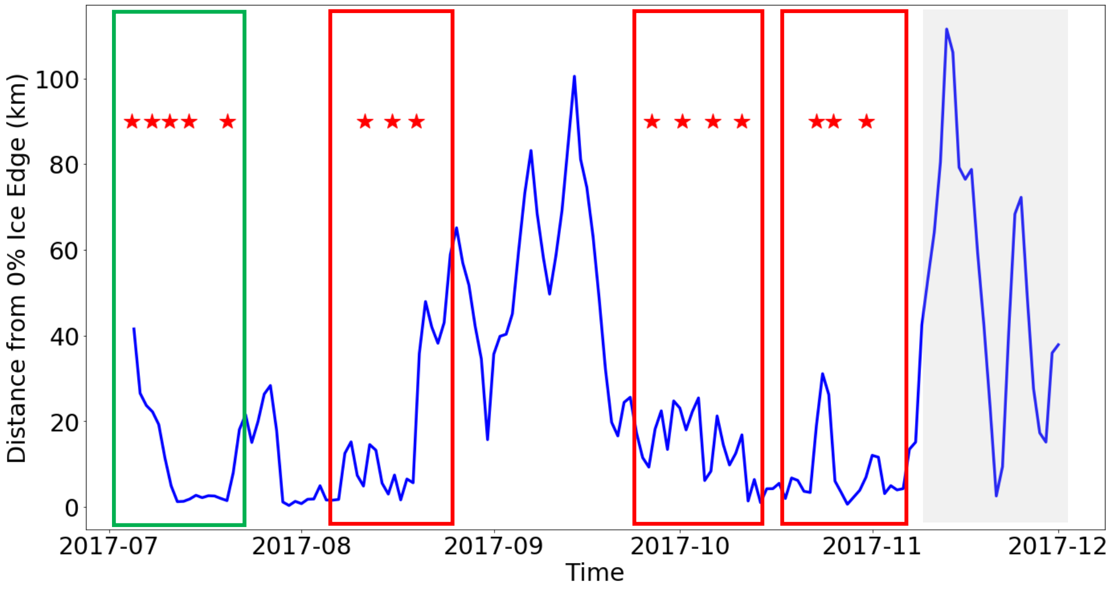

Figure 4.4: Distance between buoy U1 and the ice edge defined by AMSR2 (3.125 km) 0% sea-ice concentration. The red star symbols indicate the time when the storm cores were closest to the buoy's location. The green rectangular box denotes the five storms previously examined in Chapter 3. The red rectangular boxes denote the three sets of storms examined in Section 4.3. The grey shaded area denotes the end of buoy U1's drift when the AMSR2 was limited in detecting thin ice.

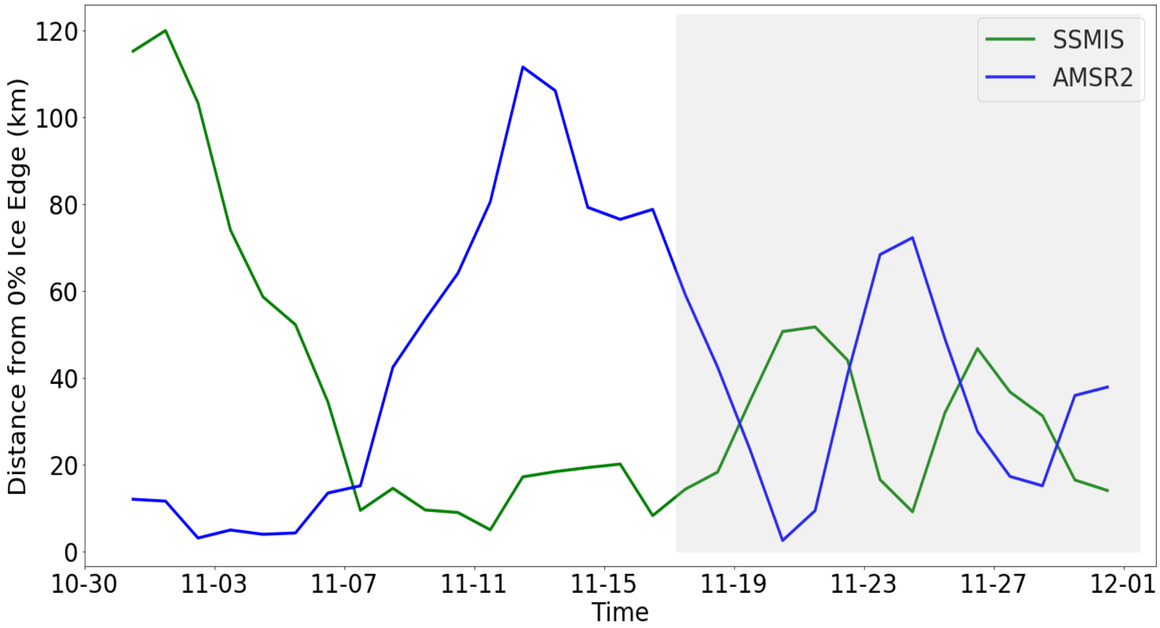

Figure 4.5: Distance between buoy U1 and the ice edge defined by (blue) the AMSR2 (3.125 km) 0% sea-ice concentration and (green) the SSMIS 0% sea-ice concentration for the 1st November to the 1st December. The shaded grey areas are comparable with the dates of the shaded area in Figure 4.4.

4.3. Polar cyclones and sea-ice meandering

The dates whereby buoy U1 was close to the ice edge (see Figure 4.4) not only coincided with periods of consecutive cyclones, but also with the largest elliptical loops of the buoy's trajectory (Figure 4.6). The left-hand-side column (a-e) of Figure 4.6 shows the three larger loops superimposed on the AMSR2 sea-ice concentration for the last day of each corresponding loop, where it can be seen that the buoy is very dynamic and mobile, even at high ice concentrations (> 80% SIC). The right-hand-side column (b-f) shows the buoy's trajectory with its daily position at 12:00 pm, and its position when each cyclone (see Figures A-C in Appendix B) was closest to it.

The first loop (Figure 4.6(a-b)) occurred between the 9th-20th August as a result of three polar cyclones (Figure A in Appendix B) travelling eastwards past buoy U1. The first two polar cyclones (9th-12th August and 15th-17th August) developed just north of the ice edge and progressed south-eastwards with a deepening core until complete lysis along the Antarctic coastline for the first cyclone, and to the east of buoy U1 for the second cyclone. The third cyclone developed to the west of buoy U1 along the ice edge on the 18th August, and travelled south-eastwards passing over the position of buoy U1 until it disappeared on the 20th August along the Antarctic coastline, south-east of the buoy.

The next large loop along buoy U1's trajectory occurred between the 26th September-12th October at approximately 10° east of the previous loop. This relatively tight-looped meander (see Figure 4.6(c)) was a result of four polar cyclones (see Figure B in Appendix B) travelling eastwards across the MIZ. The first cyclone was short-lived as it developed along the ice edge on the 26th September, and travelled south-eastwards until complete lysis on the 27th September, at the Antarctic coastline. The second cyclone developed north of the ice edge on the 30th September and moved eastwards until it vanished on the 2nd October to the north-east of buoy U1. The third cyclone developed along the ice edge on the 4th October, where it initially persisted in the same location for a day before travelling eastwards until lysis on the 7th October. The forth cyclone developed along the ice edge on the 11th October, where it travelled south-eastwards until it disappeared on the 12th October near the Antarctic coastline, where the lysis occurs more often (see Section 1.4 in the Introduction).

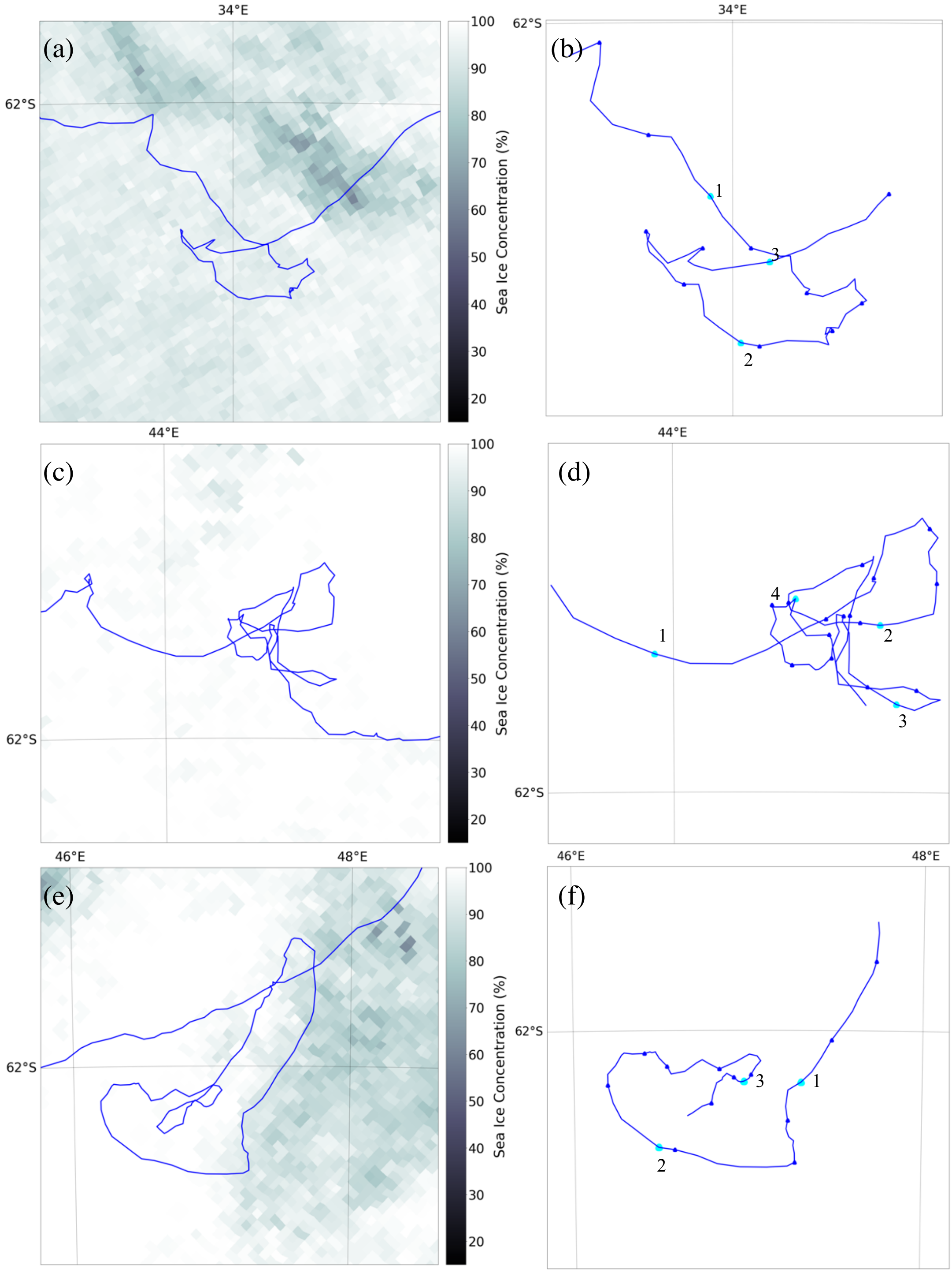

Figure 4.6: Three case studies of large elliptical loops in the drift trajectory of buoy U1 for the (a-b) 9th-20th August; (c-d) 26th September-12th October; (e-f) 21st-31st October. The blue line denotes buoy U1's trajectory. The shadings show the AMSR2 sea-ice concentration with values between 0%-100% on the last day for each corresponding meander. The dark-blue points on the right-hand-side denote the position of buoy U1 at 12:00 pm every day. The light-blue points on the right-hand-side denote when each cyclone was closest to buoy U1. The numbers denote the chronology of the storms.

The final large loop occurring along buoy U1's trajectory followed soon after the second elliptical loop from the 21st-31st October (Figure 4.6(e-f)). This loop was a result of three ice-landing cyclones (see Figure C in Appendix B) passing over buoy U1. The first cyclone (21st-23rd October) developed just north-west of the buoy and progressed south-eastwards until it disappeared south-east of the buoy, near the continent. The second cyclone impacted the buoy the following day on the 24th October just north of the ice edge and travelled south-eastwards until lysis to the east of the buoy on the 27th October. The final cyclone was short lived (30th-31st October) however, it developed west of the buoy, south of the ice edge, and then travelled eastwards over the buoy, where it then vanished.

All of the cyclones described above travelled across the MIZ, impacting buoy U1's drift differently. On the 9th August, buoy U1 began to travel in the first large cyclonic loop (Figure 4.6(b)). The buoy initially drifted south-east during the passage of the first cyclone with wind speeds of ≈ 15 m s^{-1} (Table 4.1). The second cyclone also brought wind speeds of ≈ 15 m s^{-1} causing buoy U1 to drift north-westerly before switching north-easterly under the influence of the third cyclone, with wind speeds of ≈ 21 m s^{-1}. This high wind speed, dominating buoy U1's drift, can be seen by the large distances between the consecutive daily positions of the buoy (dark-blue points), especially during the third cyclone.

In the second loop (Figure 4.6(c-d)), buoy U1 drifted in a much tighter loop, several times, before once again travelling in a straight-line path. The first cyclone, with maximum wind speeds reaching ≈ 20 m s^{-1} (Table 4.1), initially caused the buoy to travel rapidly south-east before switching north-east. During this period of high wind speeds, buoy U1 once again displayed large distances between its 12:00pm daily positions in Figure 4.6(d). The second cyclone, with wind speeds of ≈ 13 m s^{-1} (Table 4.1), resulted in several changes in the buoy's drift direction; a southerly, a westerly, and then finally a north-easterly drift. During the third and fourth cyclones with wind speeds of ≈ 20 m s^{-1} and ≈ 14 m s^{-1} respectively (see Table 4.1), buoy U1 meandered in two small anti-clockwise loops before drifting south-easterly.

The final loop of buoy U1 in Figure 4.6(e-f), showcased a much more elongated trajectory than the previous two loops. The buoy initially travelled south-westerly under the influence of the first cyclone with wind speeds of ≈ 16 m s^{-1} (Table 4.1) before switching to a southerly direction. The second cyclone brought wind speeds of ≈ 17 m s^{-1}, causing buoy U1's to drift north-westerly. The third cyclone, passed right over the buoy with wind speeds of ≈ 10 m s^{-1}

causing it to drift south-west before drifting north-easterly in a more straight-line path. This caused the buoy to showcase an “8-shaped” drift pattern (Figure 4.6(e)).

Pancake ice has a dynamical and qualitative response to these frequent and intense cyclone events which impact the Antarctic MIZ (Alberello et al., 2020). With the passage of each cyclone and their varying winds, the buoy’s trajectory was divided by sharp turns and loops. This response is attributed to minimal/absent internal stresses in pancake ice (Leppäranata et al., 2011), which has been confirmed in the analysis of the first 15 days of the deployment presented in Chapter 3.

Table 4.1: Features of the cyclones which occurred during the loops as simulated by ERA5

Cyclone	Dates	Maximum Wind Speeds	Core Air Pressure
Loop 1			
Cyclone 1	9-12th August	15 m s^{-1}	940 hPa
Cyclone 2	15-17th August	15 m s^{-1}	955 hPa
Cyclone 3	18-20th August	21 m s^{-1}	960 hPa
Loop 2			
Cyclone 1	26-27th September	20 m s^{-1}	950 hPa
Cyclone 2	30th September-2nd October	13 m s^{-1}	960 hPa
Cyclone 3	4-7th October	20 m s^{-1}	940 hPa
Cyclone 4	11-12th October	14 m s^{-1}	960 hPa
Loop 3			
Cyclone 1	21-23rd October	16 m s^{-1}	960 hPa
Cyclone 2	24-27th October	17 m s^{-1}	945 hPa
Cyclone 3	30-31st October	10 m s^{-1}	970 hPa

4.4. Quantitative measures of buoy drift

The dynamic response of buoy U1 to the passage of the intense and frequent cyclonic systems is further examined by analysing the velocity and meandering coefficient of the buoy's drift as done for the cluster of buoys in Chapter 3. Figure 4.7 shows the zonal and meridional velocities of buoy U1 for the four-month period, where it can be seen that the buoy responded qualitatively to both the speed and direction of the overlying winds. The zonal velocity of the buoy is slightly more variable, with a standard deviation of 0.21, while the meridional velocity has a standard deviation of 0.18. However, the buoy's velocity components varied according to the wind. During the periods of cyclone activity, denoted by the four rectangles, the ice drift velocity notably increased while additionally following the direction of the wind's velocity components. However, in mid-September there is one increase in the wind and ice drift speeds, particularly within the zonal component, that does not correspond to any storm. Therefore, it is important to quantify the drift response objectively, which will be done in next section. The overall drift of buoy U1 shows a high correlation to wind, which indicates the persistence of free drift conditions identified after the buoy deployment throughout the trajectory of buoy U1.

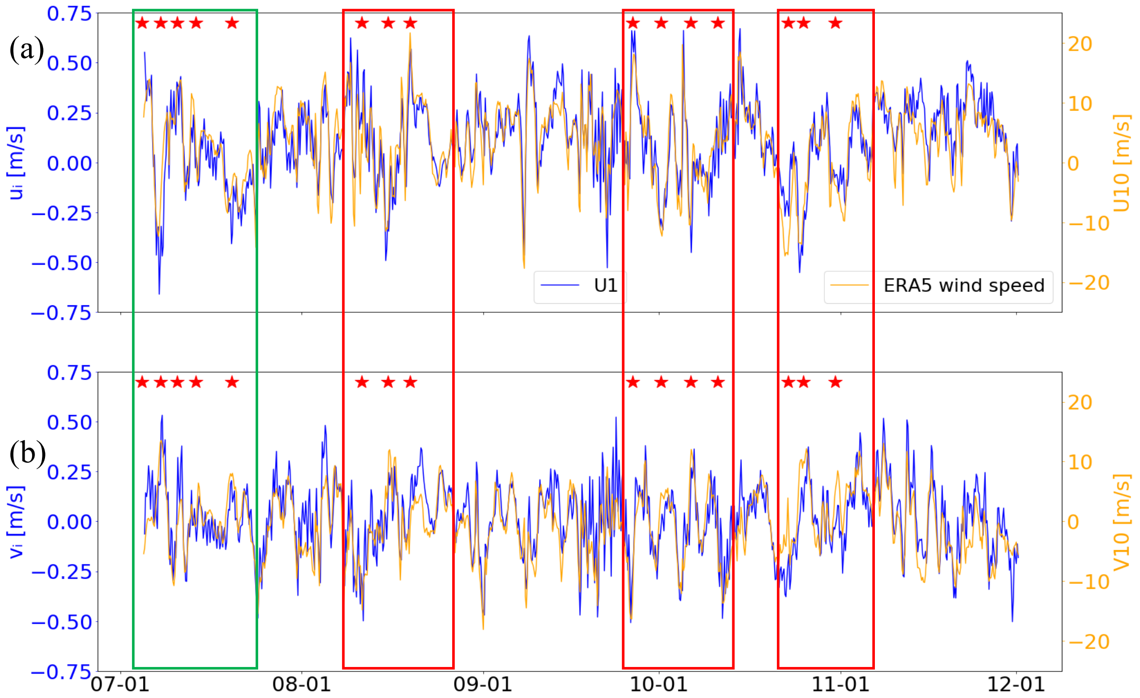

Figure 4.7: (a) The zonal velocity of buoy U1 (on the left axis) and the zonal wind velocity (on the right), and (b) the meridional velocity of buoy U1 (on the left axis) and the meridional wind velocity (on the right). The red star symbols indicate the time when the storm cores were closest to the buoy location. The green rectangular box denotes the five storms previously examined in Chapter 3. The three red rectangular boxes denote the three sets of storms examined in Section 4.3.

I now turn my attention to the meander coefficient. As buoy U1 had a larger zonal velocity than meridional velocity (Figure 4.7), it allowed the buoy to travel a total trajectory distance of ≈3322 km with a net transition distance of ≈1336 km, from the Atlantic Ocean sector to the Indian Ocean sector of the SO. This conformity of the eastwards drift of buoy U1 is due to the steering influence of the ACC, and with the impact of cyclones it led to an overall meander coefficient of 2.42. This is lower than the meander coefficient of buoy U1 during the initial 15-day analysis (4.86), indicating that buoy U1 for its full duration had a more straight-line trajectory than at the early stages after deployment.

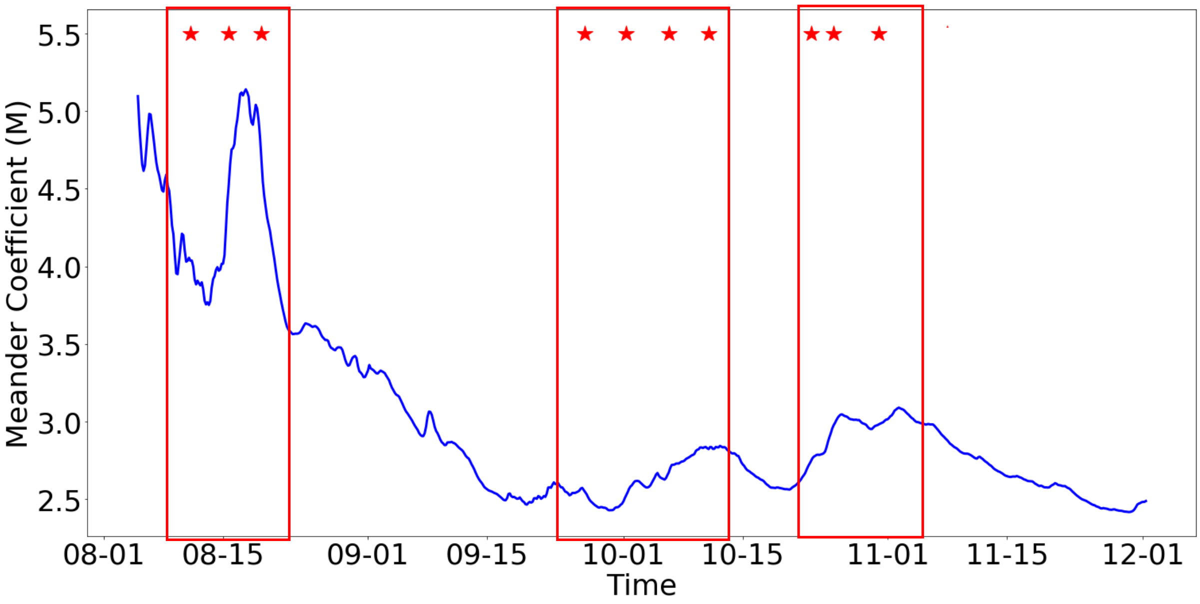

Figure 4.8: Time series of the meander coefficient for buoy U1, from the 5th August-1st December. The red star symbols indicate the time when the storm cores were closest to the buoy location. The three red rectangular boxes denote the three sets of storms examined in Section 4.3.

Figure 4.8 shows the meander coefficient time series for buoy U1 from the 5th August, just before the first elliptical loop (Figure 4.6(a-b)) until the 1st December, which was the last day of transmission. It can be seen that similar to the initial 15-day analysis, the meander coefficient increased during the periods of frequent cyclone activity, indicated by the red rectangular boxes, and decreased during periods of quiescence. This phenomenon is linked to the initiation of inertial oscillations of sea ice by energetic winds, which will be discussed later in Section 4.6. Figure 4.8 shows no increase in the meandering of buoy U1 during the September period when there was an apparent increase in drift speed that was not associated with a cyclone. This is indicative that high drift speeds may also occur without the vicinity of a cyclone core, and this drift will occur on a straight line, with minimal inertial response (see Section 4.6). At the end of the four-month drift the meander coefficient was much smaller than during three periods of frequent cyclone activity. This is because at the end of the four months there was a reduction in cyclone activity as a result of the northwards shift of the ACT in the summer months (see Section 4.1), allowing for an increased influence of the mean ocean circulation and a more straight-line path. Similarly, Heil et al. (2009), using a 37-day buoy array, derived low meander coefficients (1.3-2.7) for the East Antarctic near the Antarctic coastline, and attributed this more straight-line ice drift to be rather part of a single large-scale forcing system – the Antarctic coastal current.

4.5. Wind response

Table 4.2 shows that the mean wind factor of buoy U1 decreased only slightly from 2.86% for the 15-day analysis of buoy U1 (Section 3.3) to 2.73% for the full drift. This slight reduction could be due to the greater influence of underlying currents during the longer drift period although it cannot be confirmed given the available measurements. Nevertheless, the mean wind factor remained high with a small mean turning angle of -19.83°, indicating a continued high wind response of buoy U1.

Figure 4.9 shows the relationship between buoy U1 and the wind vectors, obtained from ERA5 (see Section 2.3) for the four-month period. The ice drift speeds have been multiplied by 33 as done in Chapter 3, so that the 1:1 line represents an ice drift of 3% of the wind speed. The measured ice drift speeds are distributed quite evenly around this line, with a coefficient of determination of $R^2 = 0.60$. This did not change much from the initial 15-day analysis of buoy U1 (Table 4.2), demonstrating a sustained strong relationship between wind speed and ice drift speed. In terms of the ice drift direction and wind direction in Figure 4.9, the majority of points are closer to the 1:1 line with the bulk of them sitting just below it, at the lower portion of the -19.83° turning angle line. However, like the 15-day analysis of buoy U1 (Figure 3.8), some of the points are found at the top-left and bottom-right corners, leading to a R^2 value of only 0.40 between the wind direction and ice drift direction. These more remote points would have occurred during periods of quiescence, similar to that of the 15-day analysis, when the wind stresses were small and when the turning angle range was the largest.

Table 4.2: Principal Characteristics of the Drift Dynamics of Buoy U1

Buoy	Wind Factor (%)	Turning Angle θ (°)	Linear Coefficient of Determination (R^2)		Vector Coefficient of Determination (R_v^2)
			DIR	SPEED	
U1 (15 days)	2.86	-24.02	0.39	0.67	0.74
U1 (4 months)	2.73	-19.83	0.40	0.60	0.76

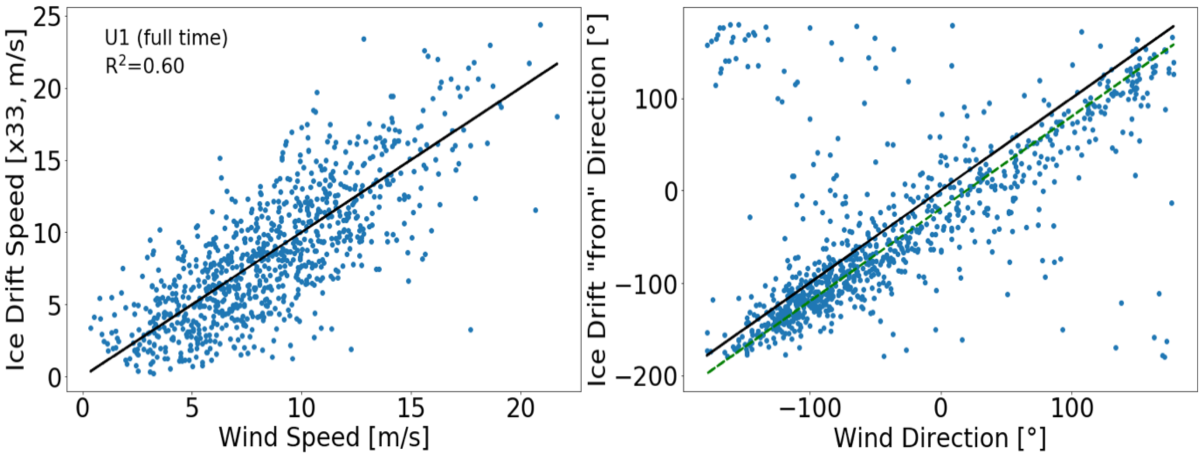

Figure 4.9: Scatterplots (left) of ice drift speed as a function of wind speed and (right) of ice drift direction as a function of wind direction of buoy U1. The black line is the 1:1 line. The green line is the turning angle at -19.83°.

The vector coefficient of determination (last column in Table 4.2) between buoy U1 and the wind vectors remained high with a $R_v^2 = 0.74$ for the initial analysis in Section 3.3 and a $R_v^2 = 0.76$ for the remainder of the trajectory. Additionally, the vector R_v^2 remained higher than the linear R^2 for the entire drift of buoy U1, indicating the that the relationship between ice drift and wind direction continued to be significant. Table 4.2 overall confirms the good correlation between the buoy's drift and the reanalysed wind, extending beyond the first 15-day period when the reanalyses were validated with in situ measurements. This demonstrates that wind continued to have a great physical control on the ice floe trajectory, even in regions where the eastward-flowing ACC is expected to become a dominant driver of the ice drift.

4.6. Spectral Analysis of buoy U1's drift

Figure 4.10 shows the power spectral density (PSD), detailed in Section 2.4.6, for the four-month drift of buoy U1. The wind velocity presents a classical, continuous energy cascade from the lower (multi-day) frequencies toward high (sub-daily) frequencies. The ice drift velocity is also subject to an energy cascade but indicates a clear energy peak at 13.47 hours. This energy peak is found within the theoretical range of 13.72-13.47 hours at 61°S-62°S, as shown in the earlier analysis in Section 3.4. These inertial oscillations have thus continued to be a prominent feature of buoy U1 for four months, as it drifted within the MIZ from the South Atlantic sector to the Indian Ocean sector of the Southern Ocean.

The majority of the power within the *u* and *v* components of wind is found at the lower frequencies, with slight peaks at 114 hours (≈5 days) for the zonal component and 93 hours (≈4 days) for the meridional component. This would be due to the passage of polar cyclones in the Southern Ocean which occurs on time scales of approximately five days (Thorndike, 1986), during which they directly transfer momentum from their strong winds to the sea ice. Heil et al. (2009) suggested that the multiday-frequency forcing of winds leads to the multi-day frequency of sea ice and these results confirm this as the ice drift PSD, although with less power, follows the energy cascade of the wind however, with a strong inertial signature.

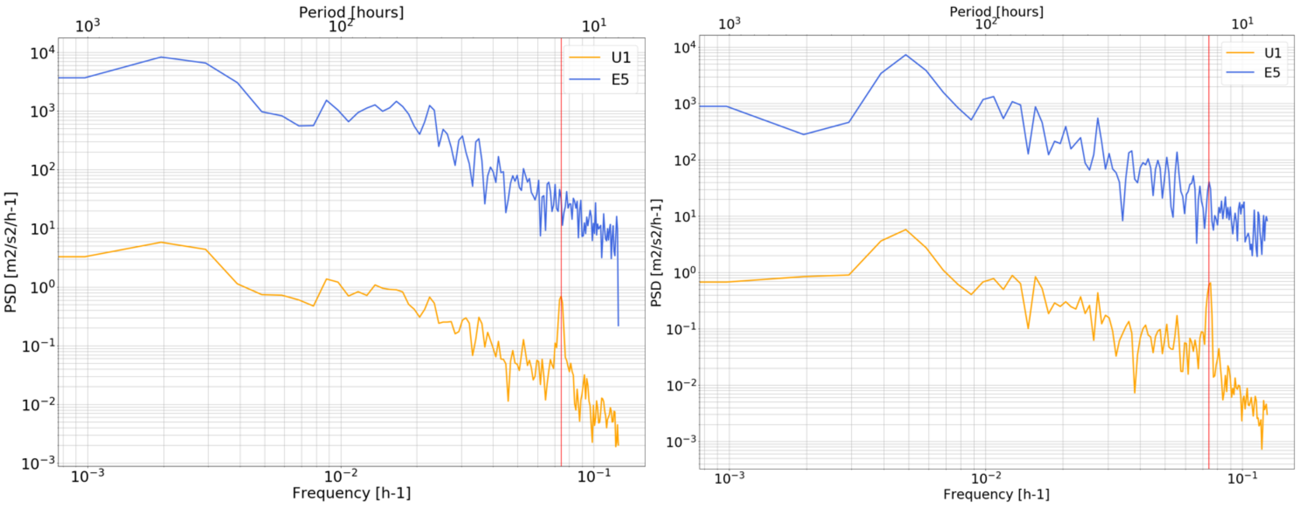

Figure 4.10: Power Spectral Density corresponding to the (left) zonal component of ice drift velocity and the (right) meridional component of ice drift velocity of buoy U1 for four months. The orange line indicates buoy U1 and the blue line indicates the ERA5 winds. The vertical red line indicates the peak associated with inertial oscillations (13.47 hours).

The PSD provides information only within the frequency domain and therefore, similar to the earlier analysis in Section 3.4, a wavelet analysis (see Section 2.4.7) was done to view the periodicity of the ice drift velocity in both the time and frequency domain. However, the shorter analysis in Section 3.4 did not allow for the assessment of processes that had longer periods, given the limit in the cone of influence. Figure 4.11 therefore shows the wavelet power spectrum (left) and the wavelet spectrum (right) of both the zonal and meridional drift components of buoy U1 for its four-month drift. The wavelet power spectrum shows that the zonal and meridional components of buoy U1's drift have statistically significant power (within the COI) throughout the time series, at both the lower and inertial frequencies. However, these two frequencies still show no direct connection to one another. The wavelet power spectrum shows three large intensifications of power in the lower frequencies (≈128, ≈320 and ≈512 hours respectively) for the zonal component, with a lagged response in the meridional component. The three main maxima observed in the zonal component occurred between the 5th-20th July (the initial period analysed in Section 3.4 with the cluster of buoys), the ≈6th-26th August and ≈30th September-10 November. The second two date ranges correspond with the dates of the three large meanders shown in Figure 4.6 and discussed in Section 4.3.

The dates of the elliptical loops in Figure 4.6 appear to correspond with the dates of significant energy within the inertial range for buoy U1 (Figure 4.11). Similarly, Gimbert et al. (2012), who defined a parameter 'M' that quantitatively explained for the time-dependent magnitude of inertial oscillations, found that M increased during periods when elliptical loops were best observed. This is because the elliptical loops detected in sea-ice trajectories are due to the superposition of an advection velocity and a rotation velocity within the inertial range (Section 1.7). When the cyclones affected the region occupied by the buoy, they transferred momentum to the sea ice which excited inertial oscillations (Heil et al., 2009). This allowed the rotation velocity to become larger than the advection velocity which then formed the elliptical loops (Gimbert et al., 2012), as seen in Figure 4.6 and increased the meander coefficient (see Figure 4.8).

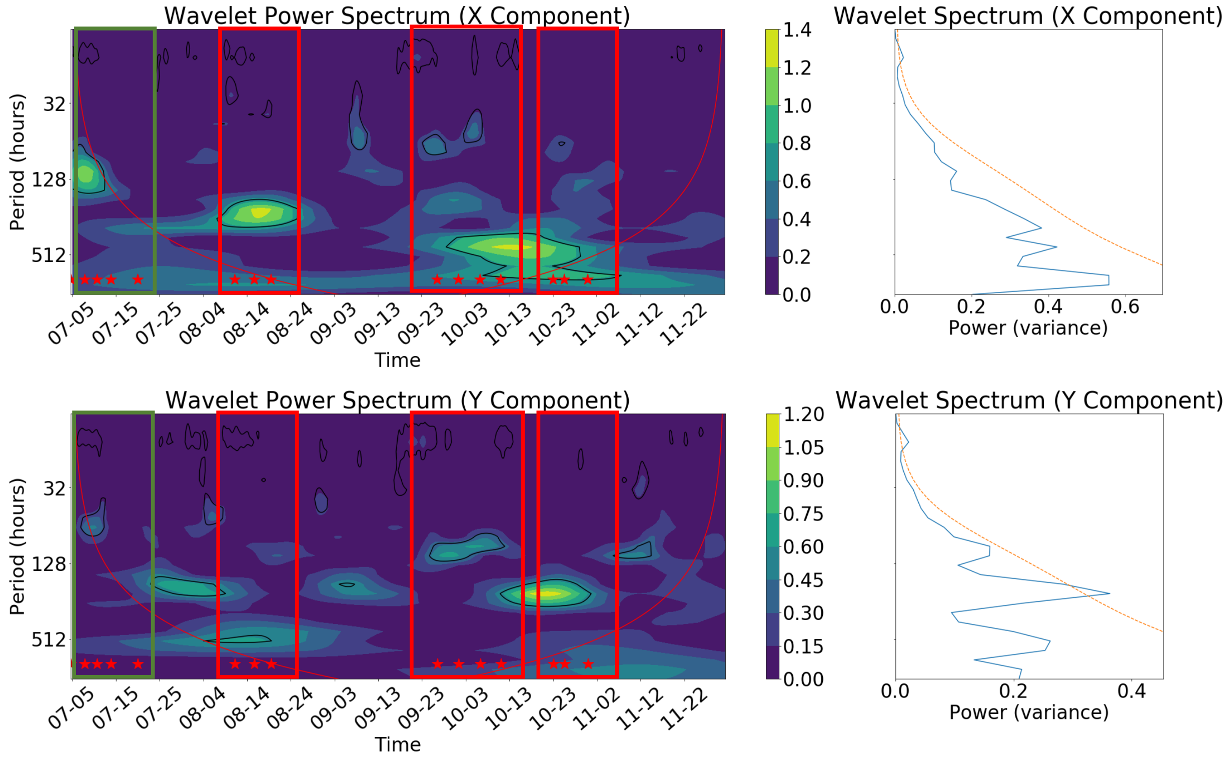

Figure 4.11: The Wavelet Power Spectrum (left) and the Wavelet Spectrum (right) of buoy U1 for its four-month drift. The red line indicates the cone of influence, the black contours (left two figures) and orange dashed line (right two figures) indicate the 95% significance level. The red star symbols indicate the time when the storm cores were closest to the buoy location. The green rectangular box denotes the five storms previously examined in Chapter 3. The three red rectangular boxes denote the three sets of storms examined in Section 4.3.

As buoy U1 drifted for approximately four months, the wavelet power spectrum in Figure 4.11 additionally captured a strong seasonal frequency (≈512 hours, > 20 days), particularly within the zonal component, which was not previously visible in the 15-day wavelet power spectrum of buoy U1 (Section 3.4). For the meridional component, the power peak is rather found between 128 and 512 hours, and while significant, it is less powerful than within the zonal component. Additionally, like the 15-day analysis the signal found at the inertial range, coincided with the dates of the lower-frequency power intensifications (Figure 4.11). This was done through a visual inspection however; a more objective analysis will be required in the future. This relationship between the two frequencies is because simultaneous with the ocean, strong winds initiate inertial oscillations of the sea ice (Lammert et al., 2009; Heil et al., 2009), and the ice drift changes to be dominated by high-frequency oscillations (Lammert et al., 2009), which lasts only for a few days (Gimbert et al., 2012).

This longer time series of buoy U1 in Figure 4.11 suggests that during the dates of the frequent passage of intense cyclone activity (discussed in Section 4.3), inertial oscillations were excited. However, as seen in the wavelet power spectrum (Figure 4.11), majority of the power within the velocity components of buoy U1 lies within the lower frequencies, whereas the inertial range holds much less power and is less prominent in the wavelet power spectrum. This led to the use of a high-pass Butterworth filter (detailed in Section 2.4.7.2) that was applied to buoy U1's velocity time series in order to filter out the lower frequencies which occurred throughout the trajectory (Figure 4.12). It passed all frequencies above 0.04 h^{-1} (the ≈daily frequency), allowing the sub-daily (inertial) frequencies to become more significant. This outcome can be seen in Figure 4.13, where the power at the inertial range for buoy U1 has a greater significance, that is now comparable with the filtered peak of power found at the lower multi-day frequencies.

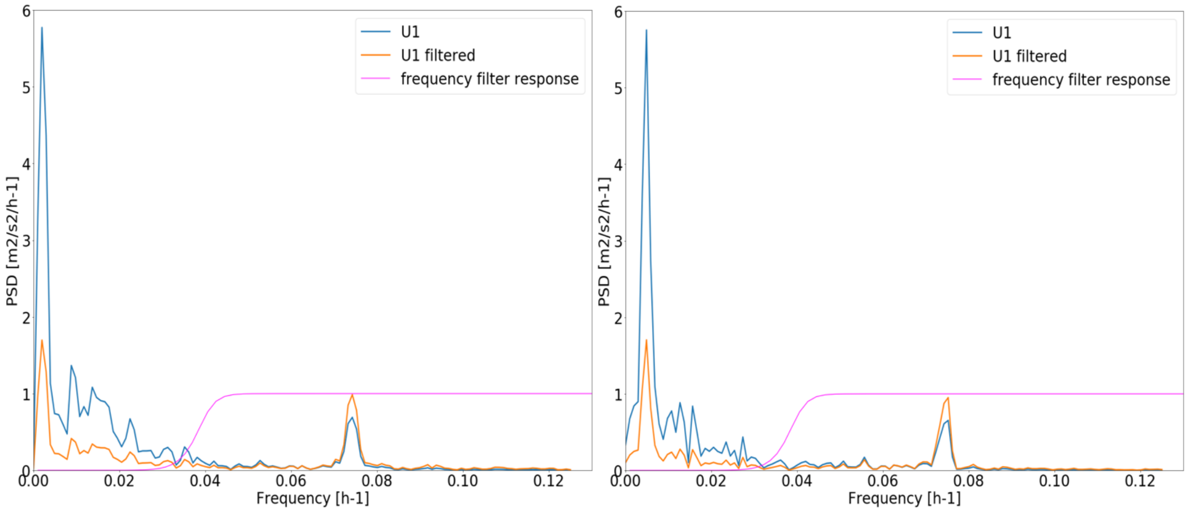

Figure 4.12: The Butterworth high-pass filter applied to filter out the lower frequencies of buoy U1's zonal (left) and meridional (right) velocity components. All frequencies below 0.04 (≈daily frequency) have been filtered out. The pink line is the filter response, passing all frequencies higher than 0.04. The blue line denotes the original spectrum. The orange line denotes the filtered spectrum.

With the lower frequencies being filtered out, the regular occurrence at which the inertial oscillations were initiated are more prominent in the wavelet power spectrum (Figure 4.13). There is much more significant power within both the zonal and meridional components at the inertial range, and the filter operations still allows to see the energy found at the lower frequencies. The strongest inertial oscillations coincided with the cyclones analysed in Section 4.3, especially the four cyclones (26th September-12th October) that caused the tightest elliptical loops in Figure 4.6(c-d). These four cyclones transferred great amounts of momentum from their energetic winds as seen by the large intensification of power at the synoptic frequencies of buoy U1 (≈128 to ≈512 hours, between 5 and 20 days), leading to high ice drift velocities (Figure 4.7) and an increased meander coefficient (Figure 4.8), which is closely linked to the significant inertial oscillations observed in the wavelet analysis at periods shorted than 16 hours (Figure 4.13).

These results suggest that the inertial oscillations of sea ice are quickly triggered by the passage of storms however, Alberello et al. (2020) attributed the presence of inertial oscillations to geostrophic currents (or sub-mesoscale eddies) in the ocean. This phenomenon was first proposed by Heil et al. (2009), in which sea ice provides a medium that allows the transfer of energy from wind forcing at the lower frequencies to the semi-diurnal frequencies. As already determined in Chapter 3, Figure 4.10 shows that an energy cascade from multi-day frequencies of wind velocity is needed to produce both the synoptic and inertial frequency responses in ice drift. However, as seen in Figure 4.13 this inertial response, although occurring more regularly than the synoptic frequencies, is shorter lived as inertial oscillations dissipate after a few days (Gimbert et al., 2012). This dissipation is likely due to kinetic energy dissipation within the Ekman layer, friction occurring between the bottom of ice foes and the ocean surface (Gimbert et al., 2012), and the internal stress of the ice floes, that cannot be measured with a single buoy. By means of the results of the meandering coefficient shown in Section 3.4, it is speculated that these forces dampen the rotation, which then leads to a more straight-line trajectory before new oscillations are excited. This is partly seen in Figure 4.1 where buoy U1 drifts with less meandering in between periods of large elliptical loops that are connected to the passage of the storms. The direct relationship between the occurrence of storms and the excitation of inertial oscillations is therefore suggested and confirmed by this present analysis, although a cluster of buoy would be required to better quantify the time evolution of ice deformation as for instance done in Itkin et al. (2017).

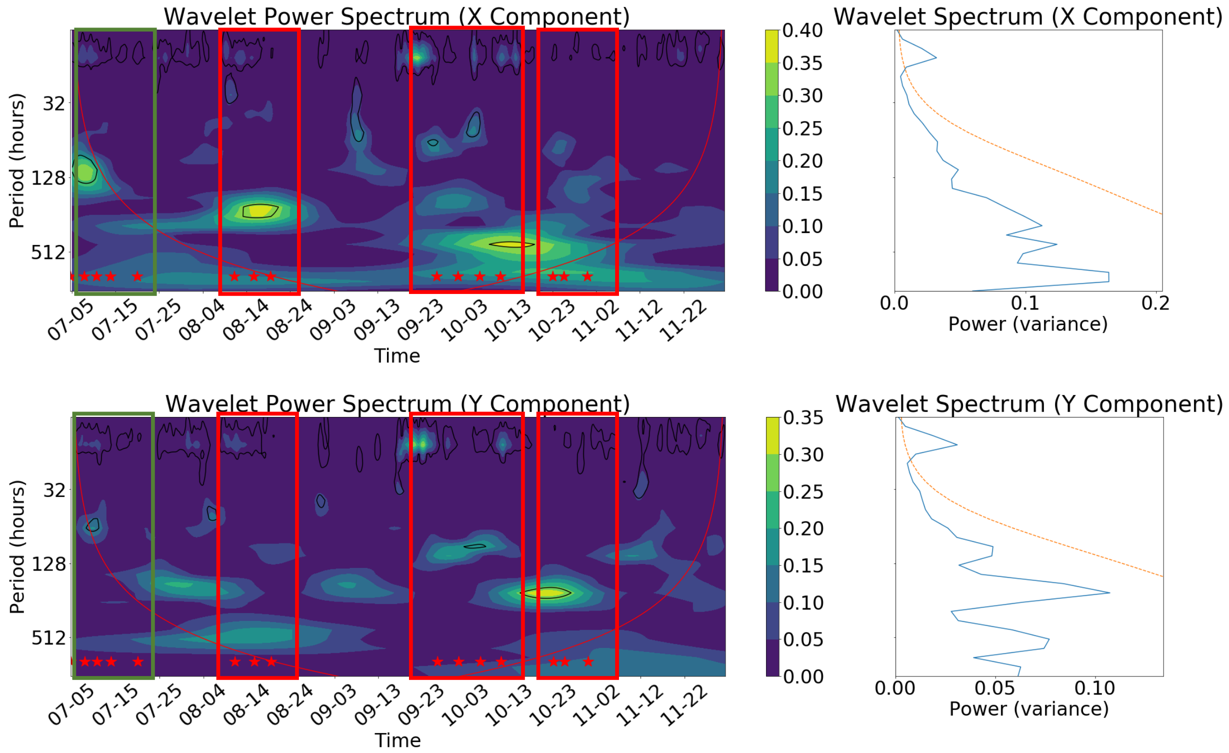

Figure 4.13: The Wavelet Power Spectrum (left) and the Wavelet Spectrum (right) of the filtered spectrum of buoy U1 for its four-month drift. The red line indicates the cone of influence, the black contours (left two figures) and orange dashed line (right two figures) indicate the 95% significance level. The red star symbols indicate the time when the storm cores were closest to the buoy location. The green rectangular box denotes the five storms previously examined in Chapter 3. The three red rectangular boxes denote the three sets of storms examined in Section 4.3.

5. SUMMARY AND CONCLUSION

An array of five buoys were deployed approximately 100 km south from the ice edge (Figure 3.2) in pancake ice conditions (60% pancake, ice 40% frazil ice) on 4th and 5th July 2017, during the Antarctic winter sea-ice expansion. This thesis builds on previous analyses published in Vichi et al. (2019) and Alberello et al. (2020). It expanded on those works by proposing that polar cyclones cause rapid variations of the sea-ice cover, and that sea ice and wind velocities are closely related, where ice drift is primarily governed by wind forcing. The aim of this thesis was to contribute to the understanding of the interactions between atmospheric forcing and sea-ice drift in the Antarctic MIZ, and to provide a better description of sea-ice dynamics in the MIZ by integrating existing data on the MIZ configuration with the atmospheric data and ice drift velocity.

5.1. Sea-ice response to atmospheric forcing from the cluster of buoys

The first part of the thesis focused on the entire cluster of buoys as firstly reported by Alberello et al. (2020). The cluster was analysed for 15 days over which five polar cyclones impacted the sea-ice cover. The first cyclone, classified as one of the rare explosive cyclones in the region (Vichi et al., 2019), first impacted the ice cover on the 2nd July, where it advected warm moist air on its eastern flank, generated large waves which penetrated deep into the MIZ, and also enhanced the southerly winds on its western flank. The four subsequent storms affected the MIZ region, and although less intense, they carried substantial energy and greatly impacted the buoys' ice drift.

The cluster of buoys in Chapter 3 remained within 100 km of the ice edge for ≈15 days (Figure 3.3) and with the intense waves-in-ice activity reported by Vichi et al. (2019) and Alberello et al. (2020), the results confirmed the initial inferences done in these papers that the sea ice never reached pack ice conditions but rather maintained the pancake-frazil ice conditions, and therefore remained within the MIZ. With this, free drift conditions were able to be assumed as the buoy array showed no signs of consolidation.

In this work, I computed several additional indicators of ice floe motion. All buoys within the cluster displayed sharp turns and loops (Figure 3.2(b)), leading to high meander coefficients during the passage of the cyclones. This is because the ice drift was significantly related to atmospheric forcing, as demonstrated by the high mean wind factors of ≈3%, the mean turning angles between ≈-22° to ≈-27°, falling within the typical range of 0° to -30° for the Southern Hemisphere (Leppäranta, 2011), and good correlations of 0.67 for the linear R^2 and 0.74 for the vector R_v^2 between wind and ice drift (see Table 3.2). From this is can be concluded that the sea-ice drift was primarily under the governance of wind forcing. Free-drift conditions allow the pancake floes to readily follow changes in atmospheric forcing, particularly during storm events, when wind speeds are high. The ice drift speed of all five buoys followed the wind speed for the 15 days with the largest ice drift speeds occurring during the cyclones and the smallest speeds occurring between the consecutive cyclones (Figure 3.5).

Spectral analysis revealed that the majority of the power within wind forcing is found at the lower (multi-day) frequencies, as seen in Figure 3.9, where the PSD of the wind velocity showed a continuous energy cascade from the lower frequencies to the higher frequencies. Furthermore, as the five cyclones discussed in Chapter 3 (Figure 3.1) passed over the MIZ, they transferred momentum from their energetic winds to the sea-ice cover. This was indicated by all of the five buoys in their PSDs, as they also showed an energy cascade from the lower frequencies to the higher (sub-daily) frequencies. However, as already highlighted by Alberello et al. (2020) and confirmed in this analysis, sea ice is additionally characterised by an energy peak at a frequency just below two cycles day^{-1} (≈13.5 hours) which lies with the inertial range of 13.47-13.59 hours, at 63°-62°S respectively, defined by the Earth's rotation. This is because sea ice, synchronous with the ocean, provides a medium that successfully allows the transfer of energy from the lower frequencies (wind forcing) to the sub-daily frequencies (Heil et al., 2009). Sea ice therefore responds to atmospheric forcing at the synoptic scale and the sub-daily frequencies.

The wavelet power spectrums of all five of the buoys (Figure 3.10 and Figures G-J in Appendix A) helped to visualise these two main energy components. Both the *u* and *v* drift components of the buoys' wavelet power spectrums displayed weak but statistically significant power within the inertial response period of ≈13.5 hours, except for buoy NYU1 due to its shorter drift period. However, majority of the power within sea-ice drift is found at the synoptic frequencies, denoting the direct transfer of momentum from the low-frequency wind forcing to the sea ice. These power intensifications however began to dissipate within a few days after the strong winds from the first two storms This dampening is due to kinetic energy dissipation within the Ekman layer, internal ice stresses and/or friction at the ice-ocean interface (Gimbert et al., 2012).

Buoy U3 showed a larger lower frequency energy component in its zonal velocity and minimal lower frequency energy in its meridional component, whereas the other buoys showed the opposite (Figure 3.10 and Figures G-J in Appendix A). This is due to buoy U3's more northerly location which led to it having an altered wind and ocean forcing, and a different drift path compared to the main cluster of buoys (Figure 3.2), and although similar, the rest of the buoys' wavelet power spectrums showed that they responded to the atmospheric forcing slightly differently. This is because the free drift conditions during these 15 days allowed the buoys to drift independently to one another, at scales between 5-100 km (Vichi et al., 2019).

5.2. Sea-ice response to atmospheric forcing during the advance-retreat phase

This thesis brings a novel analysis of the entire trajectory of buoy U1. While the other buoys stopped transmitting data in July and August presumably due to buoy malfunction, buoy U1 lasted until the 1st December, presumably due to sea-ice melting. It drifted a net distance of ≈1336 km from the South Atlantic sector to the Indian Ocean sector of the Southern Ocean. Throughout its four-month drift, buoy U1 continued to remain within ≈100 km of the ice edge (Figure 4.4), even during the winter sea-ice expansion when the ice edge advanced northwards. This would have allowed buoy U1 to be continuously susceptible to the storm-generated waves near the ice edge, where broken ice floes are more easily forced by winds. However, there was a two-day discrepancy between buoy U1 and both of the AMSR2 ice concentrations (Figures 4.2 and 4.3), whereas the SIC from the coarser SSMIS sensor with a spatial resolution of 25 km showed that buoy U1 was in the ice until the 1st December (Figure 4.3). Therefore, it was uncertain whether the estimate of the distance from the AMRS2 ice edge was accurate, as the AMSR2 passive microwaves sensors are known to have limited capabilities in detecting thin and small ice floes within the ice edge region. Therefore, the same calculation was computed using SSMIS ice concentrations. The comparison between the two satellite estimates showed vastly different and often opposite outcomes to each other (Figure 4.5), which can be attributed to the two different algorithms used by the products and/or their different spatial resolutions. Further analyses will therefore need to be conducted to assess the ice margin to determine the accuracy of these satellite products, especially during the summer months when the satellites' error becomes larger. However, Worby and Cosimo (2004) already reported a better correlation between the passive microwave-derived ice edge and in situ observations from ships, during the ice advance season compared to the observed melting season, and Beitsch et al. (2015) determined that the overall best agreement with the ship-based observations and a number of different passive microwave-derived ice concentrations was found for the Bootstrap algorithm.

Throughout this four-month drift, the sea-ice cover was continuously impacted by ice-landing cyclones as they travelled within the ACT. Ten of these cyclones with varying durations and intensities were visually found (Figures A-C in Appendix B), using the methods described in Section 2.4.4, to determine the interconnected processes occurring when polar cyclones pass over the ice edge. Vichi et al. (2019) suggested that cyclones (1) advect warm mid-latitude air onto the ice cover, (2) cause the southwards and northwards shifts of the ice edge, (3) carry substantial energy within their winds which intensifies ice drift, and 4) generates ocean waves near the ice edge, which can cause the break-up of ice floes up to ≈200 km into the ice cover. My analysis of buoy U1's drift confirmed the third point. Buoy U1's trajectory revealed large meandering and a dynamic response to wind forcing, as it displayed sharp turns and loops while drifting under the influence of varying winds (Figure 4.6). It was also found that during the periods of frequent cyclone activity, the ice drift velocity notably increased while also following the direction of the wind's velocity components. This strong relationship is further demonstrated by the sustained drift response measurements of buoy U1 (Table 4.2), where the ice drift speed was 2.73% of the wind speed, with a mean turning angle of -19.83 and good correlations of 0.60 for the linear R^2 and 0.76 for the vector R_v^2 between the wind and ice drift. This indicates that wind continued to have a dominant physical control on the ice floe trajectory throughout the four months, from winter to spring.

Buoy U1 did not measure waves in ice as it was presented in Vichi et al. (2019) for the first ≈15 days of the cluster. We can however speculate that waves are hardly affected by seasonality (Young et al., 2011) and therefore there was constant waves-in-ice activity throughout the four-month drift of buoy U1. Additionally, with the buoy's high wind response and the fact that it remained within approximately 100 km from the ice edge (Section 4.2), it can be concluded that there was no consolidation even during the maximum SIE, occurring in September (Eayrs et al., 2019). The pancake-frazil conditions of the initial ≈15-day analysis were likely to be maintained throughout the buoy's four-month drift, which further allows for the continued assumption of free-drift conditions for the entire drift of buoy U1 from the 5th July to 1st December 2017.

I used the spectral analysis (see Section 2.4.6) to further elucidate the strong influence of atmospheric forcing on ice drift. My results demonstrated that the PSD of the velocity components of both the wind and buoy U1 exhibited a continuous energy cascade (Figure 4.10), with majority of their power found between ≈128 and ≈512 hours (≈5 and >20 days). This range coincides with the frequency of the passage of cyclones in the SO (3-5 days) (Thorndike, 1986) and a seasonal atmospheric influence, which the four-month analysis was able to capture. It additionally shows the continued transfer of momentum from the lower-frequency wind forcing to the sea ice initially evidenced with the shorter analysis of Chapter 3. Seen by the prominent energy peak at 13.47 hours within the ice drift velocity, sea ice continued to be characterised by a strong inertial signature. As intense polar cyclones frequently passed over the ice cover, their strong winds are expected to have initiated inertial oscillations of the ice floes (Lammert et al., 2009; Heil et al., 2009), since sea ice is embedded within the surface of the ocean (Heil et al., 2009).

The wavelet power spectrum of buoy U1 (Figure 4.11) further highlighted the response of sea ice to wind forcing at both the lower (multi-day) and inertial frequencies. It showed three large power intensifications at the lower frequencies (≈128, ≈320 and ≈512 hours respectively) for the zonal velocity, with a lagged response in the meridional component. These intensifications appear to have coincided with the dates of the three groups of frequent cyclone activity (Figure A-C in Appendix B), suggesting the direct transfer of momentum from the erratic winds to the sea ice. The inertial signature was however not clearly visible in Figure 4.11 and therefore to further highlight the presence of inertial oscillations, I filtered out the multi-day frequencies (above 0.04 h^{-1}, >1 day). This allowed the power at the inertial range to become more significant, with majority of the power still remaining at the lower frequencies (see Figure 4.13). The relationship between the inertial oscillations and the frequency of storms is also suggested, but cannot be fully demonstrated because it appears that sometimes the power at the inertial frequency is coincident with the storms and sometimes it is not. Additionally, it is not clear how the specific periods of the synoptic events (from 5 to 20 days) affect the excitation, and what is their role on the zonal and meridional components of ice drift. A cluster of buoys with a longer drift period would be required to better understand the effects of the passage of storms on ice drift and the initiation of inertial oscillations of sea ice. Nevertheless, the strong influence at the lower (multi-day) frequencies has been identified as the primary effect of atmospheric forcing and the initiation of inertial oscillations of sea ice, for buoy U1's latitude range, has additionally been identified as the secondary effect of atmospheric forcing. This secondary effect strongly governs ice drift at shorter timescales and causes deviations of the ice drift from a straight-line path.

5.3. Implication for sea-ice characteristics in the MIZ

Pancake floes are extremely mobile if there is adequate wave energy preventing the pancakes from freezing together (Alberello et al., 2019). The seasonal evolution generally leads to a consolidated ice pack of molded pancakes as the freezing-front moves northwards, which leaves the region further from the effects of ocean waves (Doble and Wadhams, 2006). However, my analysis revealed that high mobility of ice floes was observed even during periods of high (>80%) sea-ice concentrations, as seen by the elliptical loops in Figure 4.6, and even when the SIC was at 100% (see Figure 4.6(c)). The sustained dynamic response of the ice floes to atmospheric forcing is due to the free-drift conditions which allowed the sea ice to be more susceptible to strong winds, during the passage of cyclones. The MIZ is known to be a highly dynamic region where the ocean and atmospheric interactions are stronger and more variable, and where pancake-frazil conditions are maintained. My analysis confirmed that buoy U1 did not leave the Antarctic MIZ throughout its four-month drift, with the AMSR2 sensor detecting ice concentrations above 80%, suggesting that instead of a local transition from smaller pancake ice floes into consolidated frozen pack ice, there is instead a northward push of a frontal band of unconsolidated sea ice. The exact extent of this frontal band and the features of the ice type left behind cannot be speculated from the available data and would require further observational studies.

As previously speculated by Vichi et al. (2019), the present concentration-based definition of the marginal ice zone being a narrow translational and temporary region bordering the open ocean is not suitable with the above analysis of the initial cluster of buoys as well as the four-month drift of buoy U1. The pancake-frazil ice conditions were maintained throughout the four months, even at 100% SIC, reported by the AMSR2 sensor at 3.125 km spatial resolution. Winter in situ observations indicated 60% pancake ice and 40% frazil ice (Vichi et al., 2019; Alberello et al., 2020). This implies that also the concentration-based MIZ definition, where the ice concentration lies between 15%-80% (detailed in Section 1.3), is inadequate to describe the sea-ice cover. This is because the highly dynamic nature of the MIZ is maintained at high ice concentrations, due to the ice cover being constantly impacted by the passage of polar cyclones. Therefore, this thesis highlights the need for a more holistic definition of the MIZ, which better incorporates the interconnected processes between the atmosphere, ocean and ice cover as these observations show how intense polar cyclones govern sea-ice drift in the MIZ, and hence the MIZ configuration. As already reported by Vichi et al. (2019), a better representation of the Antarctic MIZ in models is therefore needed, with the inclusion of the role that polar cyclones play in sea-ice variability and trends. This will allow for a better description of the MIZ and the Southern Ocean as a whole, and for better global climate predictions.

5.4. Future Work

The present study provided a comprehensive analysis of five ice buoys to better understand and highlight the effects of ice-crossing polar cyclones on sea-ice drift in the Antarctic however, this study did not include the analysis of the storm-generated waves, which are able to penetrate up to ≈200 km into the sea-ice cover. These waves contribute to the continuation of an unconsolidated ice cover, keeping the ice floes susceptible to strong winds brought by the polar cyclones. Therefore, future work will be aimed to investigate the relationship and correlation between wind-ice and wave-ice interactions of the pancake-frazil ice field, while also incorporating the dissipative underlying physical processes of sea-ice dynamics and wave attenuation. As previously reported in Section 5.2, inertial oscillations come from the combined ice-ocean system and therefore the role played by the geostrophic currents also needs to be measured in conjunction with the role of atmospheric forcing. Additionally, further analyses will be required to determine how the periods of the synoptic events (from 5 to 20 days) affect the excitation of inertial oscillations of sea ice, and what their specific role is on the zonal and meridional components of ice drift.

6. LIST OF REFERENCES

Ackley, S. F., Xie, H., & Tichenor, E. A., 2015. Ocean heat flux under Antarctic sea ice in the Bellingshausen and Amundsen Seas: two case studies. Annals of Glaciology, 56(69), pp. 200–210.

Alberello, A., Onorato, M., Bennetts, L., Vichi, M., Eayrs, C., MacHutchon, K. and Toffoli, A., 2019. Brief communication: Pancake ice floe size distribution during the winter expansion of the Antarctic marginal ice zone. *The Cryosphere*, *13*(1), pp. 41-48.

Alberello, A., Bennetts, L., Heil, P., Eayrs, C., Vichi, M., MacHutchon, K., Onorato, M. and Toffoli, A., 2020. Drift of pancake ice floes in the winter Antarctic marginal ice zone during polar cyclones. *Journal of Geophysical Research: Oceans*, 125(3), pp. e2019JC015418.

Allison, I. and Worby, A., 1994. Seasonal changes of sea-ice characteristics off East Antarctica. *Annals of Glaciology*, 20, pp.195-201.

Andreas, E.L. and Ackley, S.F., 1982. On the differences in ablation seasons of Arctic and Antarctic sea ice. *Journal of the Atmospheric Sciences*, 39(2), pp.440-447.

Andreas, E.L., Horst, T.W., Grachev, A.A., Persson, P.O.G., Fairall, C.W., Guest, P.S. and Jordan, R.E., 2010. Parametrizing turbulent exchange over summer sea ice and the marginal ice zone. *Quarterly Journal of the Royal Meteorological Society*, *136*(649), pp. 927-943.

Bartels-Rausch, T., Bergeron, V., Cartwright, J.H., Escribano, R., Finney, J.L., Grothe, H., Gutiérrez, P.J., Haapala, J., Kuhs, W.F., Pettersson, J.B. and Price, S.D., 2012. Ice structures, patterns, and processes: A view across the icefields. *Reviews of Modern Physics*, *84*(2), pp. 885.

Bauer, J. and Martin, S., 1983. A model of grease ice growth in small leads. *Journal of Geophysical Research: Oceans,* 88(C5), pp. 2917-2925.

Bojinski, S., Verstraete, M., Peterson, T.C., Richter, C., Simmons, A. and Zemp, M., 2014. The concept of essential climate variables in support of climate research, applications, and policy. *Bulletin of the American Meteorological Society,* 95(9), pp.1431-1443.

Beitsch, A., Kern, S. and Kaleschke, L., 2014. Comparison of SSM/I and AMSR-E sea ice concentrations with ASPeCt ship observations around Antarctica. *IEEE Transactions on Geoscience and Remote Sensing*, 53(4), pp.1985-1996.

Bracegirdle, T.J., Stephenson, D.B., Turner, J. and Phillips, T., 2015. The importance of sea ice area biases in 21st century multimodel projections of Antarctic temperature and precipitation. *Geophysical Research Letters*, *42*(24), pp.10-832.

Copernicus Climate Change Service., 2020. ERA5 hourly data on pressure levels from 1979 to present [Online]. [accessed on 1 May 2020]. Available from: https://cds.climate.copernicus.eu/.

Comiso, J.C. 2006. Abrupt decline in Arctic winter sea ice cover. *Geophysics Research Letters*, 33:1-5.

Doble, M.J. and Bidlot, J.R., 2013. Wave buoy measurements at the Antarctic sea ice edge compared with an enhanced ECMWF WAM: Progress towards global waves-in-ice modelling. *Ocean Modelling*, *70*, pp.166-173.

Doble, M.J., Coon, M.D. and Wadhams, P., 2003. Pancake ice formation in the Weddell Sea. *Journal of Geophysical Research: Oceans*, *108*(C7).

Doble, M.J. and Wadhams, P., 2006. Dynamical contrasts between pancake and pack ice, investigated with a drifting buoy array. *Journal of Geophysical Research: Oceans*, *111*(C11).

Dolatshah, A., Nelli, F., Bennetts, L.G., Alberello, A., Meylan, M.H., Monty, J.P. and Toffoli, A., 2018. Hydroelastic interactions between water waves and floating freshwater ice. *Physics of Fluids*, *30*(9), p.091702.

Eayrs, C., Holland, D., Francis, D., Wagner, T., Kumar, R. and Li, X., 2019. Understanding the Seasonal Cycle of Antarctic Sea Ice Extent in the Context of Longer-Term Variability. *Reviews of Geophysics*, 57(3), pp.1037-1064.

Feltham, D.L., 2005. Granular flow in the marginal ice zone. *Philosophical Transactions of the Royal Society A: Mathematical, Physical and Engineering Sciences*, 363(1832), pp.1677-1700.

Frölicher, T.L., Sarmiento, J.L., Paynter, D.J., Dunne, J.P., Krasting, J.P. and Winton, M., 2015. Dominance of the Southern Ocean in anthropogenic carbon and heat uptake in CMIP5 models. *Journal of Climate,* 28(2), pp.862-886.

Geiger, C.A., Hibler, W.D. and Ackley, S.F., 1998. Large-scale sea ice drift and deformation: Comparison between models and observations in the western Weddell Sea during 1992. *Journal of Geophysical Research: Oceans*, 103(C10), pp.21893-21913.

Gimbert, F., Jourdain, N.C., Marsan, D., Weiss, J. and Barnier, B., 2012. Recent mechanical weakening of the Arctic sea ice cover as revealed from larger inertial oscillations. *Journal of Geophysical Research: Oceans*, 117(C11).

Gimbert, F., Marsan, D., Weiss, J., Jourdain, N.C. and Barnier, B., 2012. Sea ice inertial oscillations in the Arctic Basin.

Grieger, J., Leckebusch, G.C., Raible, C.C., Rudeva, I. and Simmonds, I., 2018. Subantarctic cyclones identified by 14 tracking methods, and their role for moisture transports into the continent. *Tellus A: Dynamic Meteorology and Oceanography*, *70*(1), p.1454808.

Haas, C., 2017. *Sea Ice*. 3rd edn. Edited by David N. Thomas. Chichester: John Wiley and Sons Ltd.

Hague, M. and Vichi, M., 2018. A link between CMIP5 phytoplankton phenology and sea ice in the Atlantic Southern Ocean. *Geophysical Research Letters*, *45*(13), pp.6566-6575.

Heil, P., 1999. *Sea-ice growth, drift and deformation off Eastern Antarctica* (Doctoral dissertation, University of Tasmania).

Heil, P. and Allison, I., 1999. The pattern and variability of Antarctic sea- ice drift in the Indian Ocean and western Pacific sectors. *Journal of Geophysical Research: Oceans*, 104(C7), pp.15789-15802.

Heil, P. and Hibler III, W.D., 2002. Modeling the high-frequency component of Arctic sea ice drift and deformation. *Journal of Physical Oceanography*, 32(11), pp.3039-3057.

Heil, P., Massom, R.A., Allison, I., Worby, A.P. and Lytle, V.I., 2009. Role of off-shelf to on-shelf transitions for East Antarctic sea ice dynamics during spring 2003. *Journal of Geophysical Research: Oceans*, 114(C9).

Heorton, H.D., Feltham, D.L. and Hunt, J.C., 2014. The response of the sea ice edge to atmospheric and oceanic jet formation. *Journal of Physical Oceanography*, 44(9), pp.2292-2316.

Heorton, H.D., Tsamados, M., Cole, S.T., Ferreira, A.M., Berbellini, A., Fox, M. and Armitage, T.W., 2019. Retrieving Sea Ice Drag Coefficients and Turning Angles From In Situ and Satellite Observations Using an Inverse Modeling Framework. *Journal of Geophysical Research: Oceans*, 124(8), pp.6388-6413.

Hibler, W.D., Weeks, W.F., Kovacs, A. and Ackley, S.F., 1974. Differential sea-ice drift. I. Spatial and temporal variations in sea-ice deformation. *Journal of Glaciology*, *13*(69), pp.437-455.

Hobbs, W. R., Bindoff, N. L., and Raphael, M. N., 2014. New Perspectives on Observed and Simulated Antarctic Sea Ice Extent Trends Using Optimal Fingerprinting Techniques. *Journal of Climate*, 28(4), pp.1543–1560.

Hobbs, W. R., Massom, R., Stammerjohn, S., Reid, P., Williams, G., & Meier, W. 2016. A review of recent changes in Southern Ocean sea ice, their drivers and forcings. *Global and Planetary Change*, 143, pp.228–250.

Holland, P.R. and Kwok, R., 2012. Wind-driven trends in Antarctic sea-ice drift. *Nature Geoscience*, 5(12), pp.872-875.

Hopkins, M.A., Tuhkuri, J. and Lensu, M., 1999. Rafting and ridging of thin ice sheets. *Journal of Geophysical Research: Oceans*, 104(C6), pp.13605-13613.

Hoskins, B. J., and Hodges, K. I., 2005. A New Perspective on Southern Hemisphere Storm Tracks. *Journal of Climate*, 18(20), 4108–4129.

Howarth, D.A., 1983. An Analysis of the Variability of Cyclones Around Antarctica and Their Relationship to Sea- Ice Extent. *Annals of the Association of American Geographers*, 73(4), pp.519-537.

Hutchings, J.K., Heil, P., Steer, A. and Hibler, W.D., 2012. Subsynoptic scale spatial variability of sea ice deformation in the western Weddell Sea during early summer. *Journal of Geophysical Research: Oceans*, 117(C1).

iSTAR, 2014, Pancakes all around!. [Online]. [accessed on 24 April 2019]. Available from: https://www.istar.ac.uk/2014/03/05/pancakes-all-around/.

Iacozza, J., 2011. Spatial and temporal evolution of snow-covered sea ice, with reference to polar bear habitat.

Itkin, P., Spreen, G., Cheng, B., Doble, M., Girard-Ardhuin, F., Haapala, J., Hughes, N., Kaleschke, L., Nicolaus, M. and Wilkinson, J., 2017. Thin ice and storms: Sea ice deformation from buoy arrays deployed during N-ICE2015. *Journal of Geophysical Research: Oceans*, *122*(6), pp.4661-4674.

Irving, D., Simmonds, I. and Keay, K., 2010. Mesoscale cyclone activity over the ice-free Southern Ocean: 1999–2008. *Journal of climate*, 23(20), pp.5404-5420.

JAXA., 2015. About AMSR2. [Online]. [accessed on 1 May 2020]. Available from: https://suzaku.eorc.jaxa.jp/GCOM_W/w_amsr2/whats_amsr2.html

Kimura, N., 2004. Sea ice motion in response to surface wind and ocean current in the Southern Ocean. *Journal of the Meteorological Society of Japan. Ser. II*, *82*(4), pp.1223-1231.

Kimura, N. and Wakatsuchi, M., 2000. Relationship between sea- ice motion and geostrophic wind in the Northern Hemisphere. *Geophysical Research Letters*, 27(22), pp.3735-3738.

Kohout, A. L., Williams, M. J. M., Dean, S. M., & Meylan, M. H. (2014). Storm-induced sea ice breakup and the implications for ice extent. *Nature*, 509(7502), pp. 604–607.

Kottmeier, C. and Sellmann, L., 1996. Atmospheric and oceanic forcing of Weddell Sea ice motion. *Journal of Geophysical Research: Oceans*, 101(C9), pp.20809-20824.

Kwok, R., Pang, S.S. and Kacimi, S., 2017. Sea ice drift in the Southern Ocean: Regional patterns, variability, and trends. *Elem Sci Anth*, 5.

Lammert, A., Brümmer, B. and Kaleschke, L., 2009. Observation of cyclone- induced inertial sea- ice oscillation in Fram Strait. *Geophysical research letters*, 36(10).

Lecomte, O., Goosse, H., Fichefet, T., Holland, P. R., Uotila, P., Zunz, V., & Kimura, N. (2016). Impact of surface wind biases on the Antarctic sea ice concentration budget in climate models. *Ocean Modelling*, 105, 60–70.

Lemieux, J., Bouillon, S., Dupont F., Flato, G., Losch, M., Rampal, P., Tremblay, L., Vancoppenolle, M. and Williams, T., 2017. *Sea Ice Analysis and Forecasting*. 1st edn. Edited by Tom Carrieres, Mark Buehner, Jean-François Lemieux and Leif Toudal Pedersen. Cambridge University Press.

Leppäranta, M., 2011. *The drift of sea ice*. Springer Science & Business Media.

Leppäranta, M., Oikkonen, A., Shirasawa, K. and Fukamachi, Y., 2012. A treatise on frequency spectrum of drift ice velocity. *Cold regions science and technology*, 76, pp.83-91.

Lindsay, R.W., 2002. Ice deformation near SHEBA. *Journal of Geophysical Research: Oceans*, 107(C10), pp.SHE-18.

Liu, Y., Helfrich, S., Meier, W.N. and Dworak, R., 2020. Assessment of AMSR2 Ice Extent and Ice Edge in the Arctic Using IMS. *Remote Sensing*, 12(10), p.1582.

Lund, B., Graber, H.C., Persson, P.O.G., Smith, M., Doble, M., Thomson, J. and Wadhams, P., 2018. Arctic sea ice drift measured by shipboard marine radar. *Journal of Geophysical Research: Oceans*, 123(6), pp.4298-4321.

Maksym, T., 2019. Arctic and Antarctic Sea Ice Change: Contrasts, Commonalities, and Causes. *Annual Review of Marine Scien*ce, 11(1), null.

Martin, J.E., 2013. *Mid-latitude atmospheric dynamics: a first course*. John Wiley & Sons.

Massom, R.A., 1992. Observing the advection of sea ice in the Weddell Sea using buoy and satellite passive microwave data. *Journal of Geophysical Research: Oceans,* 97(C10), pp.15559-15572.

Massom, R.A. and Stammerjohn, S.E., 2010. Antarctic sea ice change and variability–physical and ecological implications. *Polar Science*, 4(2), pp.149-186.

Matear, R. J., O'Kane, T. J., Risbey, J. S., and Chamberlain, M., 2015. Sources of heterogeneous variability and trends in Antarctic sea ice. *Nature Communications*, 6, 8656.

McPhee, M.G. 1978. A simulation of inertial oscillation in drifting pack ice. *Dynamics of Atmospheres and Oceans*, 2(2), pp.107-122.

McPhee, M.G., 1988. Analysis and prediction of short-term ice drift.

McPhee, M.G., Morison, J.H. and Nilsen, F., 2008. Revisiting heat and salt exchange at the ice- ocean interface: Ocean flux and modeling considerations. *Journal of Geophysical Research: Oceans,* 113(C6).

Meier, W.N. and Stewart, J.S., 2019. Assessing uncertainties in sea ice extent climate indicators. *Environmental Research Letters,* 14(3), p.035005.

Messori, G., Woods, C., and Caballero, R., 2017. On the Drivers of Wintertime Temperature Extremes in the High Arctic. *Journal of Climate*, 31(4), 1597–1618.

Montiel, F., Squire, V.A., Doble, M., Thomson, J. and Wadhams, P., 2018. Attenuation and directional spreading of ocean waves during a storm event in the autumn Beaufort Sea marginal ice zone. *Journal of Geophysical Research: Oceans*, 123(8), pp.5912-5932.

Montiel, F. and Squire, V.A., 2017. Modelling wave-induced sea ice break-up in the marginal ice zone. *Proceedings of the Royal Society A: Mathematical, Physical and Engineering Sciences*, 473(2206), p.20170258.

Nansen, F., 1902. The oceanography of the North Polar Basin. The Norwegian North Polar Expedition 1893-1896. *Scient. Results*, 3(9).

National Center for Atmospheric Research Staff (Eds)., 2016. The Climate Data Guide: SSMI/, SSMIS: Special Sensor Microwave/Imager and Sounder. [Online]. [accessed on 11 August 2020]. Available from: https://climatedataguide.ucar.edu/climate-data/ssmi-ssmis-special-sensor-microwaveimager-and-sounder.

NSIDC, 2018. SMMR, SSM/I, and SSMIS Sensors. [Online]. [accessed on 11 August 2020]. Available from: https://nsidc.org/ancillary-pages/smmr-ssmi-ssmis-sensors.

Papritz, L., Pfahl, S., Rudeva, I., Simmonds, I., Sodemann, H. and Wernli, H., 2014. The role of extratropical cyclones and fronts for Southern Ocean freshwater fluxes. *Journal of Climate*, 27(16), pp.6205-6224.

Perovich, D.K., 2017. Sea Ice. 3rd edn. Edited by David N. Thomas. Chichester: John Wiley and Sons Ltd.

Petrich, C. and Eicken, H., 2017. *Sea Ice*. 3rd edn. Edited by David N. Thomas. Chichester: John Wiley and Sons Ltd.

Rao, V. B., do Carmo, A. M. C. and Franchito, S. H., 2002. Seasonal Variations in the Southern Hemisphere Storm Tracks and Associated Wave Propagation. *J. Atmos. Sci.*, 59, 1029–1040.

Schemm, S., 2018. Regional trends in weather systems help explain Antarctic sea ice trends. *Geophysical Research Letters*, *45*(14), pp.7165-7175.

Schlosser, E., Haumann, F.A. and Raphael, M.N., 2018. Atmospheric influences on the anomalous 2016 Antarctic sea ice decay. *Cryosphere*, 12(3), pp.1103-1119.

Schlosser, E., Powers, J.G., Duda, M.G. and Manning, K.W., 2011. Interaction between Antarctic sea ice and synoptic activity in the circumpolar trough: implications for ice-core interpretation. *Annals of Glaciology*, 52(57), pp.9-17.

Simmonds, I., 2003. Modes of atmospheric variability over the Southern Ocean. *Journal of Geophysical Research: Oceans,* 108(C4), SOV 5-1.

Skatulla, S., 2017. Photograph of ice buoy deployment

Stockwell, R.G., Large, W.G. and Milliff, R.F., 2004. Resonant inertial oscillations in moored buoy ocean surface winds. Tellus A: *Dynamic Meteorology and Oceanography*, 56(5), pp.536-547.

Strong, C., Foster, D., Cherkaev, E., Eisenman, I. and Golden, K.M., 2017. On the Definition of Marginal Ice Zone Width. *Journal of Atmospheric an Oceanic Technology*, 34, pp.1565-1584.

Thorndike, A.S., 1986. Kinematics of sea ice. In *The geophysics of sea ice* (pp. 489-549). Springer, Boston, MA.

Thorndike, A. S., and Colony, R. 1982. Sea ice motion in response to geostrophic winds. *Journal of Geophysical Research: Oceans*, 87(C8), 5845-5852.

Turner, J., Phillips, T., Marshall, G. J., Hosking, J. S., Pope, J. O., Bracegirdle, T. J., & Deb, P., 2017. Unprecedented springtime retreat of Antarctic sea ice in 2016. *Geophysical Research Letters*, 44(13), 6868–6875.

University of Hamburg, 2014. Sea ice Concentration. [Online]. [accessed on 20 May 2020]. Available from: https://www.ifm.uni-hamburg.de/en/workareas/remote/remotesensing/seaice/ice-concentration.html.

Uotila, J., 2001. Observed and modelled sea-ice drift response to wind forcing in the northern Baltic Sea. *Tellus*, 53A, pp. 112-128.

Uotila, J., Vihma, T. and Launiainen, J., 2000. Response of the Weddell Sea pack ice to wind forcing. Jo*urnal of Geophysical Research: Oceans*, 105(C1), pp.1135-1151.

Uotila, P., Vihma, T., Pezza, A.B., Simmonds, I., Keay, K. and Lynch, A.H., 2011. Relationships between Antarctic cyclones and surface conditions as derived from high-resolution numerical weather prediction data. *Journal of Geophysical Research: Atmospheres*, *116*(D7).

Vichi, M., Eayrs, C., Alberello, A., Bekker, A., Bennetts, L., Holland, D., de Jong, E., Joubert, W., MacHutchon, K., Messori, G. and Mojica, J.F., 2019. Effects of an explosive polar cyclone crossing the Antarctic marginal ice zone. *Geophysical Research Letters,* 46(11), pp.5948-5958.

Vihma, T. and Launiainen, J., 1993. Ice drift in the Weddell Sea in 1990–1991 as tracked by a satellite buoy. *Journal of Geophysical Research: Oceans*, 98(C8), pp.14471-14485.

Vihma, T., Launiainen, J., and Uotila, J., 1996. Weddell Sea ice drift: Kinematics and wind forcing. Journal of Geophysical Research: Oceans, 101(C8), 18279–18296.

Wang, Z., Turner, J., Sun, B., Li, B. and Liu, C., 2014. Cyclone-induced rapid creation of extreme Antarctic sea ice conditions. *Scientific reports*, *4*, p.5317.

Wassermann, S., Schmitt, C., Kottmeier, C. and Simmonds, I., 2006. Coincident vortices in Antarctic wind fields and sea ice motion. *Geophysical research letters*, *33*(15).

Weiss, J. and Dansereau, V., 2017. Linking scales in sea ice mechanics. *Philosophical Transactions of the Royal Society A: Mathematical, Physical and Engineering Sciences*, *375*(2086), p.20150352.

WMO. 2014. Guide to Meteorological Instruments and Methods of Observation (Report No. WMO-No.8) (p. 1128). Genva, Switzerland: World Meteorological Organization. Retrieved from http://hdl.handle.net/11329/365.

Woods, C., & Caballero, R., 2016. The Role of Moist Intrusions in Winter Arctic Warming and Sea Ice Decline. Journal of Climate, 29(12), 4473–4485.

Worby, A.P. and Comiso, J.C., 2004. Studies of the Antarctic sea ice edge and ice extent from satellite and ship observations. *Remote sensing of environment*, 92(1), pp.98-111.

Young, I.R., Zieger, S. and Babanin, A.V., 2011. Global trends in wind speed and wave height. *Science*, 332(6028), pp.451-455.

Yu, L., Jin, X., Schulz, E.W. and Josey, S.A., 2017. Air-sea interaction regimes in the sub-Antarctic Southern Ocean and Antarctic marginal ice zone revealed by icebreaker measurements. *Journal of Geophysical Research: Oceans*, *122*(8), pp.6547-6564.

Yuan, X., Patoux, J., and Li, C., 2009. Satellite-based midlatitude cyclone statistics over the Southern Ocean: 2. Tracks and surface fluxes. *Journal of Geophysical Research: Atmospheres,* 114(D4).

Zhang, J., Schweiger, A., Steele, M. and Stern, H., 2015. Sea ice floe size distribution in the marginal ice zone: Theory and numerical experiments. *Journal of Geophysical Research: Oceans*, 120(5), pp.3484-3498.

APPENDIX A

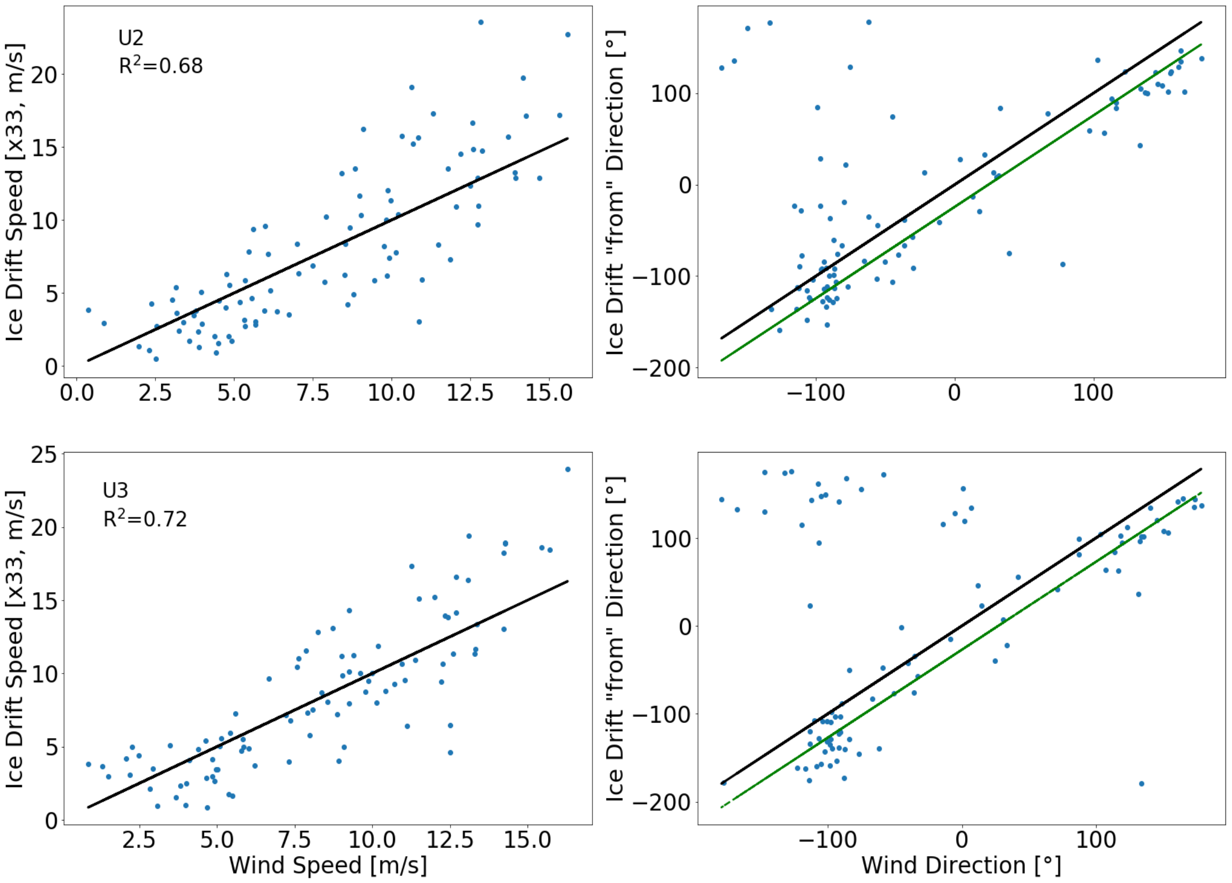

Figure A: Scatterplots (left) of ice drift speed as a function of wind speed and (right) of ice drift direction as a function of wind direction of the Trident Sensors Helix beacons. The black line is the 1:1 line. The green line is the turning angle at -24.32^{o} for U2 and -27.09^{o} for U3.

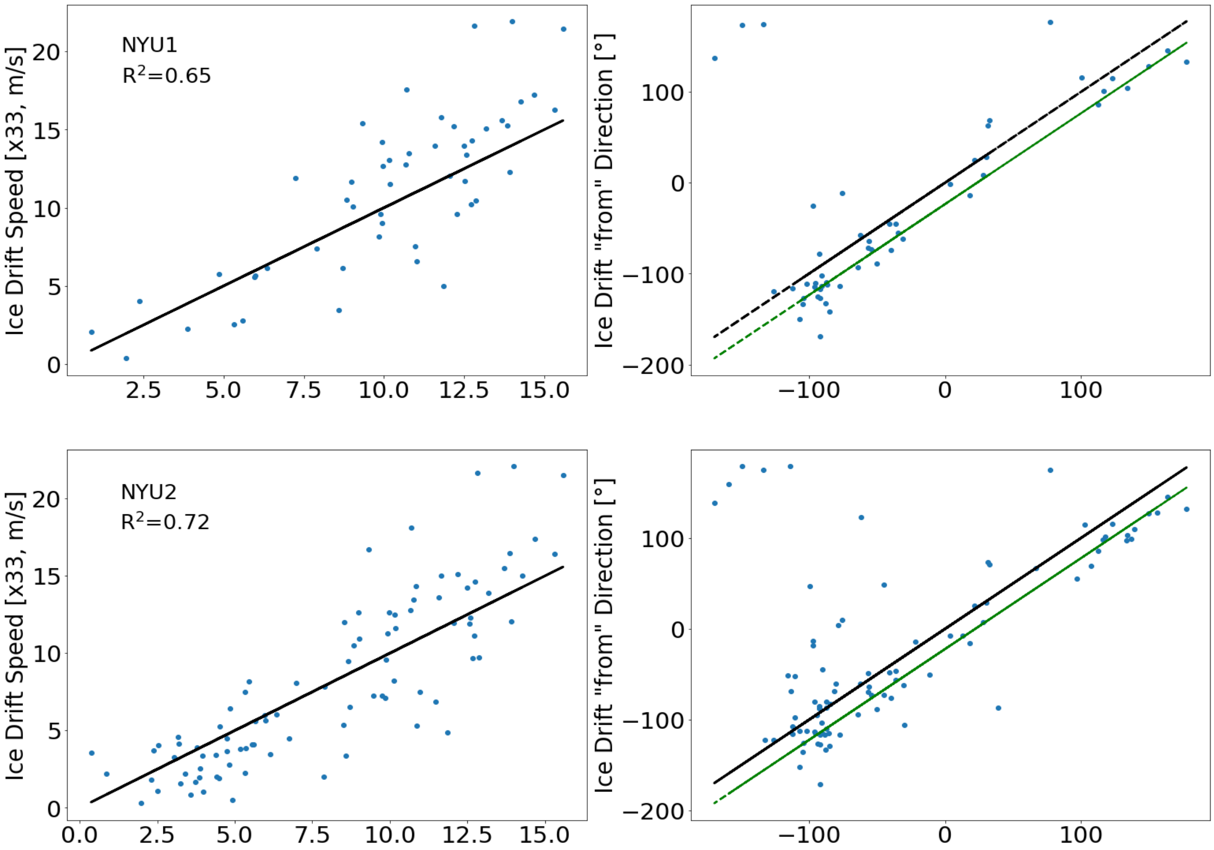

Figure B: **Scatterplots (left) of ice drift speed as a function of wind speed and (right) of ice drift direction as a function of wind direction of the WIIOS buoys. The black line is the 1:1 line. The green line is the turning angle at -23.54^o for NYU1 and -22.18^o for NYU2.**

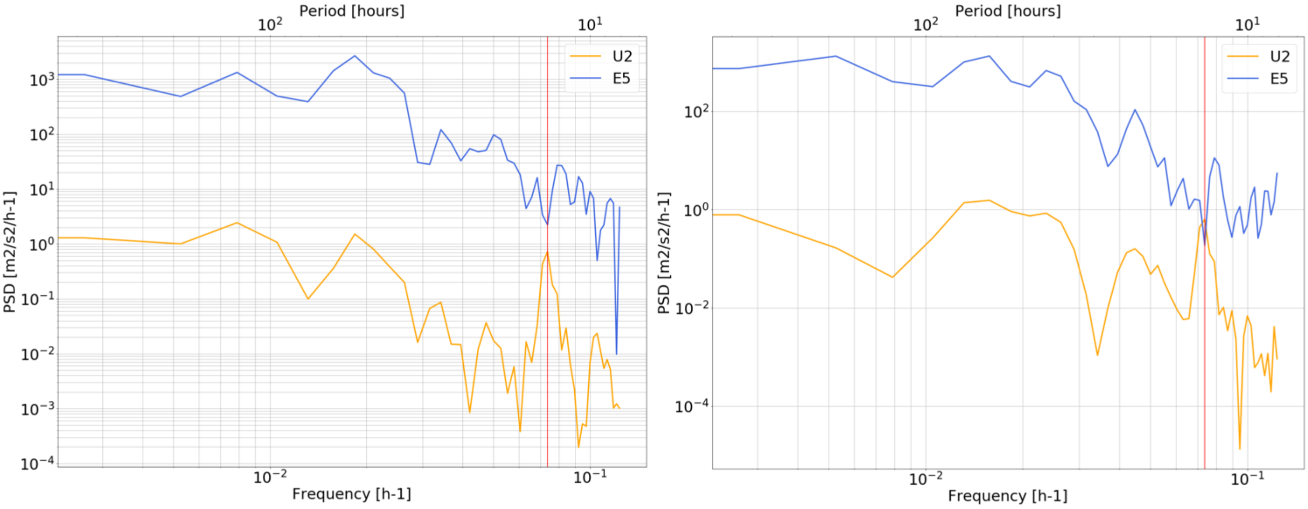

Figure C: Power Spectral Density corresponding to the (left) zonal component of ice drift velocity and the (right) meridional component of ice drift velocity for buoy U2. The orange line indicates buoy U2 and the blue line indicates the ERA5 winds. The vertical red line indicates the peak associated with an inertial oscillation (13.57 hours).

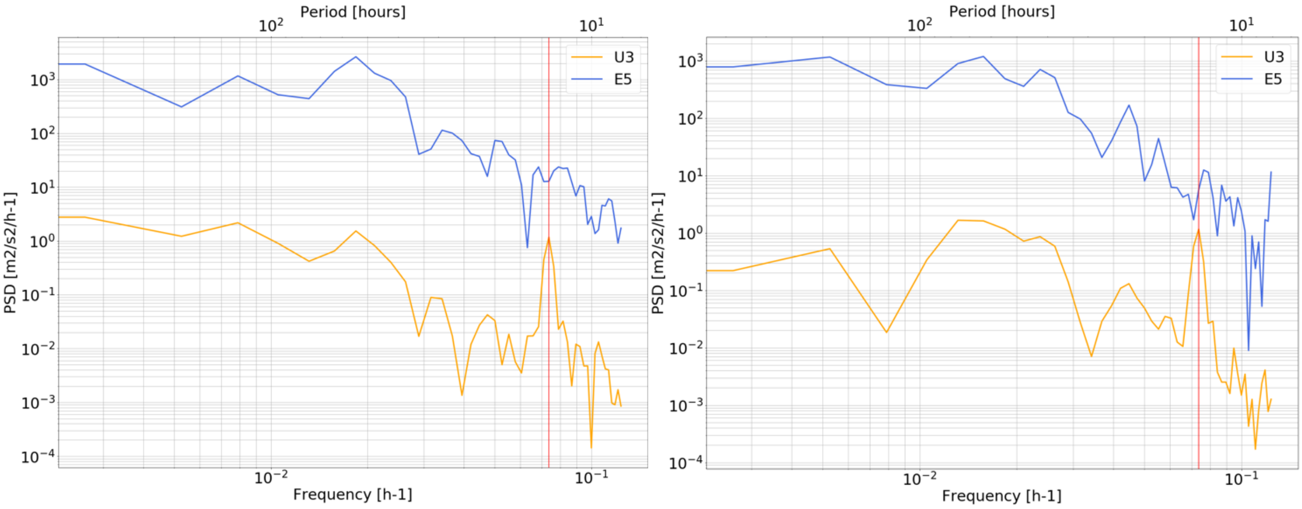

Figure D: Power Spectral Density corresponding to the (left) zonal component of ice drift velocity and the (right) meridional component of ice drift velocity for buoy U3. The orange line indicates buoy U3 and the blue line indicates the ERA5 winds. The vertical red line indicates the peak associated with an inertial oscillation (13.57 hours).

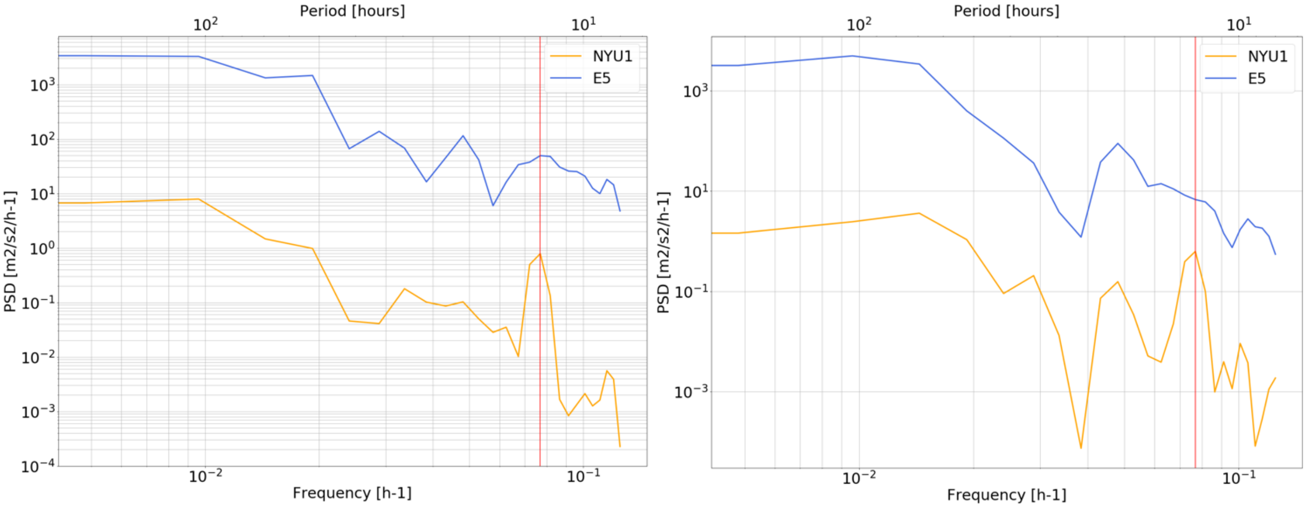

Figure E: Power Spectral Density corresponding to the (left) zonal component of ice drift velocity and the (right) meridional component of ice drift velocity for buoy NYU1. The orange line indicates buoy NYU1 and the blue line indicates the ERA5 winds. The vertical red line indicates the peak associated with an inertial oscillation (13.00 hours).

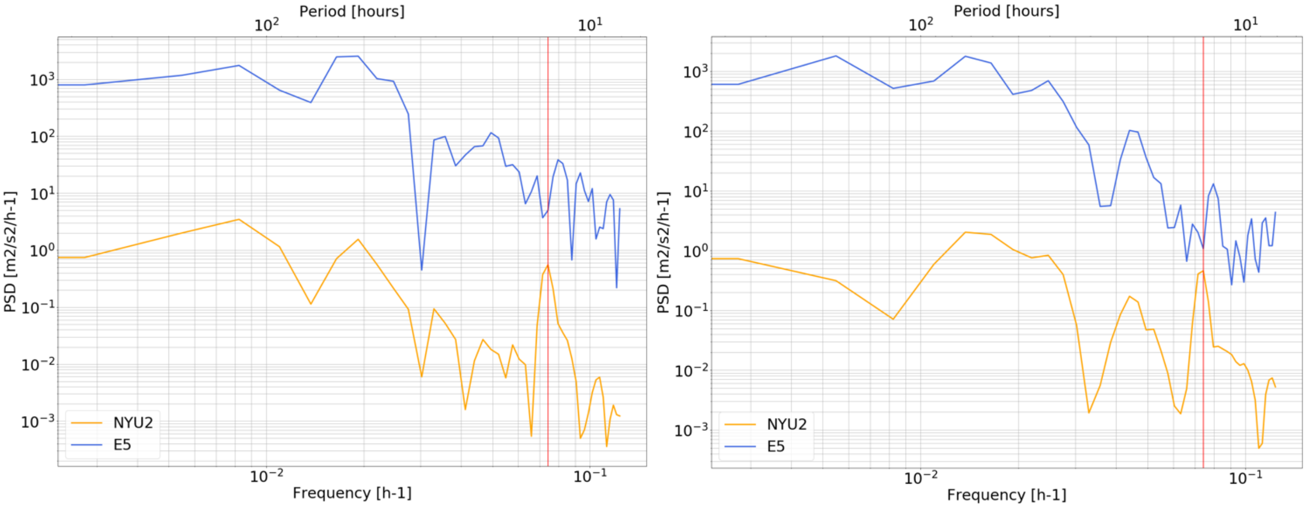

Figure F: Power Spectral Density corresponding to the (left) zonal component of ice drift velocity and the (right) meridional component of ice drift velocity for buoy NYU2. The orange line indicates buoy NYU2 and the blue line indicates the ERA5 winds. The vertical red line indicates the peak associated with an inertial oscillation (13.48 hours).

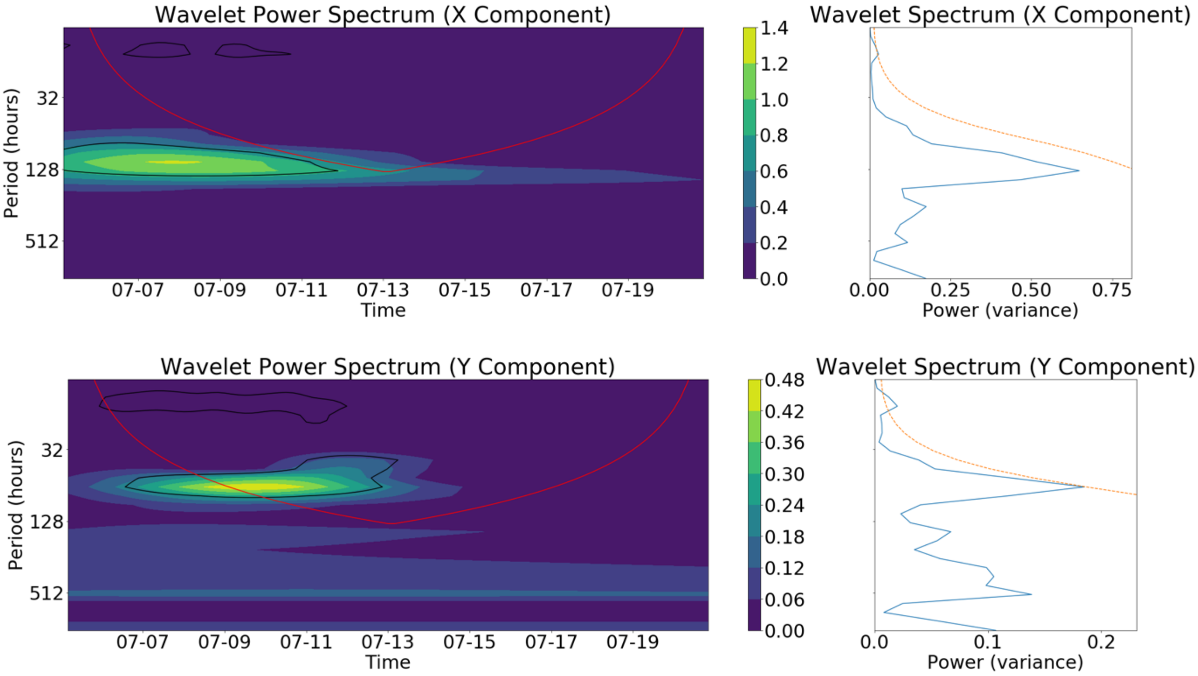

Figure G: The Wavelet Power Spectrum (left) and the Wavelet Spectrum (right) of buoy U2. The red line indicates the cone of influence, the black contours (left) and orange dashed line (right) indicate the 95% significance level.

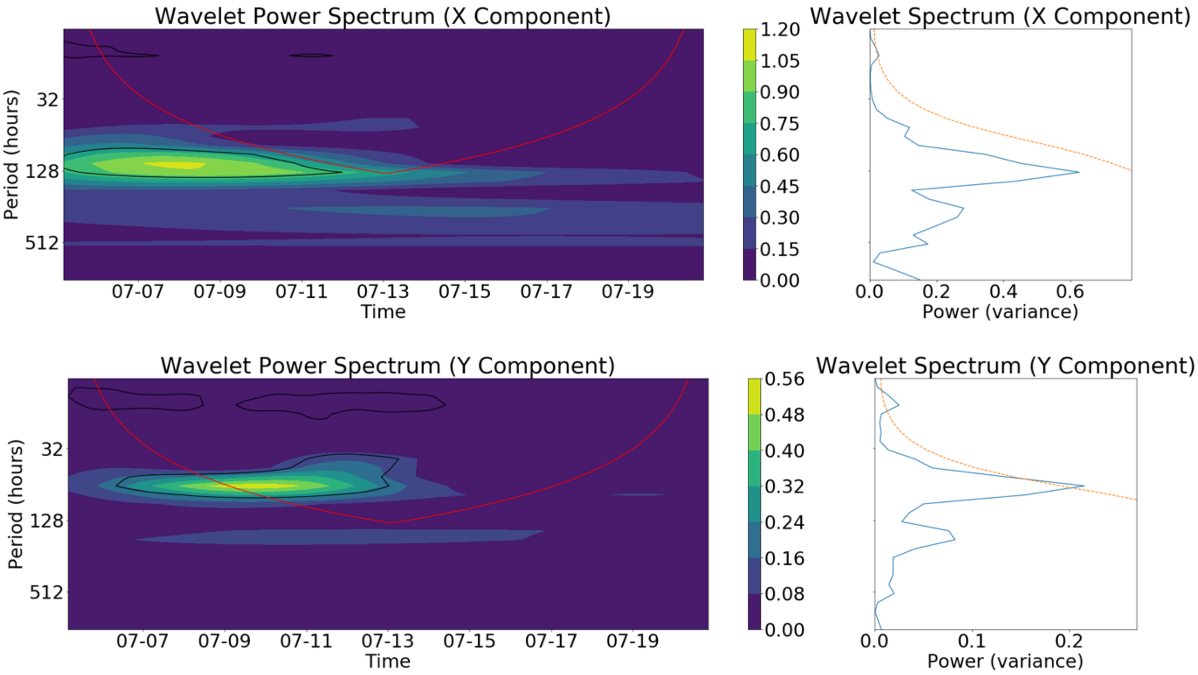

Figure H: The Wavelet Power Spectrum (left) and the Wavelet Spectrum (right) of buoy U3. The red line indicates the cone of influence, the black contour (left) and orange dashed line (right) indicate the 95% significance level.

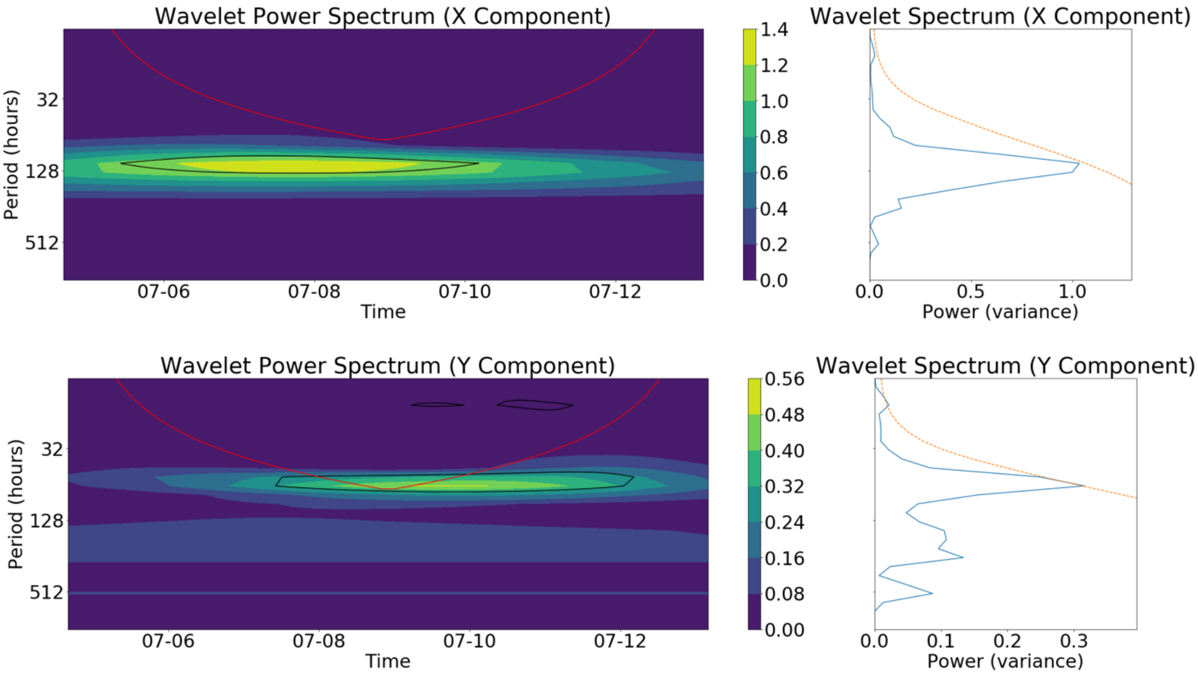

Figure I: The Wavelet Power Spectrum (left) and the Wavelet Spectrum (right) of buoy NYU1. The red line indicates the cone of influence, the black contours (left) and orange dashed line (right) indicate the 95% significance level.

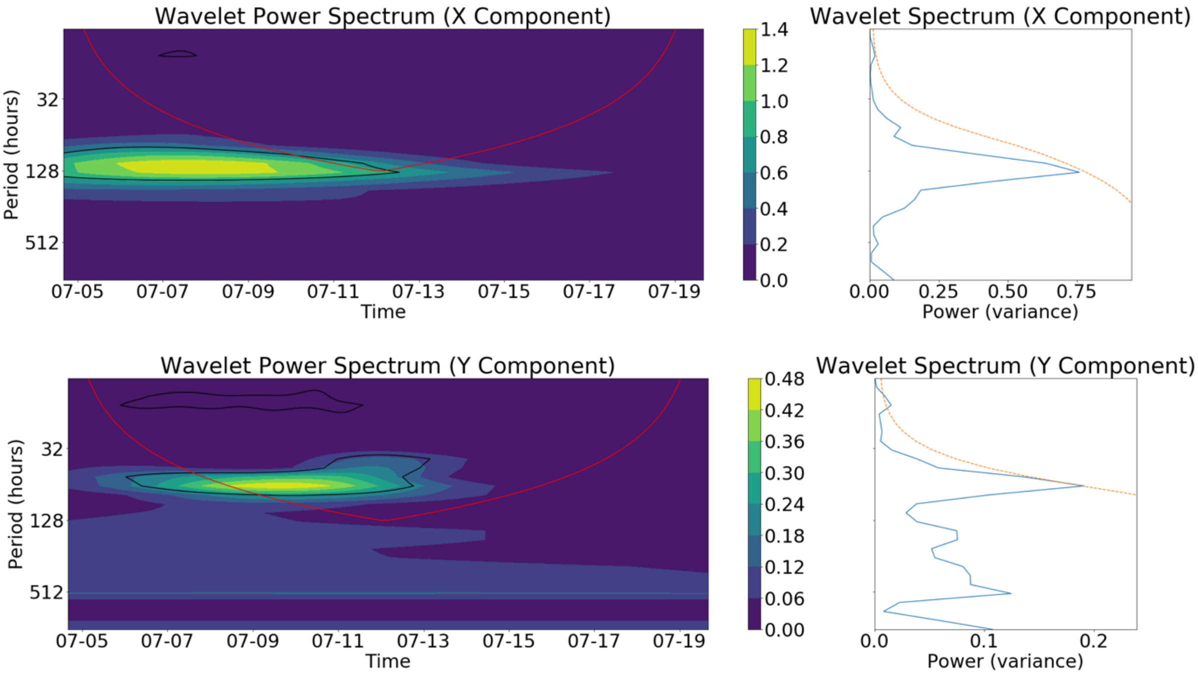

Figure J: The Wavelet Power Spectrum (left) and the Wavelet Spectrum (right) of buoy NYU2. The red line indicates the cone of influence, the black contours (left) and orange dashed line (right) indicate the 95% significance level.

APPENDIX B

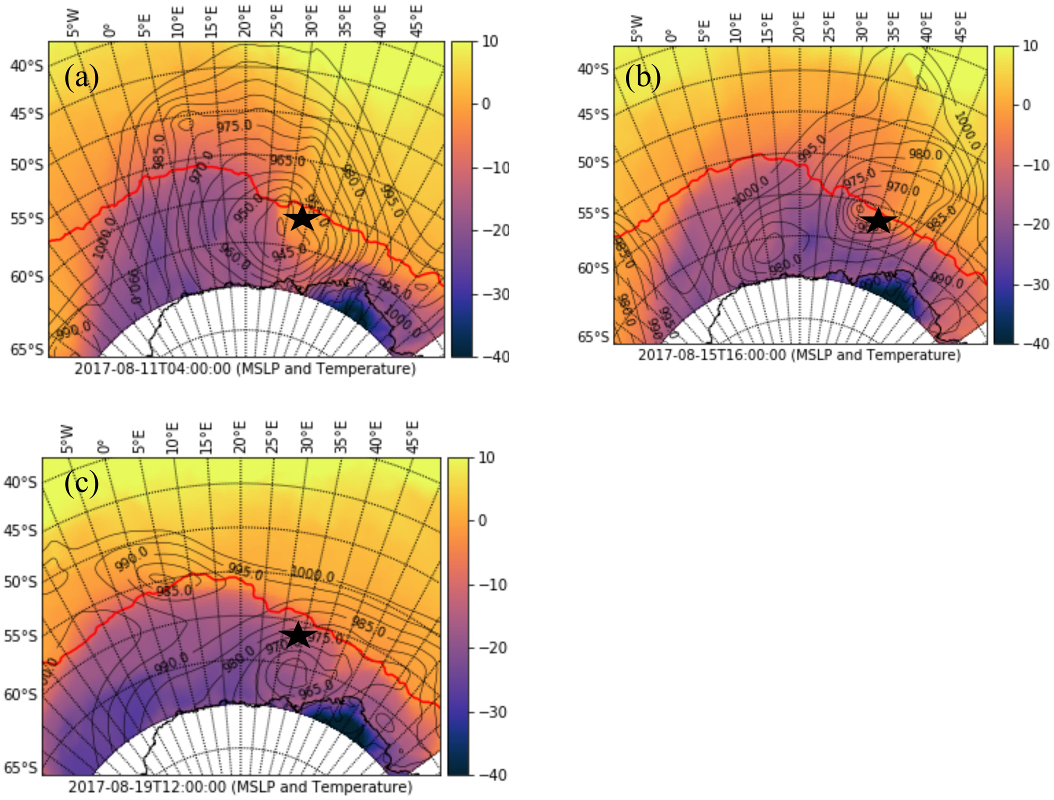

Figure A: Environmental conditions of the 3 storms when they were the close to the buoy U1 during the first large elliptical loop (see Figure 4.5): (a) at 04:00 on 11st of August; (b) at 16:00 on 15th of August; (c) at 12:00 on 19th of August. The black contour lies indicate the ERA5 isobars in hPa. The purple-orange shading indicates the ERA5 2-metre air temperature in ^{o}C. The black star denotes buoy U1's position for the corresponding day.

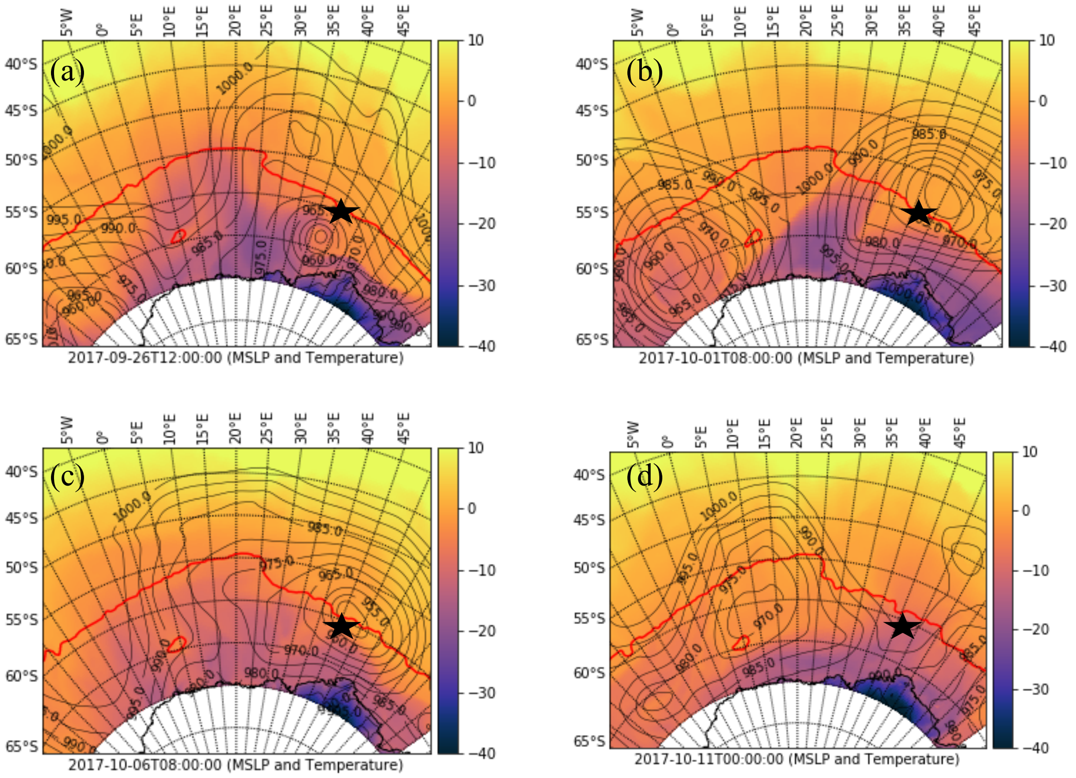

Figure B: Environmental conditions of the 4 storms when they were the close to the buoy U1 during the second large elliptical loop (see Figure 4.5): (a) at 12:00 on 26th of September; (b) at 08:00 on 1st of October; (c) at 08:00 on 6th of October; (d) at 00:00 on 11th of October. The black contour lies indicates the ERA5 isobars in hPa. The purple-orange shading indicates the ERA5 2-metre air temperature in °C. The black star denotes buoy U1's position for the corresponding day.

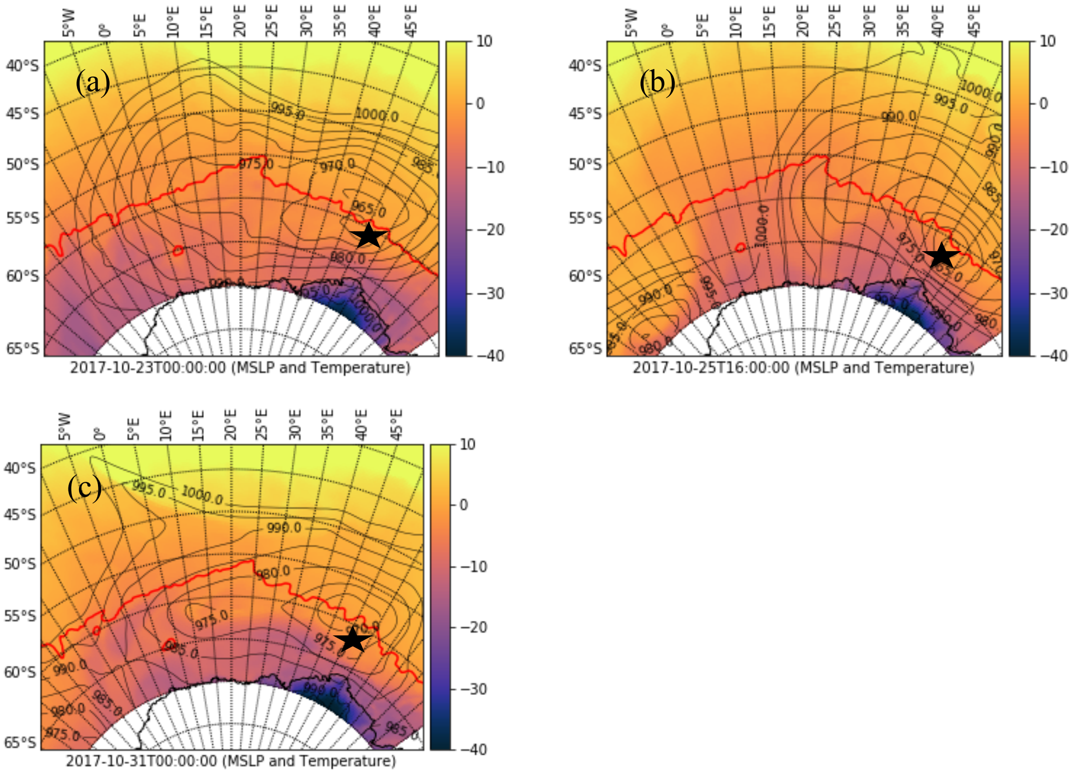

Figure C: Environmental conditions of the 3 storms when they were the close to the buoy U1 during the third large elliptical loop (see Figure 4.5): (a) at 00:00 on 23rd of October; (b) at 16:00 on 25th of October; (c) at 00:00 on 31st of October. The black contour lies indicate the ERA5 isobars in hPa. The purple-orange shading indicates the ERA5 2-metre air temperature in ^{o}C. The black star denotes buoy U1's position for the corresponding day.